University of Alberta

Geochemistry and source-tracing of the Sparrow Dyke Swarm, the Tsu Lake dykes, the Martin Group Igneous Rocks and the Christopher Island Formation

by

Rameses Joseph D'Souza

A thesis submitted to the Faculty of Graduate Studies and Research
in partial fulfillment of the requirements for the degree of

Master of Science

Department of Earth and Atmospheric Sciences

Spring 2012
Edmonton, Alberta

For Dad, Mum, Sarah and Jess.

Abstract

The present study has determined that tholeiitic basalt dykes, trending ∼130°, found near Tsu Lake, NT, are geochemically similar to the Sparrow Dyke Swarm (McGlynn *et al.*, 1974). Geochemically, the correlation of the calc-alkaline basalts of the Martin Group Igneous Rock (MGIR) with the Sparrow (Morelli *et al.*, 2009), is invalid as the former display higher incompatible element concentrations. Rather, the MGIR are geochemically similar to the ultrapotassic Christopher Island Formation (CIF).

Of these three suites, the Sparrow shows the least negative ϵNd, the CIF is the most negative and the MGIR is intermediate. Initial $^{87}Sr/^{86}Sr$ of these suites is similar within error. This is interpreted as evidence that the intensity of the metasomatism responsible for enriching the lithospheric mantle source of the CIF (Cousens *et al.*, 2001) began to wane towards the SW, where the MGIR were sourced, and was minimal where the Sparrow swarm was sourced.

Acknowledgements

This thesis would never have been possible without the help of many people. Drs. Ryan Morelli and Ken Ashton, at the Saskatchewan Geological Survey, kindly provided MGIR samples, data and information that I'd have had no other way of obtaining. Dr. Brian Cousens, at Carleton University, made public (and easily available) a large dataset of CIF analyses, for which I am very grateful. Drs. Tony Peterson and Sally Pehrsson, at the Geological Survey of Canada, provided me with a good deal of information that would otherwise have been difficult to find. Brian, Tony and Sally, in particular, identified my strange "red dykes" as "bostonites", leaving me less perplexed and very grateful. Last, but not least, Drs. Tom Chacko and Larry Heaman, whose efforts allowed me to start this project when I needed to, have provided so much help and guidance that is difficult to imagine doing a thesis with any other supervisors. Both have also given me role models upon which to base my own attitudes towards science and research. Tom and Larry have suffered through many drafts of this thesis and have ironed out the wrinkles in logic and correctness; any remaining errors are solely my own.

The hard work involved in this project was made much more bearable by my dear friends, Josh Davies, Steve Mamet, Noland Germain and Kim Precht. I'll be forever indebted to them (and others) for being my friends (and remaining so) and sharing a love of not talking about normal things. The unquestioning love and support from my family has provided the metaphorical rock from which I have been able to go off and study real rocks. It is to them that I dedicate this work.

Contents

List of Tables

List of Figures

List of Symbols

Acronyms

AFM	Alkali-FeO*-MgO
CHUR	Chondritic Uniform Reservoir
CIF	Christopher Island Formation
DM	Depleted Mantle
EM I	Enriched Mantle I
EM II	Enriched Mantle II
E-MORB	Enriched Mid-ocean Ridge Basalt
HFSE	High Field Strength Elements
HREE	Heavy Rare Earth Elements
ICP-MS	Inductively Coupled Plasma-Mass Spectrometry
LILE	Large Ion Lithophile Elements
LIP	Large Igneous Province
LREE	Light Rare Earth Elements
LOI	Loss On Ignition
MGIR	Martin Group Igneous Rocks
MIE	Molson Igneous Events
MORB	Mid-ocean Ridge Basalt

MREE	Middle Rare Earth Elements
OIB	Ocean Island Basalt
REE	Rare Earth Elements
RIF	Radiogenic Isotope Facility
SCLM	Sub-continental Lithospheric Mantle
STZ	Snowbird Tectonic Zone
TAS	Total Alkali vs. Silica
THO	Trans-Hudson Orogeny
TMZ	Taltson Magmatic Zone
TTZ	Thelon Tectonic Zone
XRF	X-Ray Fluorescence

Abbreviations

ca.	circa
HIMU	high μ
km^2	squared kilometres
meas.	measured
$(La/Sm)_N$	E-MORB normalized La/Sm ratio
NT	Northwest Territories
NU	Nunavut
SK	Saskatchewan
$(Sm/Yb)_N$	E-MORB normalized Sm/Yb ratio
WC mill	Tungsten carbide mill
wt.%	weight percent

Symbols

λ	Decay constant

σ	Standard Deviation
σ_1	Principal Compressional Stress axis
σ_3	Principal Extensional Stress axis

Chapter 1

Introduction

Large Igneous Provinces (LIPs; Coffin and Eldholm, 1991, 1993) are a geological phenomenon wherein extremely large quantities of generally basaltic magma are erupted relatively quickly (i.e., generally on the order of a million cubic kilometres erupted in under two million years). The bulk of the erupted material from Phanerozoic LIPs is preserved (e.g., Columbia River Basalts, the Deccan Traps and the Ontong-Java Plateau), however this component has generally been eroded away for older LIPs. In such cases, the only evidence for the LIPs are the mafic dykes that fed them.

Mafic dykes are used as multi-purpose pins in paleocontinental reconstructions to constrain the position of a crustal block at a particular time in Earth history (e.g., Harlan *et al.*, 2003). This stems from their generally short-lived nature, accurately measurable by U-Pb dating of zircon and/or baddeleyite, and improvements in the techniques and instrumentation for detecting and measuring paleomagnetism in mafic rocks. In combination with similar data from other crustal blocks, paleocontinental reconstructions may be rigorously assessed.

In a geochemical sense, mafic dykes can also provide information regarding

the state and nature of the mantle beneath a crustal block at the time of emplacement. LIPs with an Ocean Island Basalt (OIB) signature may indicate that a mantle plume impinged on the base of the lithosphere, melting it and emplacing dykes that fed the resulting LIPs (e.g., Morgan, 1971; Campbell, 2005). This scenario is well-supported in some instances, such as the 1.27 Ga Mackenzie Dyke Swarm (LeCheminant and Heaman, 1989), which shows a radiating pattern, uplift in the area of plume impingement at the dykes' focus, on Victoria Island, Northwest Territories (NT), and vertical flow in the dykes near the focus, but lateral flow away from the focus (Baragar *et al.*, 1996).

Other dyke swarms are not so convincingly attributable to mantle plumes. In addition to non-OIB-like geochemistry, dykes such as those of the Molson Igneous Event (*ca.* 1.88 Ga; Heaman *et al.*, 2009, and references therein) are not radially distributed around a focus and uplift of the region at the time of emplacement is difficult to demonstrate. For such dykes, geochemistry indicates that the source was similar to depleted mid-ocean ridge basalt (MORB) mantle (e.g., Heaman *et al.*, 2009) and may be attributed to passive or hybrid asthenosphere upwelling (Foucher *et al.*, 1982; White and McKenzie, 1989), lithospheric delamination (Elkins-Tanton and Hager, 2000), meteorite impact-induced melting (Rampino, 1987), or edge-driven convection (King and Anderson, 1998).

The Churchill Province, exposed in northeast to central Canada, is the site of emplacement of many dyke swarms from Neoarchean to Neoproterozoic time (Buchan and Ernst, 2004, and references therein). This includes the aforementioned Mackenzie dyke swarm and the ∼130°-trending, 1830 Ma Sparrow Dyke Swarm (McGlynn *et al.*, 1974; Bostock and van Breemen, 1992).

The latter is especially interesting as the only other expression of *ca.* 1830 Ma mafic magmatism is the Christopher Island Formation (CIF; Peterson *et al.*, 1994, and references therein). The CIF is an ultrapotassic province, consisting of lamprophyre and minette dykes and flows, extending from Rankin Inlet, Nunavut (NU), potentially as far south as Lake Athabasca, Saskatchewan (SK; Cousens *et al.*, 2004; Ashton *et al.*, 2009). This extremely large areal extent, over 200,000 km^2 (Peterson *et al.*, 2010), is highly unusual for ultrapotassic rocks which are generally thought to be produced by small-degree partial melting of locally enriched mantle (Cousens *et al.*, 2004, and references therein). Whereas there are conflicting models regarding the nature of the CIF source (see next chapter), it is universally acknowledged that they represent an enriched mantle.

Mafic dykes were emplaced at *ca.* 1820 Ma near present-day Lake Athabasca, SK, as part of the Martin Group (Morelli *et al.*, 2009). The Martin Group itself is thought to be correlative to the Baker Lake Group, of which the CIF is also a part (Ashton *et al.*, 2009, and references therein). Morelli *et al.* (2009) postulate that the igneous rocks of the Martin Group are likely correlative to the Sparrow dykes, on the basis of similar timing of emplacement, orientation (i.e., $\sim$130°) and petrography. As there is no published geochemistry of the Sparrow dykes, these criteria were also used by Ewanchuk (2006) to postulate the correlation of the Sparrow Dyke Swarm with the *ca.* 1830 Ma (Heaman, pers. comm.) mafic dykes found at Tsu Lake, Northwest Territories (NT).

The major tectonic event affecting the Churchill Province during the Paleoproterozoic was the Trans-Hudson Orogeny (THO; Hoffman, 1988), lasting from *ca.* 1.92 Ga to 1.8 Ga (Ansdell, 2005, and references therein). The

metamorphic effect of this major and long-lived tectonic event (culminating with the docking of the western Superior craton to the southeastern Churchill Province), is widespread across the Churchill Province but very restricted in the Superior (Corrigan *et al.*, 2009). This implies that the crustal block containing the Churchill Province, and terranes accreted over the duration of the THO, was under considerable tectonic stress during the time of emplacement of the CIF, Sparrow dykes, igneous rocks of the Martin Group, and the dykes at Tsu Lake.

The purpose of the present study is to first establish the validity of the correlations of the Sparrow Dyke Swarm with the Tsu Lake dykes (Ewanchuk, 2006) and Martin Group Igneous Rocks (Morelli *et al.*, 2009) on a geochemical basis. This geochemical information will then be used to make inferences about the source (or sources) of these mafic rocks. Combined with the published data for the CIF (Cousens *et al.*, 2001), these data can provide a view to the nature of the mantle underlying a large part of the western Churchill Province. A final objective of this study is to reconcile the simultaneous emplacement of these mafic magmas during the terminal phases of the THO.

Chapter 2

Regional geology and previous work

The focus of the present study is the geochemistry of the mafic dykes of the Sparrow Dyke Swarm, the dykes at Tsu Lake, NT, and the dykes, sills and volcanics of the Martin Group, found near Uranium City, SK. This *ca.* 1830 Ma mafic magmatism will also be compared with the contemporaneous (Rainbird *et al.*, 2006) ultrapotassic Christopher Island Formation (CIF) magmatism, found farther east in the Churchill Province (Paul *et al.*, 2002). To properly place the present research in the context of preceding work, this section will summarize the previous work on the geology of these igneous rocks and the country rocks into which they are emplaced. The general locations of the geological entities mentioned in this section are illustrated in Figure 2.1.

2.1 Regional geology

The igneous rocks of the present study are emplaced within the Churchill Province, located in north-central Canada. The Churchill Province consists of two domains: the Rae domain in the northwest and the Hearne domain in the southeast, separated by the Snowbird Tectonic Zone (STZ). The base-

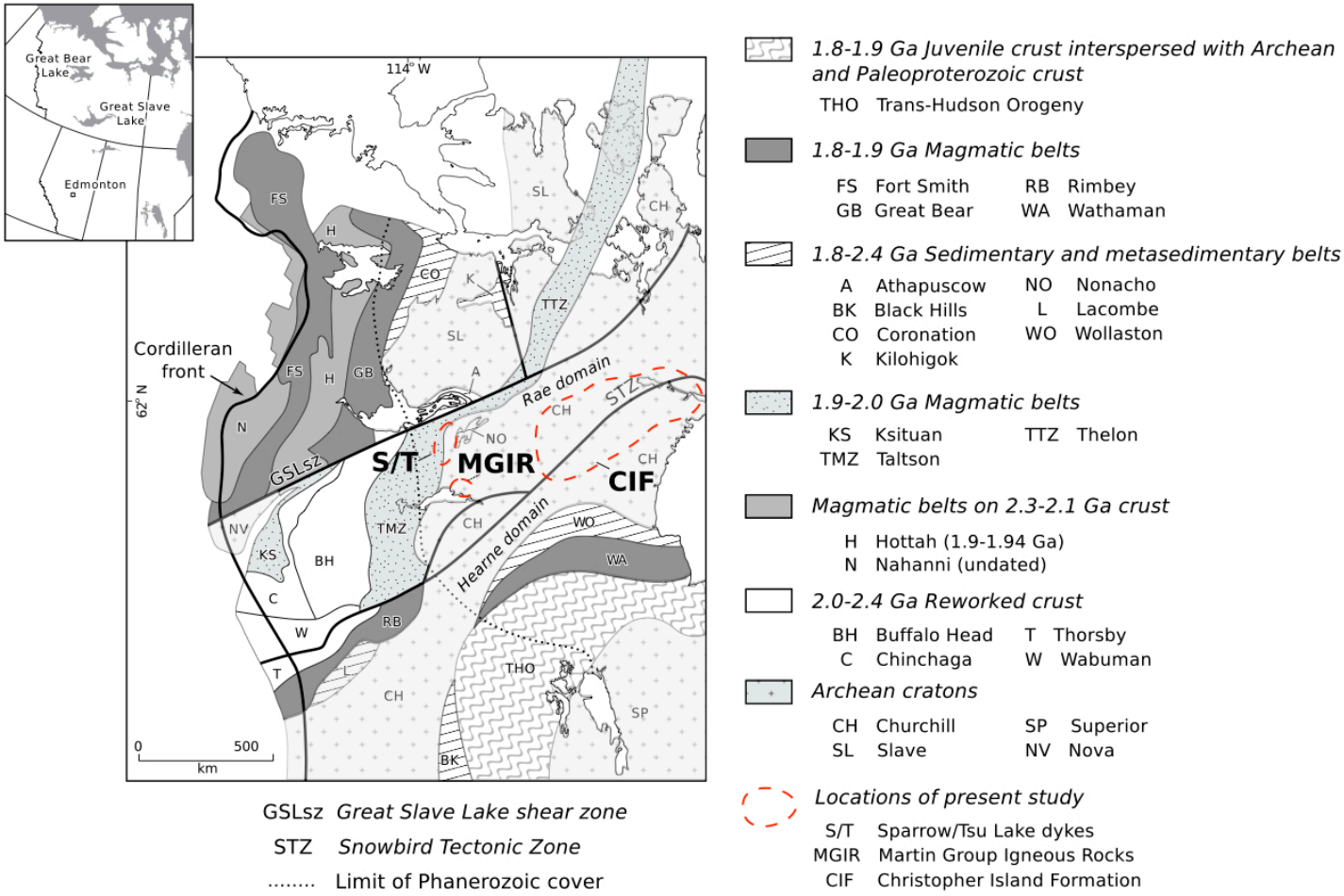

Figure 2.1: Simplified geological map of the Precambrian provinces and domains in Canada, after Chacko *et al.* (2000).

ment rocks of the Rae domain comprises granites as old as 3.33 Ga, whereas gneisses in the Hearne domain are up to 3.48 Ga (Wanless, 1979). As per the compilation map in Hoffman (1988), both the Rae and Hearne domains contain Neoarchean greenstone belts and remnants of Proterozoic sedimentary platformal cover.

The nature of the STZ is cryptic; geophysical evidence (e.g., Sharpton *et al.*, 1987) indicates gravity anomalies that are compatible with it being a suture between the Rae and Hearne domains, as summarized in Hoffman (1988). However, the lithologic evidence for this is not straightforward: folding and metamorphic grade in the basement of the Hearne are seen to increase toward the STZ, although this is not seen in the Rae (Hoffman, 1988). Furthermore, the similarities between these domains and the lack of convergence-related magmatic arcs make the hypothesis of the STZ as a suture contentious and, as indicated by Cousens *et al.* (2001), the similarities on both sides of the STZ of the Sub-continental Lithospheric Mantle (SCLM), which the CIF is thought to sample, further erodes the idea of the STZ being a suture between two separate crustal blocks.

The western margin of the Churchill craton is a belt of granitoid rocks: the Taltson Magmatic Zone (TMZ) and the Thelon Tectonic Zone (TTZ), to the south and north of the Great Slave Lake shear zone, respectively. The TMZ, into which the Sparrow and Tsu Lake dykes are emplaced, consists of several granitoid suites with differing accessory mineral assemblages and ranges in age from 1.99 to 1.93 Ga (Chacko *et al.*, 2000, and references therein). Hoffman (1988) and Thériault (1992) argue that the TMZ marks the site of the 2.0 to 1.9 Ga closure of an ocean basin separating the Churchill Province from

terranes to the west. In contrast, on the basis of major-element geochemical and Nd, Pb and O-isotopic evidence, Chacko *et al.* (2000) and De *et al.* (2000) argue that the TMZ granitoids must have been produced in the hinterland of a collision to the west of the Slave Province at *ca.* 2.0 Ga.

The southwestern Rae domain comprises rocks as old as 3.0 Ga, although detrital zircons and xenocrysts in granites have been found as old as 3.9 Ga (Hartlaub *et al.*, 2005). The Beaverlodge subdomain, near Lake Athabasca, Saskatchewan (SK), consists of granitoid basement rocks that are of 2.3, 2.6 and 3.0 Ga, variably metamorphosed from amphibolite to granulite grade (Ashton *et al.*, 2009, and references therein). In the western-most portion of the Beaverlodge subdomain, leucogranites have been found with ages of 1.97 and 1.93 Ga (Hartlaub *et al.*, 2005), making it likely that they are the eastern-most representatives of the TMZ granitoids. It is this Archean to early Paleoproterozoic basement that the Martin Group overlies (Morelli *et al.*, 2009).

2.2 *Ca.* 1830 Ma mafic rocks of the Churchill craton

2.2.1 The Sparrow Dyke Swarm

As part of a larger study on mid-Proterozoic paleomagnetism, McGlynn *et al.* (1974) carried out a paleomagnetic study of dykes trending ∼130°, in the Nonacho Group. Those authors named the dykes the 'Sparrow Dyke Swarm', after Sparrow Bay on Nonacho Lake, NT. The Nonacho group that these dykes intrude consists dominantly of sandstones, conglomerates and and shales overlying a granitic basement (Henderson, 1939b). For completeness, although

not relevant to the present study, McGlynn *et al.* (1974) found a paleopole for the Sparrow dykes at 12°N, 69°W.

The only other study on the Sparrow dykes, by (Bostock and van Breemen, 1992), reported an age for the dyke at Jerome Lake, NT (i.e., 1827 ± 4 Ma; U-Pb on baddeleyite). At the time of this writing, no geochemical data have been published for the dykes sampled in either of these studies.

2.2.2 The Tsu Lake dykes

Although the dykes at Tsu Lake, NT, were mapped by Wilson as early as 1941, their chemical composition was not investigated until the study of Ewanchuk (2006). Field-work for that study indicated that the majority of dykes in the area trend ∼130° and comprise two compositionally distinct basaltic magma types (i.e., enriched vs. depleted incompatible element concentrations). Ewanchuk (2006) interpreted these compositional differences to indicate derivation from two different mantle sources. On the basis of a Th/Ta vs. La/Yb plot (Condie, 1997), Ewanchuk (2006) postulated that the enriched dykes were from a HIMU-type source, whereas the non-enriched are from an OIB-like source.

The 'Taltson River Dyke' (location 130; Ewanchuk, 2006) shows complex cross-cutting relationship with the surrounding granites and granitic gneisses. For this granitic material, Ewanchuk (2006) reported U-Pb zircon ages of *ca.* 1950 Ma. Despite large error in these ages, this is in line with maps indicating that the granites around Tsu Lake belong to the Konth granite suite of the TMZ (McGlynn *et al.*, 1974; Bostock and van Breemen, 1994). Dyke material from this location yields an emplacement age of 1830 Ma (U-Pb in baddeleyite;

Heaman, pers. comm.).

On the basis of similarity in petrography and trend between the suites, Ewanchuk (2006) made the tentative correlation of the dykes at Tsu Lake with those of the Sparrow Dyke Swarm. The similarity in age of the Taltson River dyke and the Jerome Lake dyke, as indicated above, supports this correlation.

2.2.3 The Martin Group Igneous Rocks

Located near Uranium City, SK, the Martin Group of siliciclastic rocks is exposed over an area of ∼3000 km^2 (Morelli *et al.*, 2009). Interbedded with these sedimentary rocks are mafic dykes, sills and volcanics (the Martin Group Igneous Rocks, MGIR). The geochemistry of the MGIR were studied by Morelli (2000) and Morelli *et al.* (2009), who came to the conclusion that the dykes, sills and volcanics were sourced from a heterogeneous depleted-MORB mantle that underwent subduction-related modification. Morelli *et al.* (2009) also obtained a U-Pb (baddeleyite) date of 1818 ± 4 Ma from one of the dykes (RM-37d), slightly younger than the age of the dyke at Jerome Lake and the one at the Taltson River location (see above). This is, however, within the range of ages for the CIF (see below) and strengthens the correlations of the Martin Group with the Baker Lake Group, of which the CIF is a part (Ashton *et al.*, 2009). Ashton *et al.* (2009) do not attribute the CIF and the MGIR to a common source, but instead suggest that the Sparrow dykes are related to the dykes of the MGIR (which also trend ∼130°; Morelli, 2000). Ashton *et al.* (2009) suggest that the CIF is associated with the lamprophyres found in the eastern Beaverlodge domain.

2.2.4 The Christopher Island Formation

The CIF is the largest known ultrapotassic province in the world, emplaced over an area of 200,000 km^2 at *ca.* 1830 Ma (Peterson *et al.*, 1994; Cousens *et al.*, 2001, 2004; Rainbird *et al.*, 2006). The rocks are dominantly minettes and lamprophyres (Peterson *et al.*, 1994), found as dykes from Rankin Inlet, NU, to Uranium City, SK (Cousens *et al.*, 2004). As per Cousens *et al.* (2001, 2004), incompatible element concentrations of these rocks are characteristic of melts derived from a subduction-modified source and their high carbonate content requires that CO_2 be present in their source. In addition to their ultrapotassic nature, the REE concentrations of the CIF samples are very enriched relative to the Primitive Mantle (Cousens *et al.*, 2001). Additionally, ϵNd vaules of -6 to -12 are not correlated with geochemical monitors of crustal contamination (Cousens *et al.*, 2001, 2004). Cousens *et al.* (2001, 2004) interpret these geochemical characteristics to reflect a source modified by Neoarchean subduction and metasomatism. This model is disputed by Peterson *et al.* (2002, 2010), who favour a model whereby middle crustal layers were imbricated in the lithosphere beneath the Churchill craton at *ca.* 1.9 Ga, during the assembly of the supercontinent Nuna. Melting of this crustal material by the hotter surrounding mantle would impart the observed geochemical signatures (Peterson *et al.*, 2002, 2010).

Irrespective of which enrichment model is preferred for the CIF, it is clear that its mantle source was enriched over a large area. That the CIF magmas were emplaced at approximately the same time as the Sparrow Dyke Swarm, the Tsu Lake dykes and the MGIR indicates that the mantle beneath the Churchill craton in the Paleoproterozoic exhibited large-scale heterogeneity.

In the case of the MGIR, the CIF may also be spatially proximal, if the lamprophyre dykes of the eastern Beaverlodge domain are indeed of CIF affinity (Ashton *et al.*, 2009).

2.3 The Trans-Hudson Orogeny

As indicated in the excellent reviews by Hoffman (1988) and Corrigan *et al.* (2009), the *ca.* 1830 Ma time period marks the beginning of the terminal collision phase of the THO. The following summary of the THO is derived from that review, unless otherwise stated. The THO is the largest Paleoproterozoic orogenic belt in the world, extending from as far northeast (present-day coordinates) as Scandinavia and at least as far south as Dakota and possibly up to the Grand Canyon area. The THO was the result of the closure of the Manikewan Ocean that separated the Churchill and Superior cratons over the period from *ca.* 1.92–1.8 Ga (Ansdell, 2005, and references therein). This orogeny, as exposed in northeastern Canada and the prairie provinces, involved three distinct crustal blocks: the Superior craton to the southeast, the obscure Sask craton in the southwest and the Churchill Province (specifically, the Hearne Domain) in the north and northwest.

The amalgamation of these cratons and the subduction of intervening oceanic crust resulted in the emplacement of various active margin igneous suites, such as the Porter Bay Complex and Wathaman Batholith (Maxeiner and Rayner, 2011, and references therein), and the accretion of oceanic arcs, such as the LaRonge-Lynn Lake belts and Flin Flon-Glennie Complex. On the Superior craton side, the Molson Igneous Events at 1880 Ma (Heaman *et al.*, 2009) include mafic dykes that were emplaced parallel to the margin of the

THO.

Although ∼900 kilometres at its widest, the metamorphic footprint of the THO is asymmetrically distributed, with only a narrow zone of metamorphism on the Superior craton. Because the Churchill Province was being formed by the accretion of terranes and smaller crustal blocks over the 120 million year course of the THO, it would have a hotter and rheologically weaker lithosphere. This would be comparatively easier to metamorphose than the colder and more rigid Superior craton, resulting in the asymmetry of the the metamorphic footprint.

Chapter 3

Methods and Results

3.1 Field-work

The samples investigated in the present study are from two main areas, the southeastern part of the NT and northwestern SK. Forty one samples from the NT, each comprising approximately a kilogram of fist-sized blocks, were collected from lake shore outcrops of fourteen mafic dykes and wall-rock lithologies, accessed by floatplane from Fort Smith, NT. These locations were selected from historic maps from the Geological Survey of Canada that indicate diabase dykes trending $\sim$130° in the region between Great Slave Lake and Fort Smith, NT (Henderson, 1939a,b; Wilson, 1941; McGlynn, 1978; Bostock, 1982). The dykes and sample locations are shown in Figure 3.1 along with linear features discovered by an airborne magnetic survey that overlapped the northeastern portion of this area (NTGO, 2007). Table 3.1 indicates the number of dyke and other samples collected, although only the mafic samples will be considered for this study.

Of the 41 samples collected, 32 are from the mafic dykes (chill-margin and core, where possible), 5 are country rock samples and 1 is from a felsic

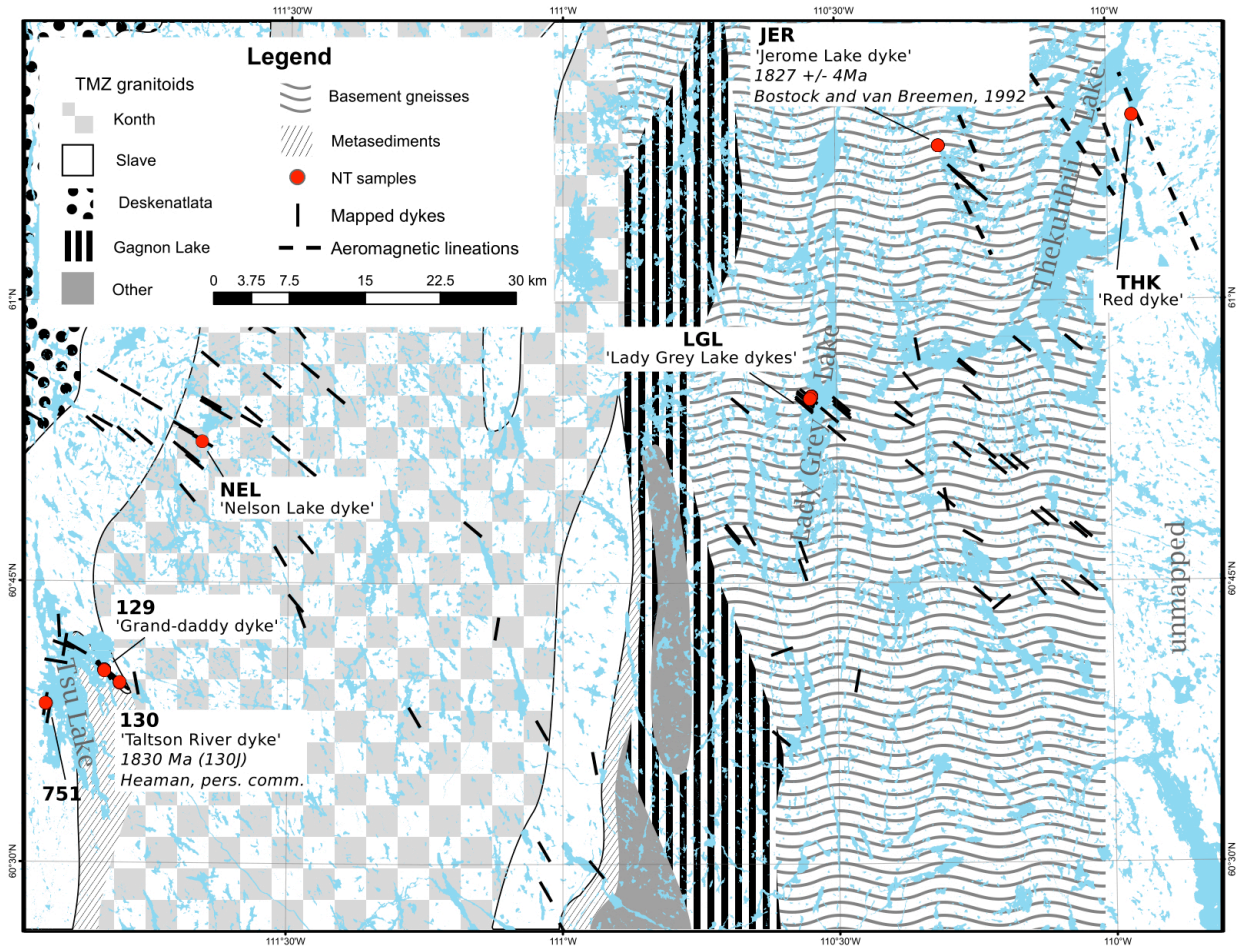

Figure 3.1: Historically mapped dykes (see text) and locations of the NT samples studied in the present work. Tsu Lake locations are as per Ewanchuk (2006). Geology (including 'unmapped' area) are as per Chacko *et al.* (2000).

Table 3.1: Number of NT samples collected by the author. The number of samples collected by Ewanchuk (2006) at locations at Tsu Lake are indicated in parentheses. Provided next to the lake name is the identifier used for the naming scheme in Table A.1.

Location name (identifier)	Location number	Number of dykes	Number of samples	
			Mafic	Other
Tsu Lake (129)	129	1	11 (10)	2; granite
Tsu Lake (751)	751	1	2 (1)	-
Tsu Lake	004	-	- (1)	-
Taltson River (130)	130	1	2 (3)	2 (2; granite)
Nelson Lake (NEL)	-	1	2	-
Jerome Lake (JER)	-	1	5	1; felsic dyke
Thekulthili Lake (THK)	-	1	-	3; red samples, 1; quartzite?
Lady Grey Lake (LGL)	-	7	10	-

dyke cross-cutting the Jerome Lake dyke. Three dyke samples, collected at Thekulthili Lake, are unique for their penetrative rusty red colour in hand-specimen. Measurements of dyke width and orientation of wall-rock contacts were taken where possible (recorded, with the dykes' locations, in Table A.1). Wall-rock contacts of all sampled dykes are generally sharp (Figure 3.2a,b,f), and trend ∼130°, with the exception of the dyke at location 751 (Ewanchuk, 2006), which trends ∼000° with an undulating contact. Some dykes show wall-rock xenoliths within the main body of the dyke (e.g., 'X Dyke' at location 129; Figure 3.2c; Ewanchuk, 2006). Only the dyke at location 751 shows irregular wisps of country rock within the dyke body.

The sampled dykes are generally 1-2 metres wide, although the 'Grand-daddy Dyke' (location 129; Ewanchuk, 2006) is 50 metres wide and the Jerome Lake dyke is at least 40 metres wide (the exposure is on a small island in Jerome Lake and the contacts are inferred to be present in the lake) . The latter is a coarse-grained gabbro throughout the exposure, whereas the Grand-daddy

Dyke shows numerous textural types. The textures and sample locations across the Grand-daddy Dyke are indicated in a sketch map (Figure 3.3). Photos of some of the textural features of this dyke and others are shown in Figure 3.2.

Twenty one dyke samples, with limited descriptive notes, were also received from Dr. Kenneth Ashton, at the Saskatchewan Geological Survey, collected around Uranium City, SK, over multiple field seasons from 2000 to 2010. Geochemical analyses of 6 additional samples were also provided. Only 18 of the 27 analyses are used in this study as the remaining samples were described as foliated or silicified. Three samples are similar in appearance to the Thekulthili Lake dyke and these 6 rusty red samples will be collectively referred to as the 'red dykes'. These sample locations are shown in Figure 3.4.

Henceforth, all samples collected in the Northwest Territories, including the fourteen samples from ∼130°-trending dykes sampled by Ewanchuk (2006), will be referred to as the 'NT samples'. The samples from Saskatchewan, including twenty from Morelli *et al.* (2009) will be referred to as the 'SK samples'.

3.2 Petrography

Hand-specimens of the NT and SK samples, with the exception of the red dykes, are all medium to dark grey rocks. Crystal size in the samples is either fine or coarse, with fine-grained samples being more common than the coarser ones. Certain samples are plagioclase-phyric, showing crystals up to a centimetre long (e.g., RD10-129-07). The red dykes show a penetrative rusty red coloration and plagioclase laths up to a centimetre long in a very fine-grained matrix. There are vugs sparsely distributed in this rock type, up

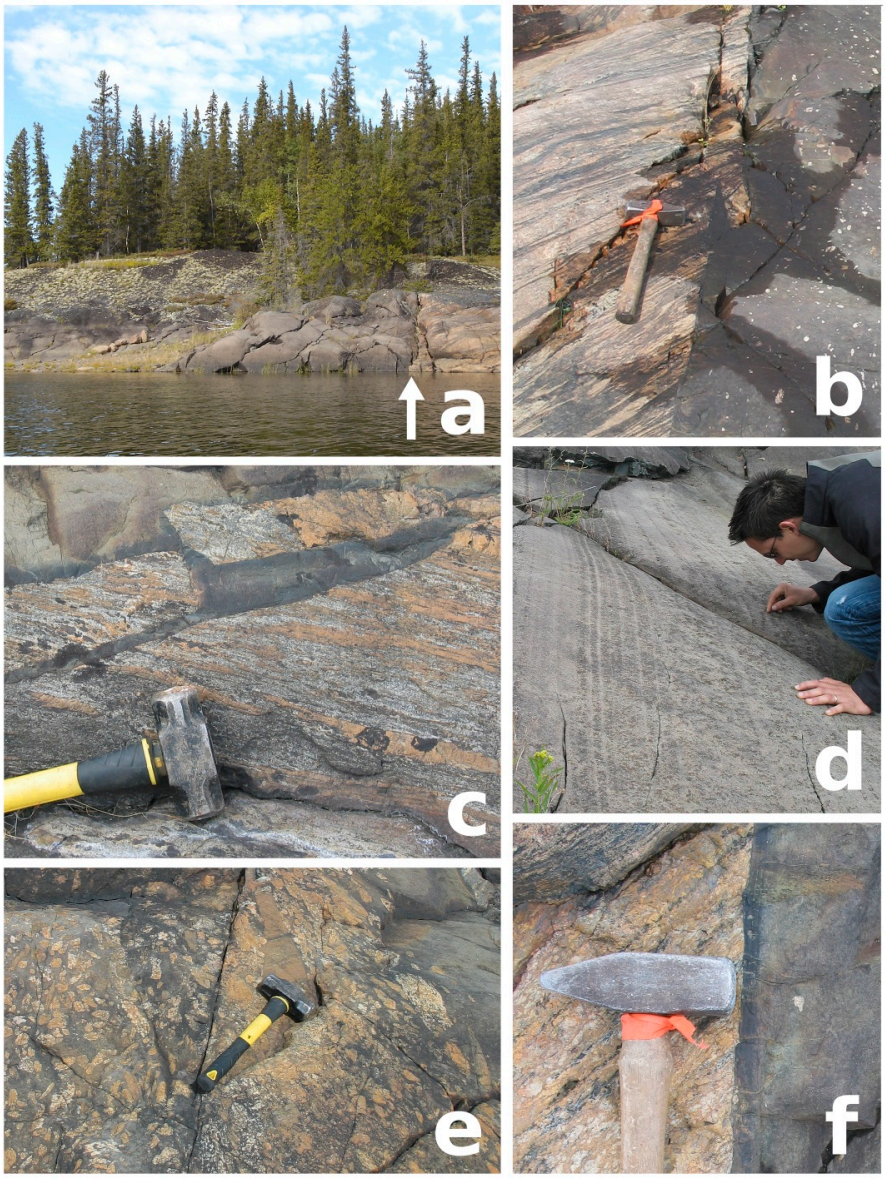

Figure 3.2: Photos of textural types observed in dykes at Tsu Lake, NT; (a) general view of location 129, showing northern contact of the 'Grand-daddy Dyke' (courtesy Dr. Thomas Chacko); (b) contact of the 'Papa Dyke' displaying wall-rock 'ripping'; (c) close-up of wall-rock 'ripping' at the 'X Dyke'; (d) magmatic layering observed at the 'Grand-daddy Dyke' (Ivan Bourque, pilot, pictured); (e) granitic xenoliths in the 'X Dyke'; (f) chill-margin observed at the 'Mama Dyke'. Photos courtesy Dr. Larry Heaman, except as noted.

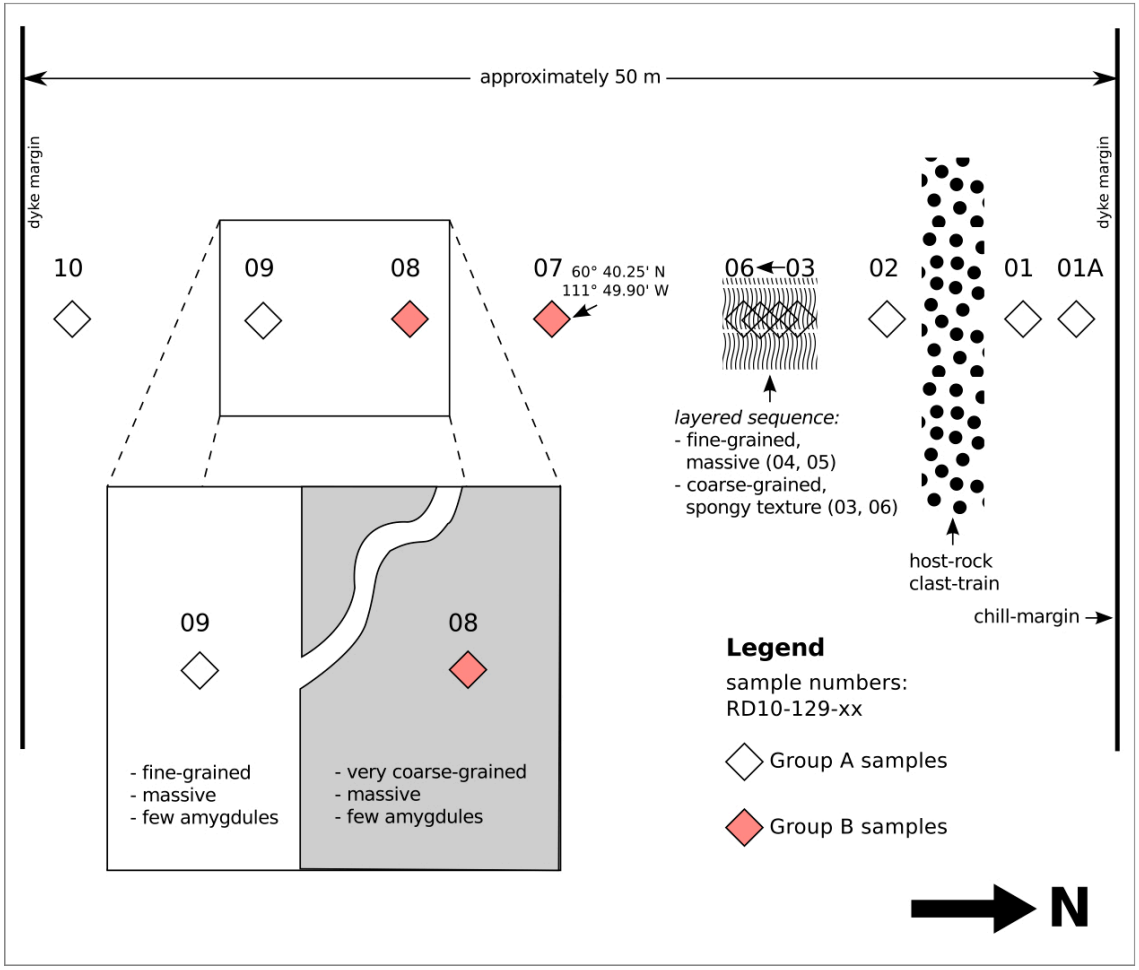

Figure 3.3: Schematic map of the 'Grand-daddy Dyke' at Tsu Lake, NT, showing sample locations coded by REE profile-defined groups (Chapter 3.3.4). It is observed that Group A cuts across Group B, indicating that it is a younger intrusion.

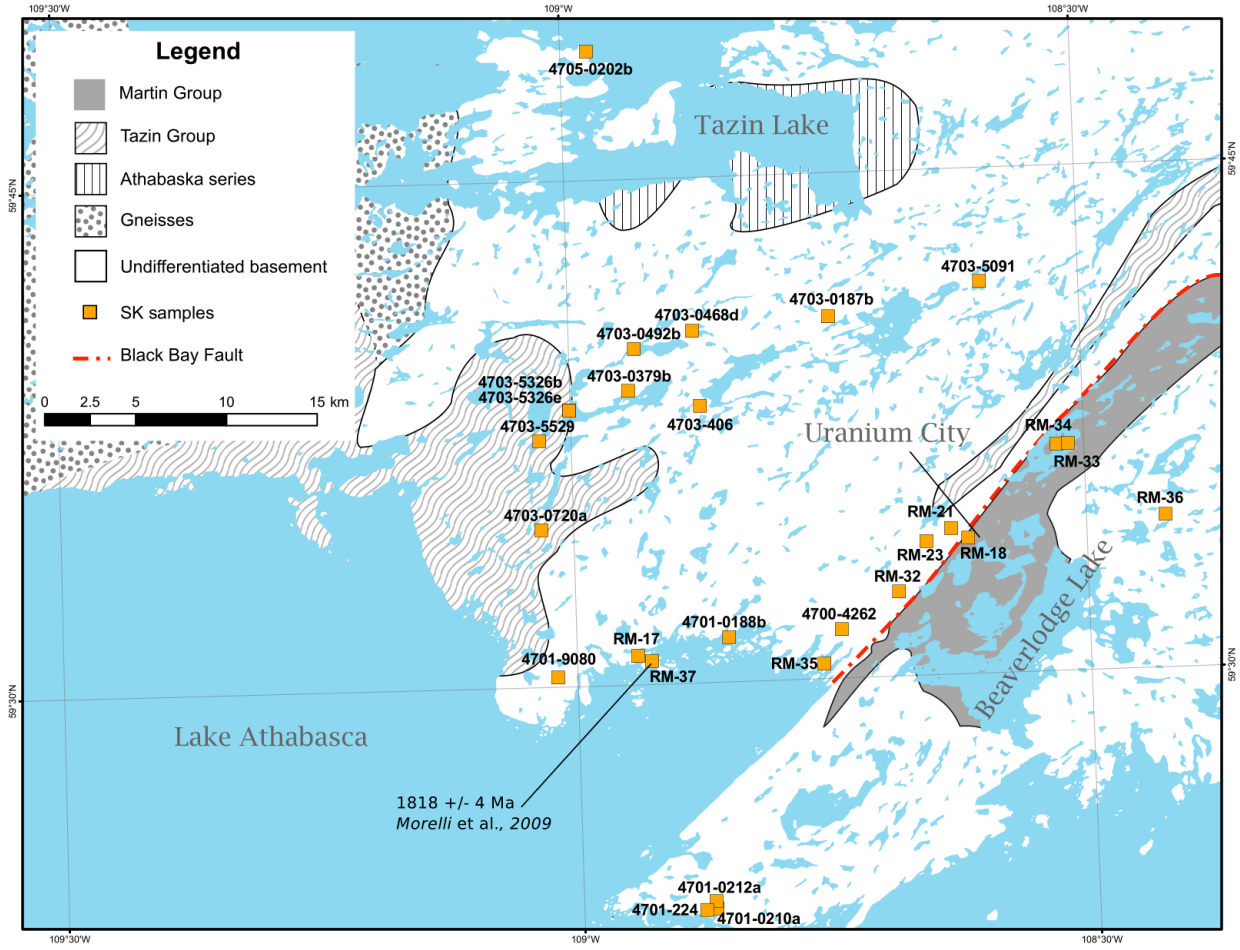

Figure 3.4: Locations of samples from Morelli *et al.* (2009) and those provided by K. Ashton. Geology as per Alcock (1936); 'Martin Group' as per Morelli *et al.* (2009).

to a centimetre in diameter, filled with pale-green crystals of epidote.

Petrographic thin-sections were prepared from 20 hand-samples (14 from the NT dykes and 6 from the SK dykes). Detailed descriptions of these thin-sections are provided in Appendix B. In summary, the NT and SK sample sets are quite similar and, besides crystal size, there is little petrographic difference between the fine-grained and coarse-grained samples. The mafic dykes are dominated by plagioclase and clinopyroxene, although the latter is generally extensively altered to amphibole or chlorite. The plagioclase in the samples displays variable alteration, from minimal (e.g., RD10-NEL-01) to extensive (e.g., RD10-LGL-03). It is not uncommon to find quartz intergrowing with plagioclase in granophyric patches (e.g., RD10-129-07, RD10-JER-04). Opaque minerals are generally 2–5% in modal abundance (e.g., RD10-NEL-01), but can be as high as 10% (e.g., RD10-751-01). The thin-section of RD10-JER-05A and RD10-LGL-01 show calcite to be present, though it is likely secondary in the latter sample. Thin sections of the red dykes (i.e., RD10-THK-03 and 4705-5326a) indicate that their colour is caused by a pervasive alteration of the plagioclase crystals in the groundmass and those that make up phenocrysts.

3.3 Whole-rock geochemistry

Samples were cut into slabs, broken to chips and then split into two aliquots. One of these was crushed in a tungsten-carbide ring-and-puck mill (WC mill), whereas the other was crushed in an agate mill. The crushing procedure (detailed in Appendix C) included a thorough cleaning of crushing equipment between samples to ensure that the potential for cross-contamination was min-

imized. Major-elements (reported as oxide weight percentages; wt.%)[1] and selected trace elements (reported in parts per million; ppm)[2] were analyzed by X-Ray Fluorescence spectrometry (XRF) at the Geochemical Laboratories, McGill University, Québec, Canada, using the WC milled samples to avoid major element contamination from the agate mill. Minor, trace and rare earth elements[3] were analyzed by inductively coupled plasma mass spectrometry (ICP-MS). For the ICP-MS analyses, the agate milled samples were used to reduce the contamination in trace elements from the WC mill. ICP-MS analyses were done on an Elan 6100 instrument at the Radiogenic Isotope Facility (RIF), at the University of Alberta.

Whole-rock geochemical results are provided in Appendix D.1, whereas Appendix D.2 lists duplicated analyses and analyses of the BCR-2 basalt standard, which respectively indicate the good repeatability and high accuracy of the ICP-MS analytical procedure. The samples reported in Ewanchuk (2006) were analyzed by the FUS-ICP and FUS-MS methods at Actlabs (Ancaster, Ontario, Canada). Appendix D.3 compares the analyses for samples from location 751 in that study and this one. As this indicates good agreement between the methods, the data from Ewanchuk (2006) will be considered together with the data from this study, even where samples have been taken at the same outcrop.

The analyses from Morelli *et al.* (2009) were obtained by a combination of XRF (X-Ray Assay Laboratories in Don Mills, Ontario, Canada) and ICP-MS (University of Saskatchewan). The analyses provided by Dr. Ashton were

[1] SiO_2, TiO_2, Al_2O_3, Fe_2O_3*, MnO, MgO, CaO, Na_2O, K_2O and P_2O_3.

[2] Ba, Ce, Co, Cr, Cu, Ni, Sc, V, Zn, Ga, Nb, Pb, Rb, Sr, Th, U, Y and Zr.

[3] Be, V, Cr, Mn, Co, Cu, Zn, As, Rb, Sr, Y, Zr, Nb, Mo, Cd, Sn, Sb, Cs, Ba, La, Ce, Nd, Sm, Eu, Gd, Tb, Dy, Ho, Er, Yb, Lu, Hf, Ta, Tl, Pb, Th and U.

obtained from Actlabs, using their '4Lithores' package (ICP and ICP-MS).

In the following subsections, the NT and SK samples will each be separated into their coarse and fine-grained components to evaluate differences in geochemistry, if any, between these. The red dykes from the two sample sets will be treated as a separate group.

3.3.1 TAS diagrams

A TAS (Total Alkali vs. Silica) diagram, Figure 3.5, is used to determine the names applicable to these samples (data recalculated to 0% loss on ignition, as per Le Maitre, 2002). The coarse-grained NT samples cluster tightly as basaltic andesites with SiO_2 between 52.2 to 54.6 wt.%, and total alkali content between 2.0 and 3.6 wt.%. The coarse-grained SK samples share this field with the NT samples, though they show higher and more consistent alkali contents (4.3 to 4.8 wt.%) than the NT samples, but greater variation in silica (51.8 to 56.7 wt.%). Also seen in Figure 3.5 are six NT samples that plot at higher silica and total alkali values (56.7 to 62.4 wt.%, and 3.0 to 6.2 wt.%, respectively). Of these, the three with the highest SiO_2 content (circled with a dashed line) are from the dyke at location 751 which, as described above, trends $\sim 000°$.

The three samples within the dotted line are:

RD10-JER-01, (SiO_2 = 58.76 wt.%) is from a section of the Jerome Lake dyke that appears faulted,

RD10-JER-05A, (SiO_2 = 56.16 wt.%) is also from the Jerome Lake dyke, next to the the contact with a cross-cutting felsic dyke, and

130B, (SiO_2 = 57.39 wt.%; from Ewanchuk, 2006) is from the northern mar-

gin of the Taltson River dyke (Tsu Lake location 130), where "syenogranite blobs" are found (Ewanchuk, 2006).

The NT samples from the dyke at location 751 will henceforth not be considered in this study on the basis of the very different trend and morphology of that dyke, indicating that it may be from a separate, unrelated event. The position of these samples away from the clusters of the NT and SK samples (with no intermediate samples) supports the assertion that they are likely unrelated to the rest of the NT samples.

The observations at the specific sample locations of the Jerome Lake and Taltson River dykes (listed above), indicate that they may represent dyke material that is potentially altered or mixed with other lithologies. These assertions are supported by the separation of these samples from the NT sample cluster although they are physically part of the dykes of interest. For this reason, these samples will also be excluded from the remaining description of results and the following discussion.

Although the fine-grained samples of each sample set overlap significantly with the the coarse-grained ones, they show a spread to lower SiO_2; i.e., 50.5 vs. 52.3 wt.% for the least silica-enriched fine- and coarse-grained NT samples, respectively, and 47.0 vs. 51.8 wt.% for the least silica-enriched fine- and coarse-grained SK samples, respectively. The fine-grained samples also show higher concentrations and greater range of alkali content than the coarse-grained samples; i.e., 2.1 to 5.3 wt.% and 2.0 to 3.9 wt.% for the fine- and coarse-grained NT samples, respectively, and 2.1 to 7.4 wt.% and 3.4 to 4.2 wt.% for the fine- and coarse-grained SK samples, respectively.

The red dyke samples show higher alkali and silica concentrations than the

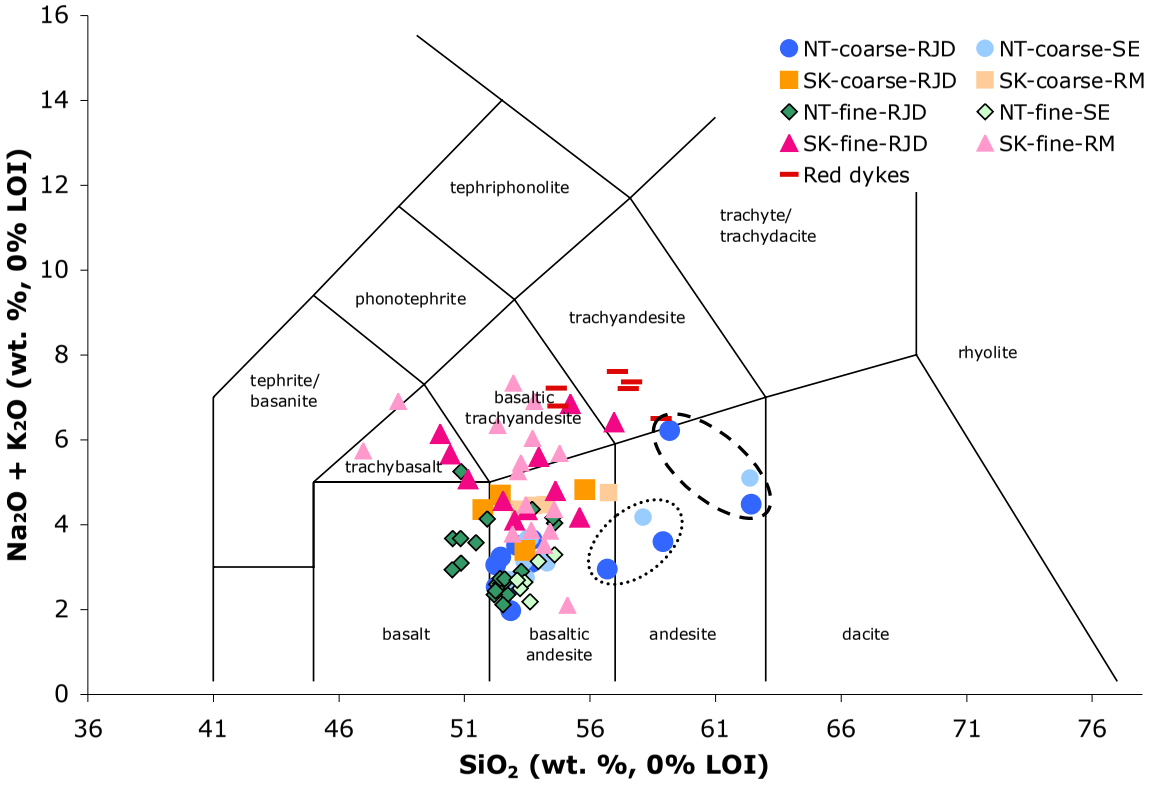

Figure 3.5: TAS diagram for NT and SK samples. All data recalculated to 0% LOI, as per Le Maitre (2002). Suffix '-RJD' indicates that the samples were processed as part of this study; suffixes '-SE' and '-RM' indicate samples whose data comes from Ewanchuk (2006) and Morelli *et al.* (2009), respectively. It is observed that the red dykes are amongst the most alkaline and silica rich samples, that the SK samples are in general more alkaline than the NT samples and that there is little correlation between the crystal size of the samples and position of the TAS diagram. Discussed in the text are the samples within the dashed loop (from location 751) and within the dotted loop (130B, RD10-JER-01 and RD10-JER-05A).

NT samples. Although they overlap in both these parameters with the SK samples, their distinctly different physical appearance precludes the merging of these sample sets.

3.3.2 Harker diagrams

Major-element variation diagrams (Harker diagrams) have been plotted for both sample sets in Figure 3.6. It is observed, as in the TAS diagram (Figure 3.5), that the NT samples show tighter clustering in SiO_2 compared to the SK samples and that the fine-grained samples extend to lower SiO_2 concentrations (despite great overlap with the coarse-grained samples of each suite). The NT and SK sample sets show similar TiO_2, Al_2O_3, Na_2O and MgO content. The NT samples show generally higher Fe_2O_3 and CaO than the SK samples, whereas the K_2O and P_2O_5 contents of the SK samples are lower than for the NT samples.

3.3.3 Choice of normalization

All Rare Earth Element (REE) and incompatible element data in this study will be normalized to the the values of Enriched MORB (E-MORB; Sun and McDonough, 1989). The rationale for this choice is illustrated in Figure 3.7, which shows that the E-MORB normalization consistently gives the flattest REE profiles of the analyzed samples compared to the other choices of normalization. This is preferred by the present author as deviations from a flat pattern are easy to detect visually and mathematically. These deviations can aid in sample grouping and detecting outliers.

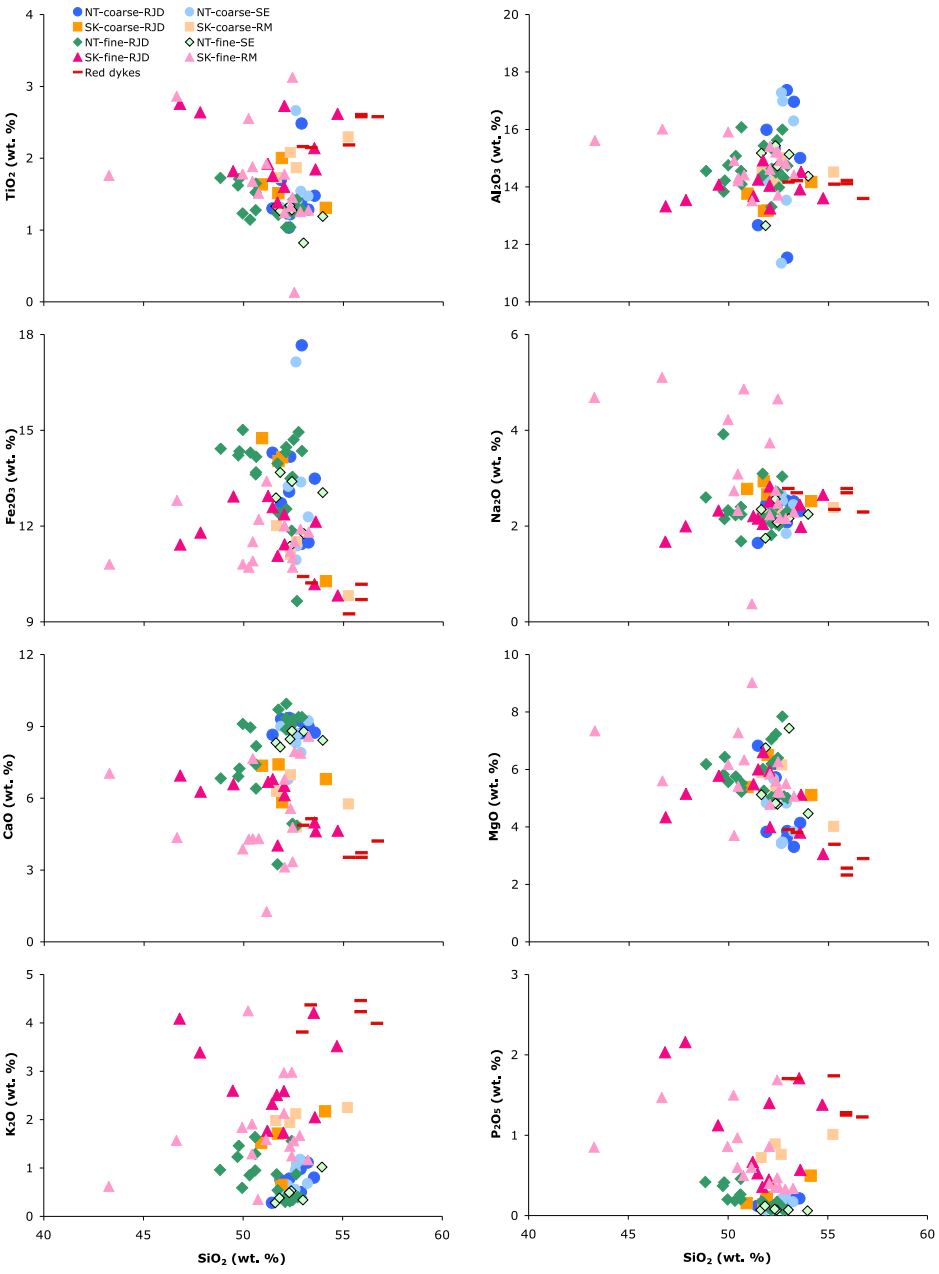

Figure 3.6: Harker diagram for NT and SK samples. Symbols as per Figure 3.5.

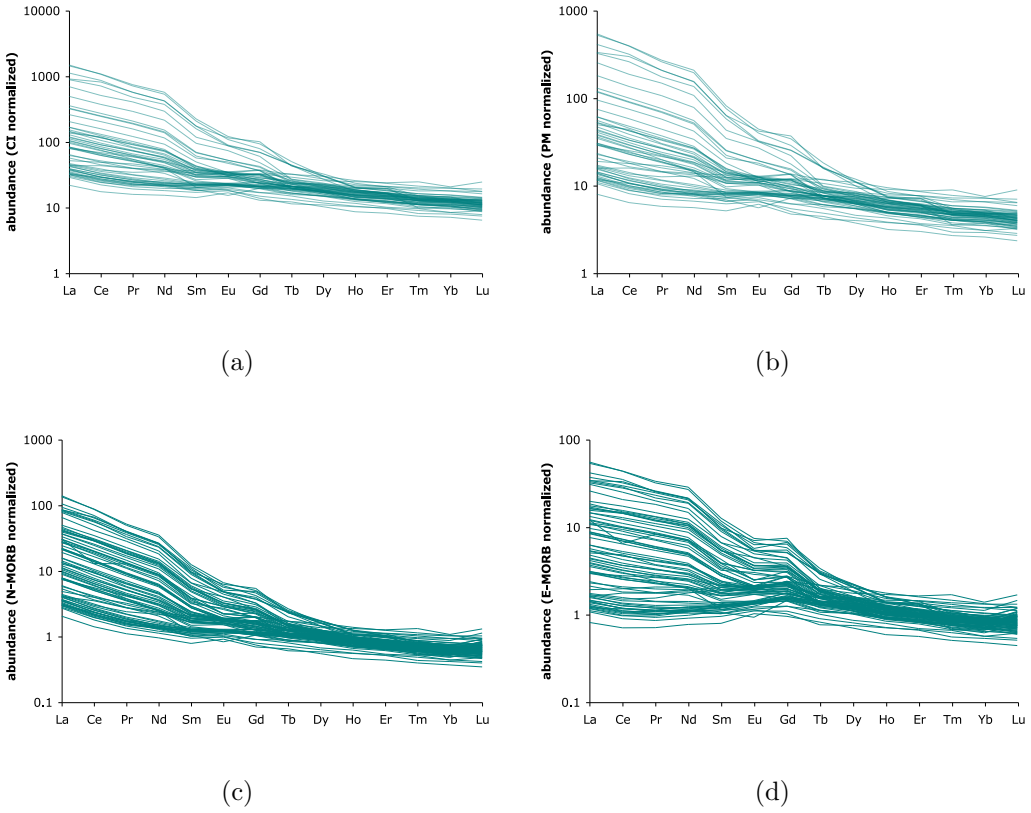

Figure 3.7: Comparison of possible normalization choices: (a) CI chondrite (McDonough and Sun, 1995); (b) Primitive Mantle (McDonough and Sun, 1995); (c) Normal-MORB (Sun and McDonough, 1989); (d) Enriched-MORB (Sun and McDonough, 1989). The E-MORB normalization is selected for this study as the REE profiles are the flattest making it easier to detect deviations from the general trend.

3.3.4 Rare earth element profiles

E-MORB-normalized (Sun and McDonough, 1989) REE profiles for the NT and SK samples are shown in Figure 3.8. It is apparent from these diagrams that all the samples are similar in Heavy REE (HREE) abundance. However, the majority of SK samples show greater Light REE (LREE) and Middle REE (MREE) enrichments than the NT samples; i.e., between $\sim$10$\times$ and $\sim$100$\times$ E-MORB for the SK samples and $\sim$1$\times$ to $\sim$10$\times$ E-MORB for the NT samples. Additionally, there appears to be no correlation of REE enrichment with the petrography of the samples. Although the red dykes show very elevated REE profiles compared to the NT samples, they have REE abundances similar to the most enriched SK samples.

As the major feature in Figure 3.8 is the slope of the profiles, it is helpful to visualize the difference in slope between samples by plotting the values of the LREE to MREE slope (i.e., $(La/Sm)_N$) against the MREE to HREE slope (i.e., $(Sm/Yb)_N$), as in Figure 3.9. Although there are distinct clusters formed on this plot, these clusters are not related to petrography. Group A on this figure shows a relatively unsloped profile, with $(La/Sm)_N$ of 1 to 1.5, and $(Sm/Yb)_N$ under 2. Group B shows steeper slopes (i.e., $(La/Sm)_N$ from 1.8 to 3.2, $(Sm/Yb)_N$ from 1.7 to 3.4). Group C shows still steeper slopes, with $(La/Sm)_N$ from 2.6 to 4.7 and $(Sm/Yb)_N$ from 3.9 to 17. Group A is dominated by NT samples, but also includes three SK samples. Although there is minimal overlap between Groups B and C, Group B is exclusively composed of NT samples, whereas Group C is exclusively SK samples. Note that although the red dykes fall along the Group C trend, their very different nature precludes their inclusion in this group. The REE profiles in Figure 3.10

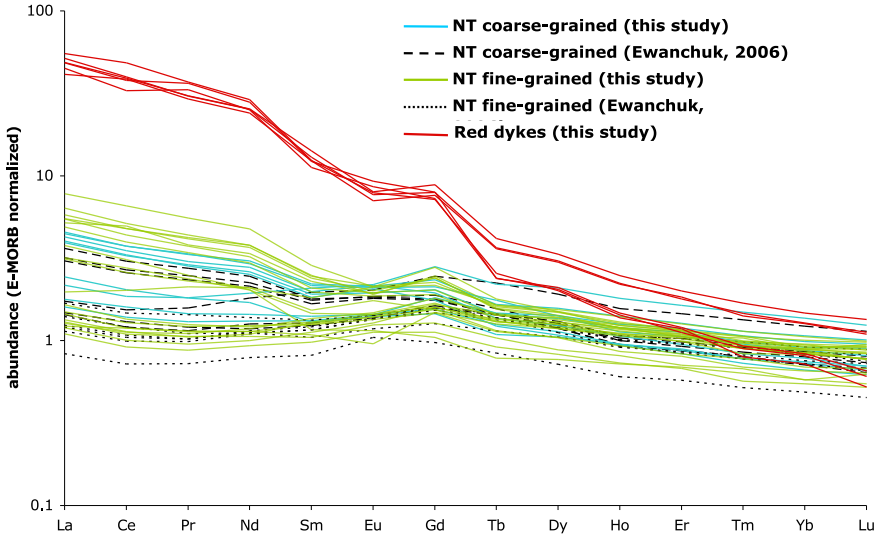

(a)

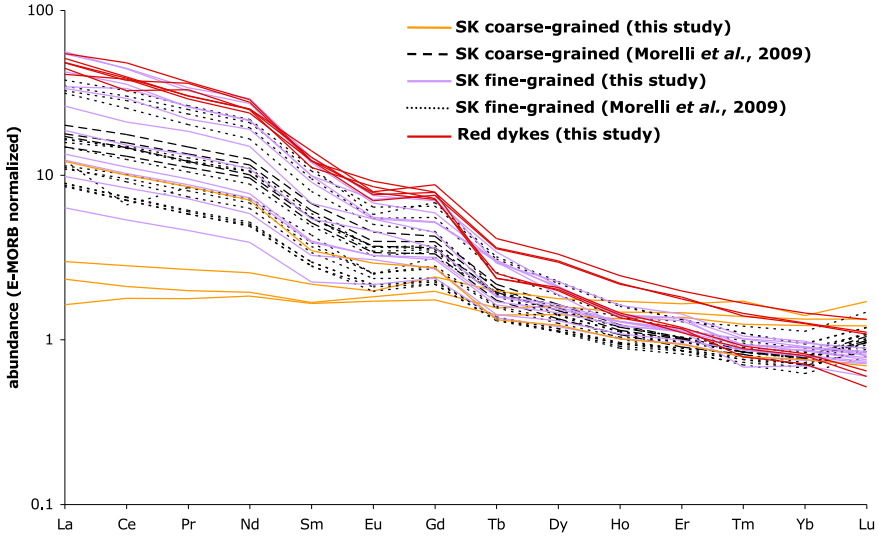

(b)

Figure 3.8: E-MORB normalized (Sun and McDonough, 1989) REE profiles, sorted by location and crystal size, for (a) NT and (b) SK samples.

have been coded according to the groups observed in Figure 3.9.

3.3.5 Spidergrams

'Spider diagrams' (or 'spidergrams') are used to display the variation in abundance of incompatible elements between samples. Here, the choice and order of elements displayed is from Pearce (1983), modified to show lanthanum instead of cerium, with element concentrations normalized to E-MORB (Sun and McDonough, 1989). As per Pearce (1983), the x-axis is arranged so that the Large Ion Lithophile Elements (LILE) are on the left (i.e., Sr, K_2O, Rb, and Ba), whereas the remainder of the elements (on the right) are the High Field Strength Elements (HFSE). Spidergrams for the NT and SK samples are provided in Figure 3.11. These show no correlation of geochemistry with petrography in either sample set, as with the REE profiles. Also as with the REE profiles, the red dykes are more enriched than the NT samples, but similar to the most enriched SK samples.

Coding the samples by REE group (as previously defined) shows a more distinct grouping, as observed in Figure 3.12. The HFSE portions of the profiles for each group are similar to the REE profiles in that Group A is least enriched, Group C is most enriched and Group B is intermediate. Each of these groups show distinct negative Nb anomalies and elevated abundances of the LILE relative to the HFSE. Between groups, the abundance of the LILE generally shows enrichment from Group A to C. However, the majority of Group C samples display E-MORB-like Rb abundance whereas K_2O and Ba are very enriched, resulting in very sharply negative rubidium anomalies.

The red dyke samples are remarkably coherent in the LILE and HFSE.

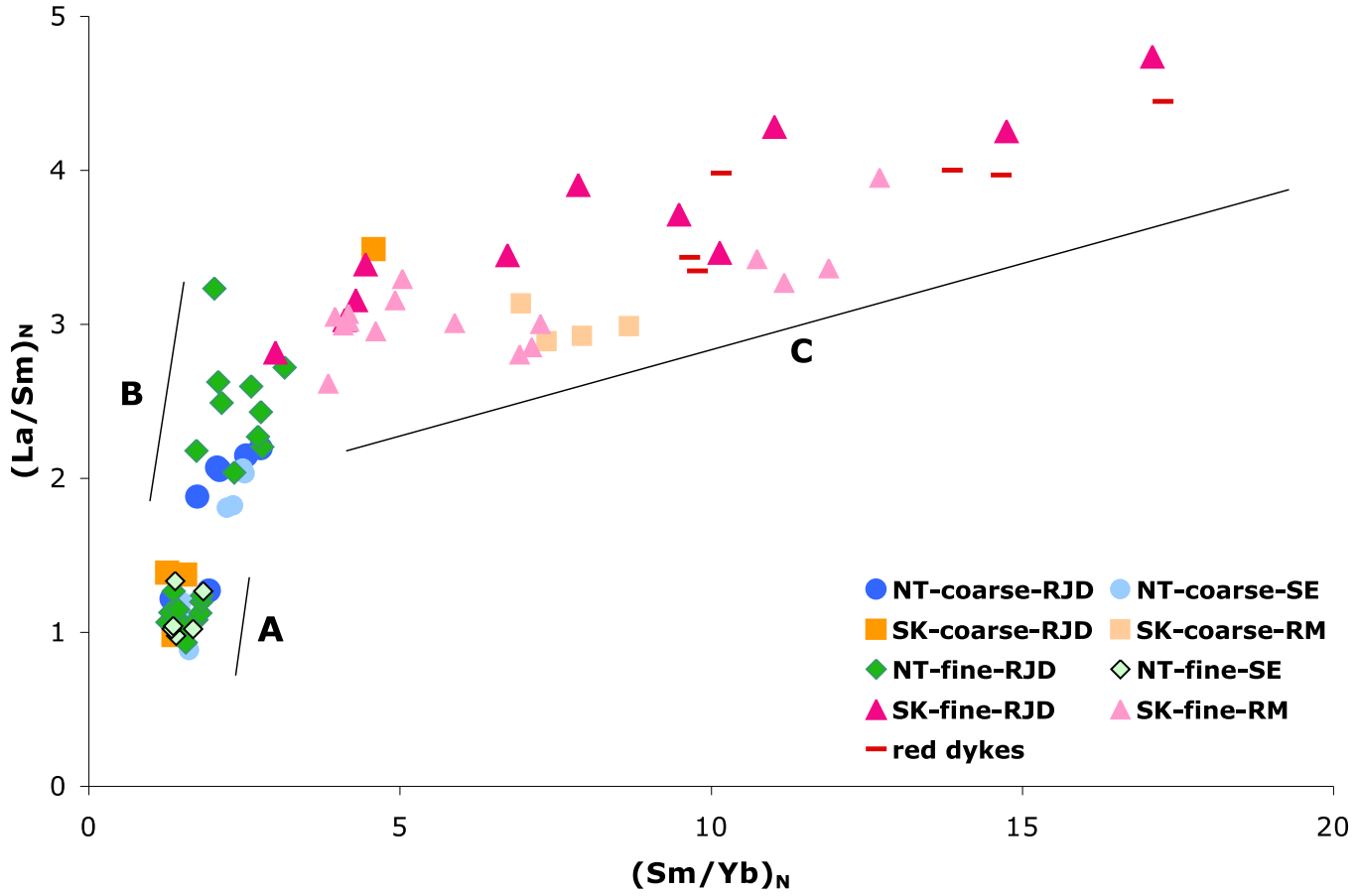

Figure 3.9: La/Sm vs. Sm/Yb (E-MORB normalized, Sun and McDonough, 1989) of NT and SK samples. It is observed that the data splits into three groups, as indicated. 'A, B and C' refer to the names given to these groups. Furthermore there is no link observed between crystal size and grouping.

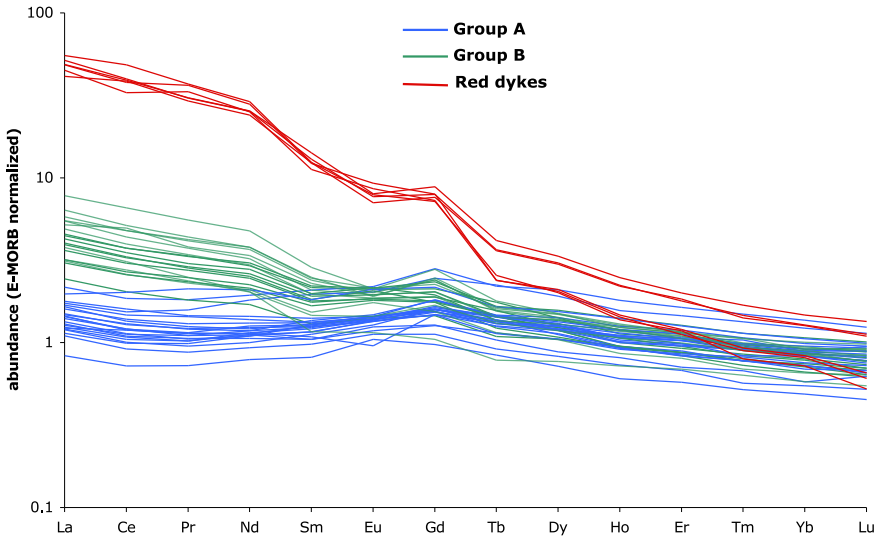

(a)

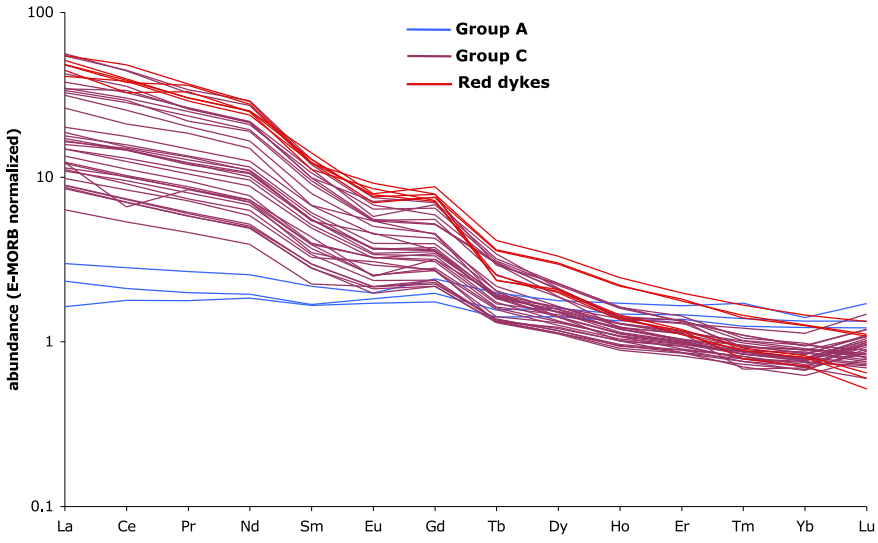

(b)

Figure 3.10: REE profiles (E-MORB normalized; Sun and McDonough, 1989) grouped as per Figure 3.9 for (a) NT and (b) SK samples.

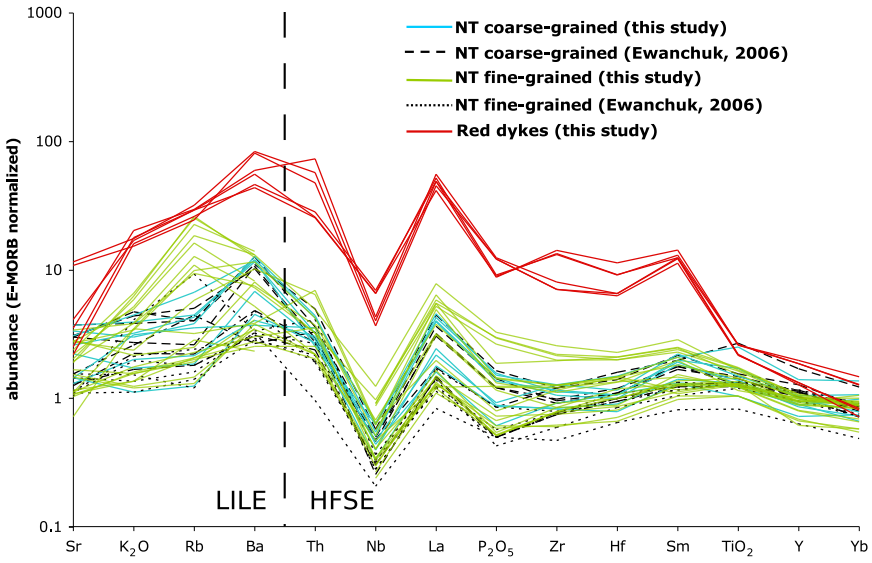

(a)

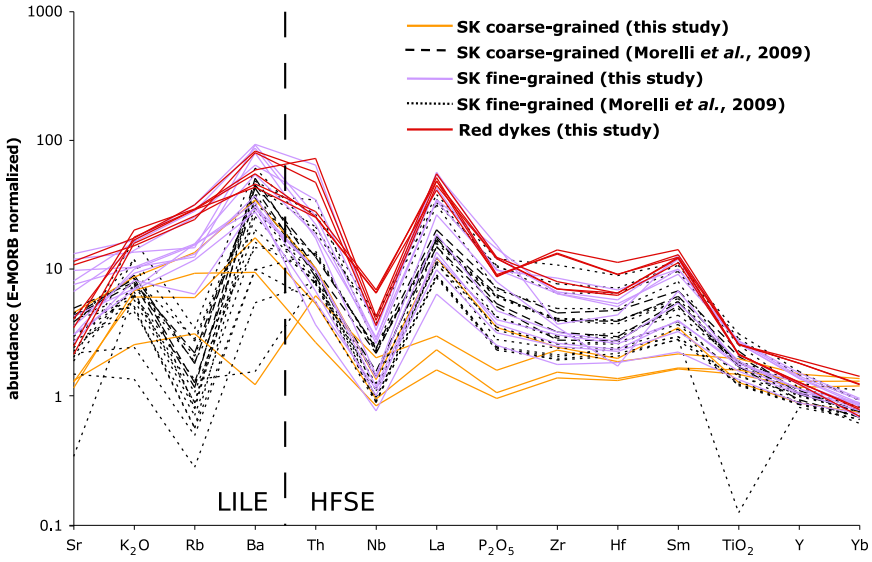

(b)

Figure 3.11: E-MORB normalized (Sun and McDonough, 1989) spidergrams (after Pearce, 1983), sorted by location and crystal size, for (a) NT and (b) SK samples.

Relative to the other samples, they display the most elevated abundance in all elements, except Sr, Ba, P_2O_5, TiO_2, Y and Yb.

3.4 Field-relationships between Groups A and B.

The only contact relationship directly observed between rocks of Groups A and B occurs at the 50 metre wide 'Grand-daddy dyke' (Ewanchuk, 2006), at location 129 at Tsu Lake. There, as illustrated in Figure 3.3, the Group B samples are found only in the centre of the body, whereas the Group A samples come from the margins. Near the south margin, the Group A lithology is observed cutting across Group B. It is notable that the Group A rock displays no chill-margin at the contact with the intruded rock, although it clearly shows one at the northern contact with the country rock.

At Lady Grey Lake, samples RD10-LGL-05A and RD10-LGL-05 from the contact and core, respectively, of a 1 metre wide dyke, are from Group A and B, respectively. Although the samples are clearly adjacent and from a single body, the contact relationship was obscured.

3.5 Sm-Nd and Rb-Sr isotopic geochemistry

In order to derive information regarding the sources and possible contamination of the samples of this study, Sm-Nd and Rb-Sr isotopic analysis was carried out. Samples were selected for analysis so as to represent the spread of data observed in Figure 3.9. The selected samples are listed in Table 3.2.

Agate milled aliquots of selected whole-rock samples were prepared and analyzed at the RIF by Dr. Robert Creaser. The procedures of Creaser *et al.*

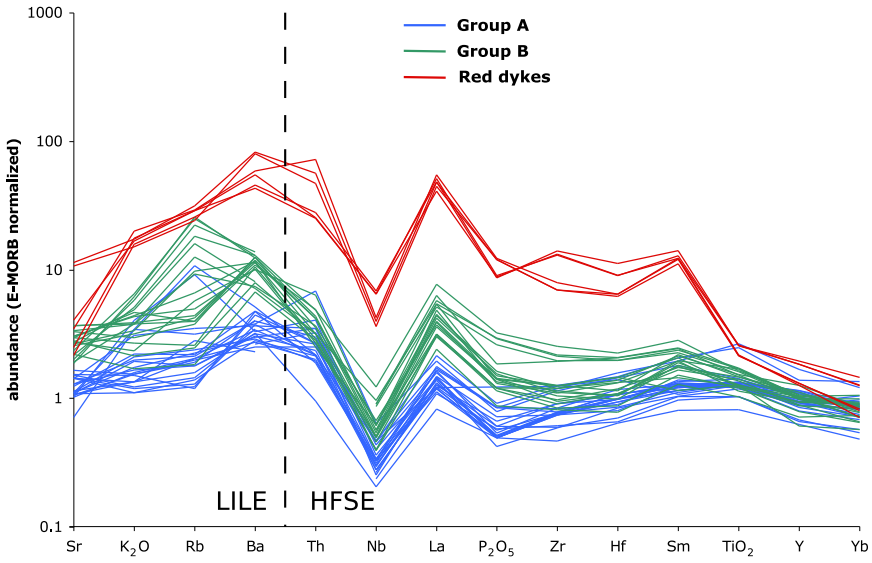

(a)

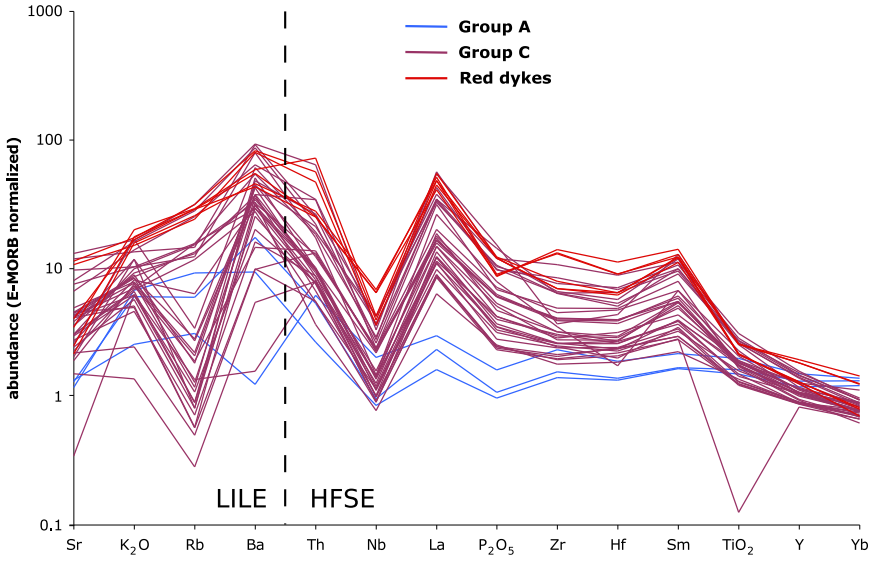

(b)

Figure 3.12: E-MORB normalized (Sun and McDonough, 1989) spidergrams (after Pearce, 1983) for (a) NT and (b) SK samples, grouped as per REE profiles.

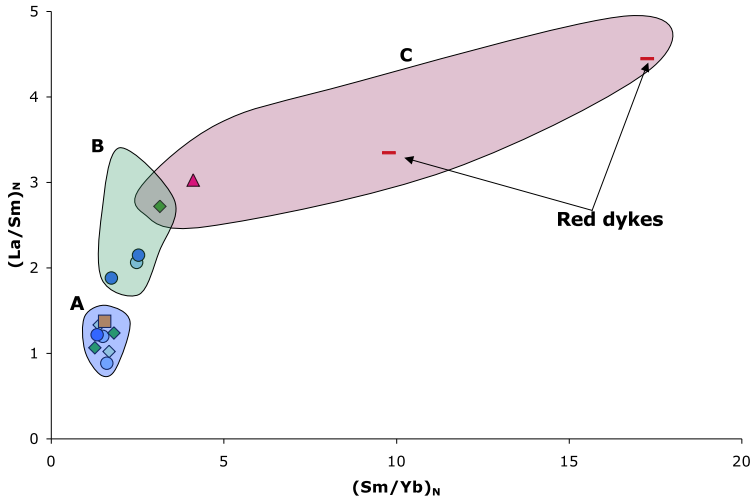

Figure 3.13: La/Sm vs. Sm/Yb (E-MORB normalized, Sun and McDonough, 1989) of samples selected for isotopic analyses. Symbols as in Figure 3.5; groups as in Section 3.3.4.

Table 3.2: Samples selected for Sm-Nd and Rb-Sr isotopic analyses in this study and the groups to which they belong.

Sample	Group
130A	A
129E	A
129F	A
129N	A
RD10-129-02	A
RD10-129-09	A
RD10-NEL-02	A
4701-0212a	A
130J	B
RD10-129-07	B
RD10-JER-04	B
RD10-LGL-04	B
4705-0202b	C
RD10-THK-03	red dyke
4703-0379b	red dyke

(2004) and Holmden *et al.* (1997) were used for the separation of Rb and Sr, whereas those of Böhm *et al.* (2007) and Unterschutz *et al.* (2002) were used for Sm and Nd separation. Isotopic analysis of Sm, Nd and Sr, by multi-collector ICP-MS, were as per Buzon *et al.* (2007) and Schmidberger *et al.* (2007). Rb isotopes were analyzed by Thermal Ionization Mass Spectrometry as per Creaser *et al.* (2004).

The Sm-Nd and Rb-Sr isotope data are presented in Tables 3.3 and 3.4, respectively. Errors for each measurement are reported as twice the Standard Error of up to 60 and 40 measurements for Nd and Sr isotopes, respectively. In the calculation of initial isotope ratios, 't' was set to 1830 Ma and 1818 Ma for the NT and SK samples, respectively. ϵNd is calculated with $(^{143}\mathrm{Nd}/^{144}\mathrm{Nd})_{\mathrm{CHUR}} = 0.512638$, $(^{147}\mathrm{Sm}/^{144}\mathrm{Nd})_{\mathrm{CHUR}} = 0.1967$ and $\lambda_{^{147}\mathrm{Sm}} = 6.54\times10^{-12}$ year^{-1}, using the equation:

$$\epsilon\mathrm{Nd} = \left(\frac{(^{143}\mathrm{Nd}/^{144}\mathrm{Nd})_{\mathrm{meas.}} - \left[(^{147}\mathrm{Sm}/^{144}\mathrm{Nd})_{\mathrm{meas.}} \cdot \left(e^{\lambda t} - 1\right)\right]}{(^{143}\mathrm{Nd}/^{144}\mathrm{Nd})_{\mathrm{CHUR}} - \left[(^{147}\mathrm{Sm}/^{144}\mathrm{Nd})_{\mathrm{CHUR}} \cdot (e^{\lambda t} - 1)\right]} - 1 \right) \cdot 10^4$$

$(^{87}\mathrm{Sr}/^{86}\mathrm{Sr})_{initial}$ has been calculated using $\lambda_{^{87}\mathrm{Rb}} = 1.42\times10^{-11}$ year^{-1}, using the equation:

$$\left(\frac{^{87}\mathrm{Sr}}{^{87}\mathrm{Sr}}\right)_{inital} = \left(\frac{^{87}\mathrm{Sr}}{^{87}\mathrm{Sr}}\right)_{\mathrm{meas.}} - \left(\frac{^{87}\mathrm{Rb}}{^{87}\mathrm{Sr}}\right)_{\mathrm{meas.}} \cdot \left(e^{\lambda t} - 1\right)$$

3.5.1 Sm-Nd results

In the ϵ-notation, samples with values of ϵNd = 0 have the same Nd-isotopic composition as the Chondritic Uniform Reservoir (CHUR; DePaolo and Wasserburg, 1976) at the time specified by t in the equation for calculating ϵNd, shown above. Positive ϵNd values are characteristic of rocks that have been derived from a mantle source with a long-term history of melt depletion (i.e., a depleted mantle, DM, source), similar to the mantle source that gives rise to mid-ocean ridge MORB magmas (Zindler and Hart, 1986). Negative ϵNd values are characteristic of rocks derived from a source with a long-term history of low Sm/Nd such as continental crust, or 'enriched' mantle.

From the Nd data, we see that the Group A and B samples show mildly to moderately negative ϵNd values. The samples from Group C indicates moderate to very negative ϵNd values and the red dykes show a consistent negative value of -4.5. This is summarized in Figure 3.14, where it is apparent that Groups A and B are indistinguishable, in terms of ϵNd. The Group C samples are distinctly more negative although there is minor overlap with the most evolved Group A and B samples. A depleted mantle model age (i.e. T_{DM}; DePaolo and Wasserburg, 1976) is calculated for all samples, however those with high ($^{147}Sm/^{144}Nd$) give model ages that are implausibly old. The samples for which T_{DM} was not implausibly old show model ages of 2.41 to 3.93 Ga.

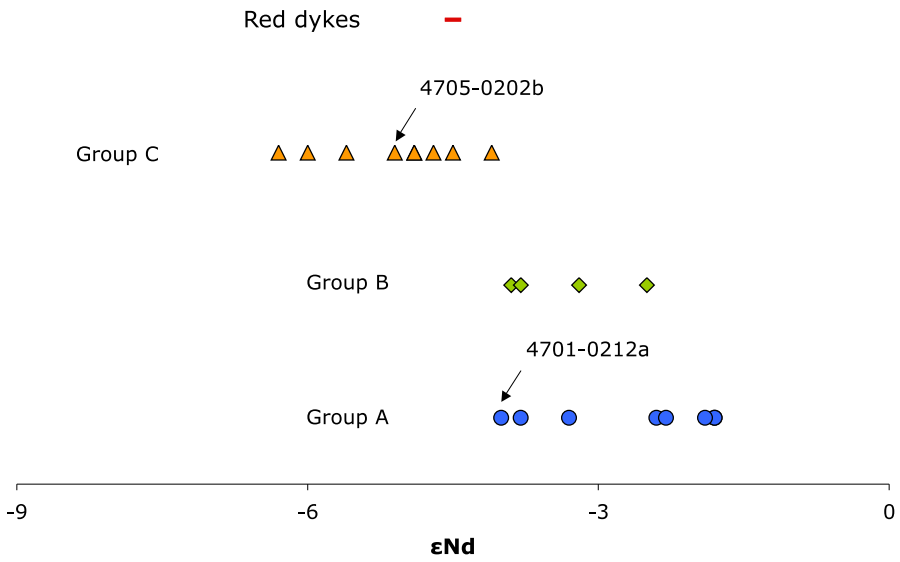

Figure 3.14: ϵNd of samples from Groups A, B, C and the red dykes. All Group C data, except 4705-0202b, from Morelli *et al.* (2009). Whereas Groups B is entirely contained within the range of Group A, Group C is considerably different and much more evolved. The two red dyke samples analyzed, one each from the NT and SK sample sets, show the same ϵNd value of -4.5.

Table 3.3: Results of Sm-Nd whole rock isotopic analyses.

Sample	Group	Sm (ppm)	Nd (ppm)	$^{147}Sm/^{144}Nd$	$^{143}Nd/^{144}Nd$	± 2 S.E. ($\times 10^{-06}$)	t (Ma)	ϵNd	T_{DM} (Ga)
130A	A	2.587	9.085	0.1722	0.512148	6.66	1830	-3.8	3.69
129E	A	2.933	9.854	0.1800	0.512338	6.84	1830	-1.9	3.70
129F	A	4.743	14.72	0.1949	0.512524	7.88	1830	-1.8	5.11*
129N	A	2.987	10.11	0.1787	0.512251	6.95	1830	-3.3	3.93
RD10-129-02	A	2.787	8.185	0.2059	0.512633	7.48	1830	-2.3	10.05*
RD10-129-09	A	2.512	8.862	0.1714	0.512236	7.54	1830	-1.9	3.31
RD10-NEL-02	A	2.930	10.18	0.1741	0.512245	1.09	1830	-2.4	3.50
4701-0212a	A	5.334	22.79	0.1415	0.511775	7.21	1818	-4.0	2.91
130J	B	5.292	25.92	0.1234	0.511594	5.66	1830	-3.2	2.64
RD10-129-07	B	4.642	22.68	0.1238	0.511633	7.91	1830	-2.5	2.58
RD10-JER-04	B	2.924	13.39	0.1320	0.511660	7.84	1830	-3.9	2.79
RD10-LGL-04	B	7.460	42.56	0.1060	0.511353	1.19	1830	-3.8	2.55
4705-0202b	C	8.061	52.57	0.0927	0.511133	5.51	1818	-5.1	2.54
RD10-THK-03	**	27.70	189.8	0.0883	0.511103	6.90	1830	-4.5	2.49
4703-0379b	**	34.13	286.3	0.0721	0.510916	6.26	1818	-4.5	2.41

* T_{DM} is implausibly old due to high $^{147}Sm/^{144}Nd$.

** red dykes.

3.5.2 Rb-Sr results

Given the mobility of Rb, a LILE, the Rb-Sr system is useful for source-tracing only if there has been little disturbance to the system after emplacement or very shorty thereafter. On a plot of the daughter isotope ^{87}Sr against

its parent ^{87}Rb (both expressed as ratios against ^{86}Sr, the stable and non-radiogenic isotope), such samples will fall on a straight line whose slope is proportional to the time elapsed since the closure of that system (i.e., when all the samples in that group had the same ^{87}Sr/^{86}Sr). Such plots, called isochrons, have been made for the Sr data in this study using Isoplot 3.00 (Ludwig, 2003), using a conservative estimate of 2% relative error in the measurement of the ^{87}Rb/^{86}Sr.

Figure 3.15(a) indicates that, with the exception of sample 4701-0212a, the samples generally fall on a straight line, indicating an age of 1824 ± 240 Ma. This age is refined to 1854 ± 120 Ma with the removal of the outlier, as in Figure 3.15(b). The coincidence of the isochron age (albeit with considerable error) with the U-Pb age of these samples (Bostock and van Breemen, 1992; Morelli *et al.*, 2009; Heaman, pers. comm.) indicates that the Rb-Sr system in these rocks has been either undisturbed, or disturbed very close to the time of emplacement. Separate isochrons for Groups A and B are shown in Figures 3.15(c) and 3.15(d) and show isochron ages of 1746 ± 180 Ma and 1848 ± 350 Ma, respectively. These, within error, are similar to the U-Pb ages. There is only one Rb-Sr datum for a Group C sample, so an isochron cannot be plotted.

That Group A sample 4701-0212a plots so far from the remaining samples in Figure 3.15(a) is an indication that it may not belong to the same igneous event as the remainder of the samples. An alternative explanation is that it is part of the same event but has experienced disturbance of its Rb-Sr system after emplacement. It must be remembered that this sample and two others, 4701-0210a and 4701-224, are included in Group A on the basis of their flat

REE profiles, as observed in Figure 3.10(b). These three samples are the only Group A representatives in the SK set and, as seen in Figure 3.4, these three samples are found ∼20 kilometres SW of Uranium City, with no other samples in close proximity. In light of the off-trend position on the Sr isochron, their geographic isolation from the other Group A samples makes it unlikely that they are part of the same event. Geochemically, they show similar REE and spidergram profiles as the Group A samples, as seen in Figures 3.10(b) and 3.12(b). Petrographically, 4701-0210a is only notably different by the alteration of its palgioclase to a fine-grained, pinkish-brown, highly birefringent mineral. Thus, while it is recognized that the data presented do not unequivocally demonstrate that these three samples are not part of the igneous event(s) considered in this work, they will not be discussed further.

The CIF whole-rock Rb-Sr data (Cousens *et al.*, 2001) indicate an isochron age of 1609 ± 230 Ma, which is refined considerably by removing the five outliers circled in Figure 3.16(a), to 1764 ± 51 Ma as seen in Figure 3.16(b). This age is similar, within error, to the age of the CIF, indicating little disturbance of the Sr system in these rocks.

The y-intercept of the line of best fit on an Rb-Sr isochron is considered to be the $^{87}Sr/^{86}Sr$ ratio at the time of emplacement. These values have been plotted for Groups A, B, C and the red dykes on Figure 3.17. Values of initial $^{87}Sr/^{86}Sr$ for Groups A and B on this figure (with error-bars equal to 2σ) were determined from the y-intercepts of the isochrons in Figures 3.15(c) and 3.15(d). As an isochron cannot be plotted for less than 4 samples (Ludwig, 2003), the initial value for Group C and the red dykes was calculated directly using the decay equation (above), and the assumed ages for the samples, as

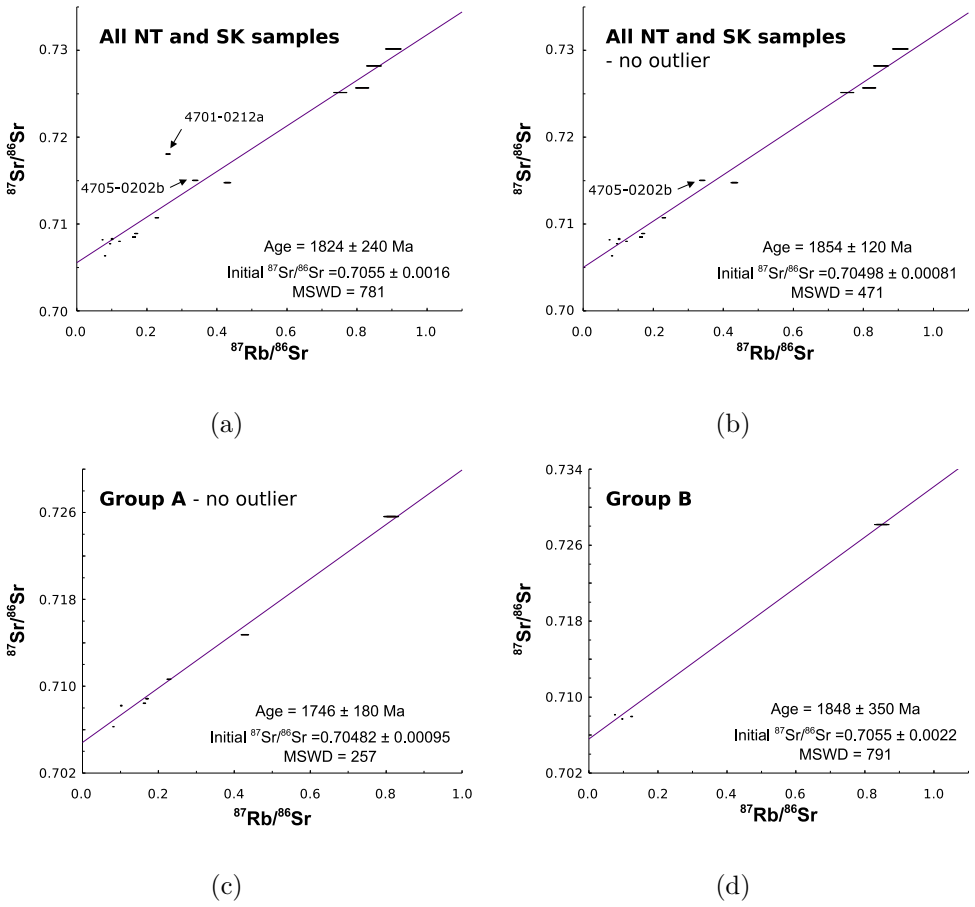

Figure 3.15: Rb-Sr isochrons for (a) all samples analyzed in this study, (b) all samples except 4701-0212a, (c) Group A samples only and (d) Group B samples only. Sample 4705-0202b is the only sample from Group C for which there is Sr isotope information. The close correspondence of all samples (except outlier 4701-0212a) to the lines of best fit, the approximately similar ages (from the the slope of the line) and the small errors on the initial $^{87}Sr/^{86}Sr$ provide confidence that the Rb-Sr system in these rocks has not been reset or altered considerably after emplacement and thus records primary information that can be utilized for source-tracing. The errors are reduced considerably by removal of the outlier from the dataset. Isochrons have been plotted using Isoplot version 3.00 (Ludwig, 2003).

indicated in Table 3.4. Despite the overlap of error bars, it is observed that there is a progression from lower to higher initial $^{87}Sr/^{86}Sr$ from Groups A through C. The initial $^{87}Sr/^{86}Sr$ for the CIF (without outliers) is 0.70497 $\pm$ 0.00081. The initial $^{87}Sr/^{86}Sr$ values for all suites are plotted in Figure 3.17 for quick comparison.

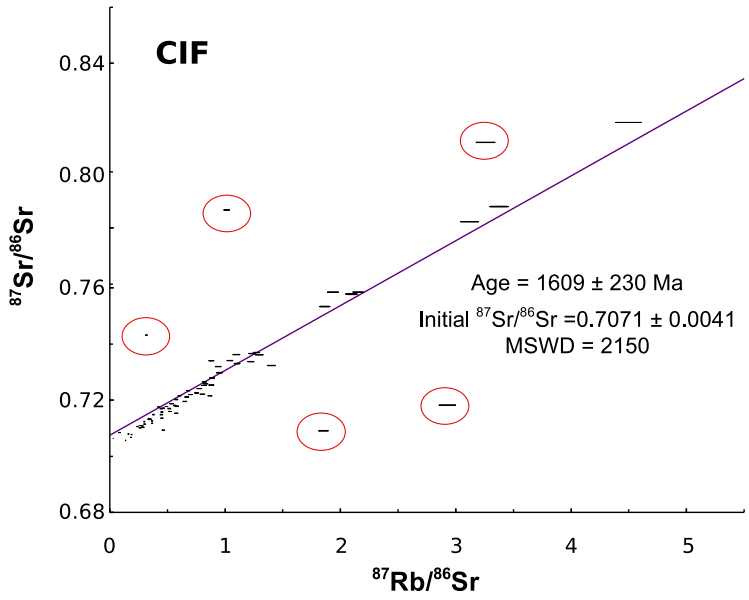

(a)

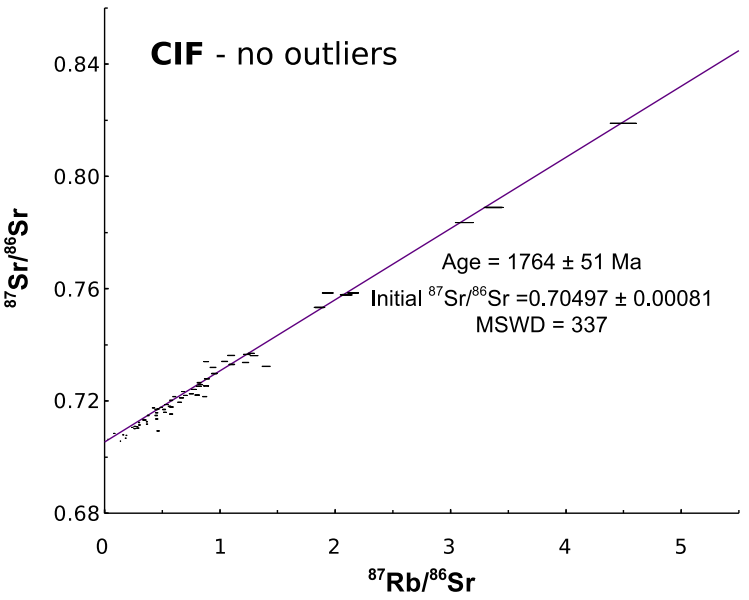

(b)

Figure 3.16: Rb-Sr isochrons for the CIF, (a) for all data from Cousens *et al.* (2001); (b) for all data without outliers circled in (a). Isochron plotted using Isoplot version 3.00 (Ludwig, 2003).

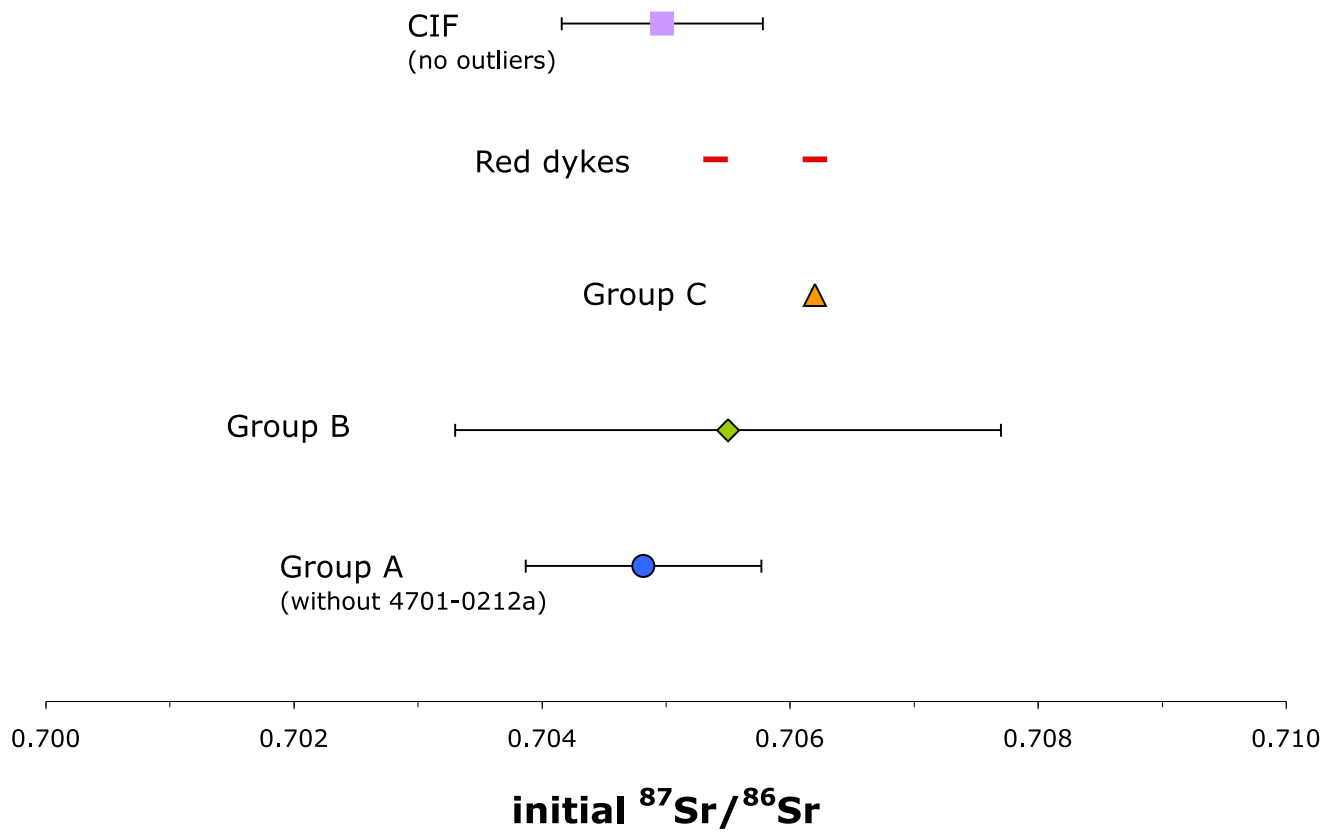

Figure 3.17: Initial $^{87}Sr/^{86}Sr$ for Groups A, B, C, the red dykes and the CIF. Initial values and error-bars (2σ) for Groups A and B are from the isochrons in Figures 3.15(c) and 3.15(d), respectively, whereas values for Group C and the red dykes are as calculated in Table 3.4.

Table 3.4: Results of Rb-Sr whole rock isotopic analyses

Sample	Group	Rb (ppm)	Sr (ppm)	$^{87}Rb/^{86}Sr$	$^{87}Sr/^{86}Sr$	± 2 S.E. ($\times 10^{-05}$)	t (Ma)	$(^{87}Sr/^{86}Sr)_{initial}$
130A	A	40.71	145.0	0.8141	0.72560	3.5	1830	0.70417
129E	A	5.237	187.6	0.0808	0.70643	1.9	1830	0.70431
129F	A	9.384	166.9	0.1628	0.70859	2.8	1830	0.70431
129N	A	30.53	206.4	0.4283	0.71483	3.5	1830	0.70355
RD10-129-02	A	8.605	146.9	0.1695	0.70899	2.4	1830	0.70452
RD10-129-09	A	8.357	239.9	0.1008	0.70837	4.7	1830	0.70571
RD10-NEL-02	A	16.10	204.2	0.2282	0.71074	2.2	1830	0.70474
4710-0212A	A	17.21	192.8	0.2586	0.71806	3.5	1818	0.71130
130J	B	16.49	393.1	0.1214	0.70811	2.9	1830	0.70491
RD10-129-07	B	16.85	515.0	0.0947	0.70785	2.4	1830	0.70536
RD10-JER-04	B	7.897	313.1	0.0730	0.70829	2.0	1830	0.70637
RD10-LGL-04	B	92.33	315.8	0.8478	0.72813	3.0	1830	0.70581
4705-0202B	C	54.40	467.2	0.3372	0.71507	2.2	1818	0.70625
RD10-THK-03	**	121.7	390.7	0.9037	0.73003	2.2	1830	0.70624
4703-0379B	**	135.0	520.8	0.7515	0.72510	2.0	1818	0.70545

** red dykes.

Chapter 4

Discussion

The results described in the previous chapter indicate that the NT samples, emplaced at *ca.* 1830 Ma (Bostock and van Breemen, 1992, Heaman, pers. comm.), fall into two distinct groups. As seen in Figure 3.10(a), Group A[1] is very similar to E-MORB in its pattern of REE enrichment, whereas Group B[2] has generally similar HREE abundance as E-MORB, but with higher LREE and MREE abundance. However, Figures 3.14 and 3.17 indicate that these groups are indistinguishable on the basis of ϵNd and initial $^{87}Sr/^{86}Sr$, respectively. As the intrusion of Group A material into Group B material shows no chill margin (Figure 3.3), it is likely that Group A was emplaced a very short time after Group B.

At approximately the same time (i.e., 1818 $\pm$ 4 Ma; Morelli *et al.*, 2009), the SK samples were emplaced $\sim$200 kilometres to the southeast. As observed in Figure 3.10(b), the majority of SK samples are much more LREE enriched than Group B, thus falling into their own group, C[3]. This group has more

[1]Group A samples: 129A, C, E, F, G, K, L, N; 130A; RD10-129-01, -01A, -02, -03, -04, -05, -06, -09, -10; RD10-130-04; RD10-LGL-05A; RD10-NEL-01 and -02.

[2]Group B samples: 004A; 129B, D; 130J; RD10-129-07, -08; RD10-130-01; RD10-JER-02, -03, -04; RD10-LGL-01, -01A, -02, -03, -04, -05, -05B, -06 and -06A.

[3]Group C samples: All SK samples, except 4701-0210a, -0212a and -224.

negative ϵNd than Groups A and B (Figure 3.14), but initial $^{87}Sr/^{86}Sr$ of these suites is similar within error, as seen in Figure 3.17.

Due to the spatial and temporal proximity of these three groups, this chapter aims to reconcile the chemical compositions into a geologically plausible petrogenetic and tectonic model. A second objective of this chapter is to place these mafic samples in a broader regional context by comparing them to the Christopher Island Formation (using data from Cousens *et al.*, 2001) and the models that have been proposed for the genesis of those rocks. Finally, to place the geochemistry of the samples in the present study in context with that of other, well-studied dykes, the data will be presented along with that for the mafic rocks of the Molson Igneous Event (Heaman *et al.*, 2009). The comparisons between these studies will be made at the end of this chapter.

4.1 Crustal contamination

At Tsu Lake, several dykes display trains of centimetre-scale to decimetre-scale wallrock xenoliths within the main-body of the dyke (Figure 3.2). In some dykes, the xenoliths appear to have been broken up (e.g., Figure 3.2e), but it is unclear if this is due to physical or chemical degradation. The latter would chemically contaminate the dyke and obscure the primary source information. Thus, crustal contamination must be assessed as a potential cause of the observed geochemical variation.

Mafic magmas have high iron and magnesium and low silica, so contamination with a felsic crustal rock, such as a granite, would decrease the iron and magnesium content and increase the silica content of the resulting rock. The Th/Nb ratio can be also used as an index of crustal contamination (Bougault

et al., 1980), in conjunction with the Th abundance (to rule out high Th/Nb ratios as a result of low Nb content). Contamination with granitic material would result in a higher Th/Nb ratio in the resulting rock.

As described in Chapter 2, the NT dykes intrude the TMZ granites and basement gneisses, which display ϵNd values of -5 to -15 (De *et al.*, 2000). Assimilation of these lithologies by a juvenile magma from a depleted mantle source ($\epsilon Nd_{1830\ Ma} \simeq +5$; McCulloch and Wasserburg, 1978) would drive the resulting rock to lower ϵNd values, whereas ferromagnesian and silica contents would decrease and increase, respectively. The link between ϵNd and magnesium content through contamination was demonstrated by Peate and Hawkesworth (1996) for the Gramado member of the Paraná continental flood basalt. In a contamination scenario, Th abundance and the Th/Nb ratio is expected to increase as ϵNd approaches lower values. The expected relationship for crustal contamination between these indices are indicated by arrows in Figure 4.1.

It is observed in Figure 4.1 that, for Group A, there is some correlation between ϵNd and the selected contamination indices. However, the generally low R^2 values for the lines regressed through these data indicates that the correlation is weak, although Group A shows a good correlation in Figure 4.1(c). In that figure, the spread in Th/Nb is due to a decrease in Nb content (as opposed to and increase in Th), as observed by the low Th concentrations of these samples in Figure 4.1(d), implying that this is not due to crustal contamination, as discussed above. Group B and C samples also show consistently weak correlation between contamination indices. The only exception is that, in Figure 4.1(b), Group B samples show strong negative correlation

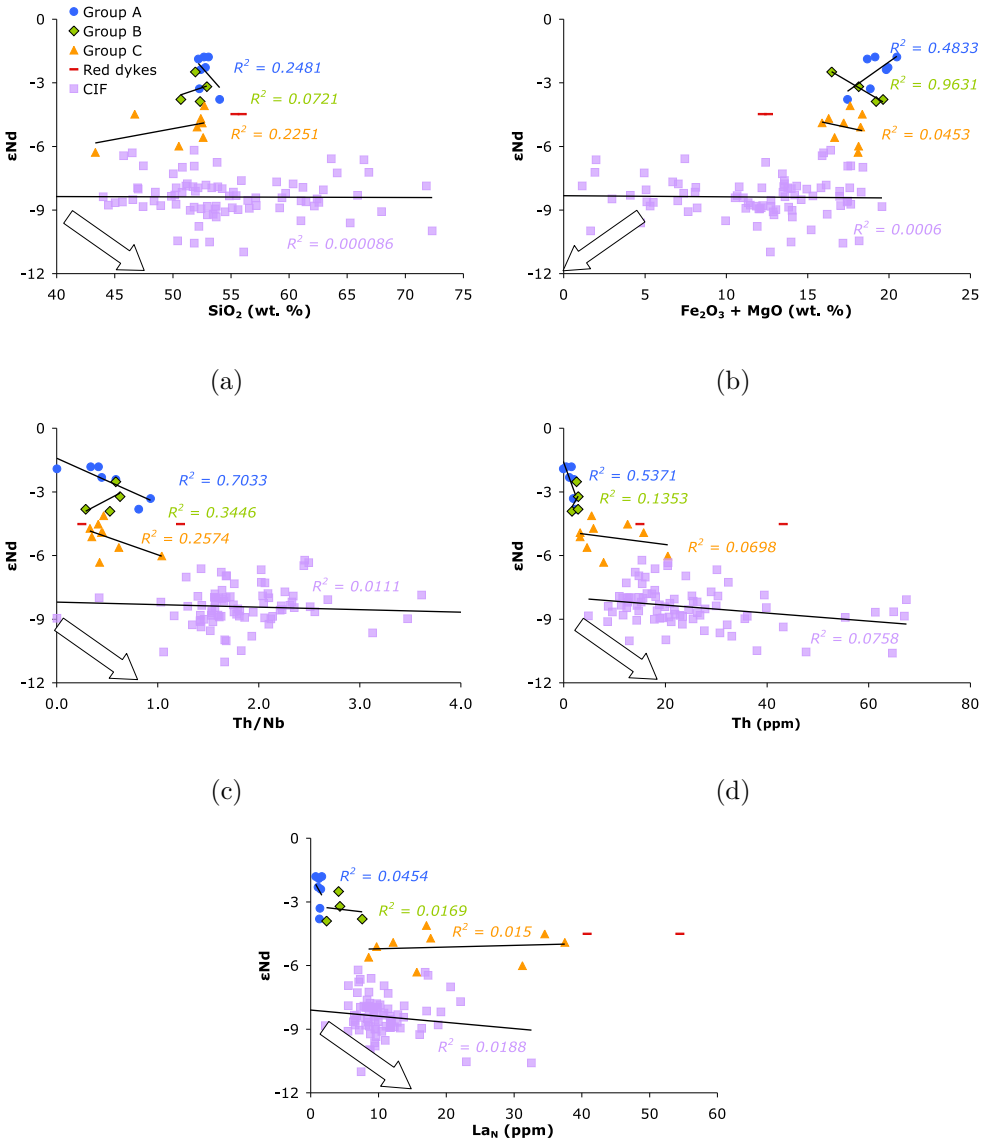

Figure 4.1: ϵNd plotted against various crustal contamination indices for Groups A, B, C, the red dykes and the CIF as described in the text. Arrows indicate expected trend with increasing contamination and lines within groups are the observed trends with calculated R^2 values indicating goodness of fit. Lack of significant correlation indicates that these rocks were not contaminated with upper crustal material. CIF data from Cousens *et al.* (2001).

between ϵNd and ferromagnesian content, contrary to what is expected from crustal contamination. This group also shows a positive trend (albeit with poor correlation) in Figure 4.1(c), also contrary to what is expected.

Also, as the upper crust is enriched in the REE, whereas Depleted Mantle is not (McKenzie and O'Nions, 1991), if the groups were related by crustal contamination, one would expect a progressive steepening of the slope of the REE profile as the degree of contamination increased. Flat and steep profiles are observed in Figure 3.10(a) for Groups A and B, respectively, however, there are no samples with intermediate slope. This point is emphasized by the gap between the Group A and B clusters in Figure 3.9, especially on the y-axis (i.e., $(La/Sm)_N$, the slope in the REE profile from LREE to MREE). Groups B and C show progressively steeper REE slope (Figure 3.9), as expected with increasing contamination. However these groups do not show a corresponding shift in the other contamination indices, as seen in Figure 4.1. Thus, it is argued that the samples of Groups A and B have experienced little to no crustal contamination.

Group C samples are exclusively from SK and include those discussed in Morelli *et al.* (2009). Those authors came to the conclusion that the samples experienced little to no crustal contamination, based on the lack of expected correlation between ϵNd and SiO_2. That there is little correlation evident between ϵNd and other contamination indices shown in Figure 4.1 reinforces those authors' conclusion. The red dykes also do not show any correlation between crustal contamination indices, implying that these samples are also not contaminated by crustal material. It must be noted, however, that only two samples of the red dykes were analyzed.

Also plotted on Figure 4.1 are the data for the CIF (Cousens *et al.*, 2001). Based on a plot of ϵNd vs. SiO_2, similar to Figure 4.1(a), Cousens *et al.* (2001, 2004) asserted that the CIF rocks have not experienced significant crustal contamination. That conclusion is well supported, given that the CIF shows little to no correlation between the other contamination indices presented in Figure 4.1.

4.2 Source characteristics

Having established that the samples discussed in this study have experienced little to no crustal contamination, it is possible to use their geochemistry to make some inferences about the nature of their mantle source. This will be discussed in relation to the CIF, which is also considered to represent uncontaminated magmas, as per Cousens *et al.* (2004) and as shown above.

The REE profiles and spidergrams of the red dykes from the NT and SK sample sets plot entirely within the field of the CIF in Figure 4.2. Cousens *et al.* (2004) describe an "orange to red-weathering, potassium feldspar-bearing felsite" overlying the basement of the CIF. The red dykes from this study have been confirmed by Cousens (pers. comm.) to be similar to these felsites, which have also been called 'bostonites' (Peterson *et al.*, 2010). Thus, on the basis of the unique petrography of these rocks and the occurrence of similar ones in the typical CIF localities (Cousens *et al.*, 2004; Peterson *et al.*, 2010, 2011), the red dykes will henceforth be grouped with the CIF rocks.

As seen in Figure 4.2(a), Groups A and B are distinct from the CIF in their degree of overall enrichment and in the slope of the REE profile. The REE profiles for Group C, on the other hand, are entirely within the field of the CIF

and the slopes appear to be similar, though there is less variation in the HREE abundance. This separation of groups is less apparent in the spidergrams in Figure 4.2(b), where the CIF field encloses Groups A, B and C in the HFSE (with the exception of Th, Nb and La which are considerably lower in Group A than the CIF). As with the REE profiles, the Group C spidergrams are most similar to the CIF in the shape and slope of the HFSE portion of the spidergram, whereas Groups A and B are considerably flatter. All samples show a steep negative Nb anomaly. This anomaly is also commonly observed in arc volcanism (e.g., Ryerson and Watson, 1987), where it is associated with modification of the mantle overlying a slab of subducting oceanic crust (Pearce, 1982; McCulloch and Gamble, 1991).

The LILE enrichment of all suites in Figure 4.2(b) is likely due to the mobility of these elements in aqueous fluids (Muecke *et al.*, 1979; Brewer and Atkins, 1989) and could indicate metasomatic alteration of the source. This hypothesis is compatible with a subduction-modified source (implied by the negative Nb anomaly), as it is thought that a subducting slab of oceanic crust dehydrates at depth, releasing fluids into the overlying mantle wedge (Pearce, 1982; McCulloch and Gamble, 1991).

On a Th-Hf-Nb tectonic discrimination diagram (Figure 4.3, after Wood, 1980), Groups A, B and C plot in the 'arc-basalt' field. The source of arc volcanics is thought to be in a mantle modified by the subduction of oceanic crust and the subsequently metasomatized by fluids driven from that crust (Gill, 1981). However, between 1850 and 1800 Ma, arc volcanism related to the THO was restricted to the S-SE margin of the Hearne Domain (Corrigan *et al.*, 2009) and there is no evidence for plutonic or volcanic arc magmatism

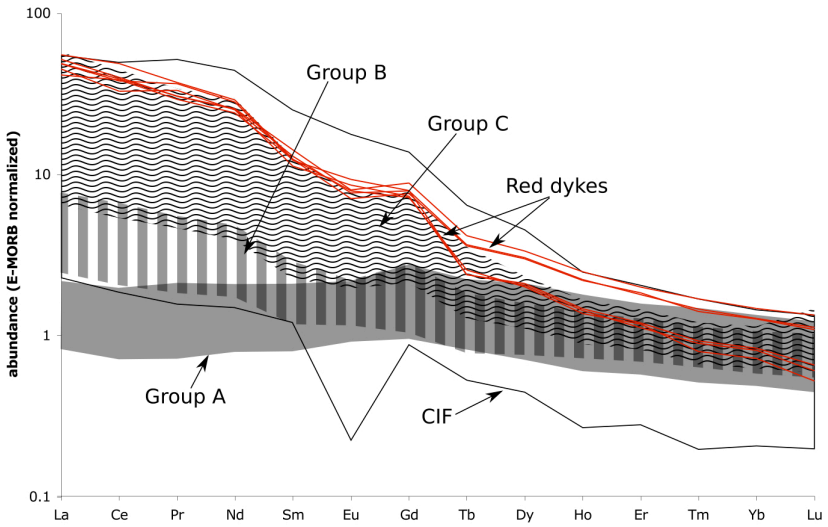

(a)

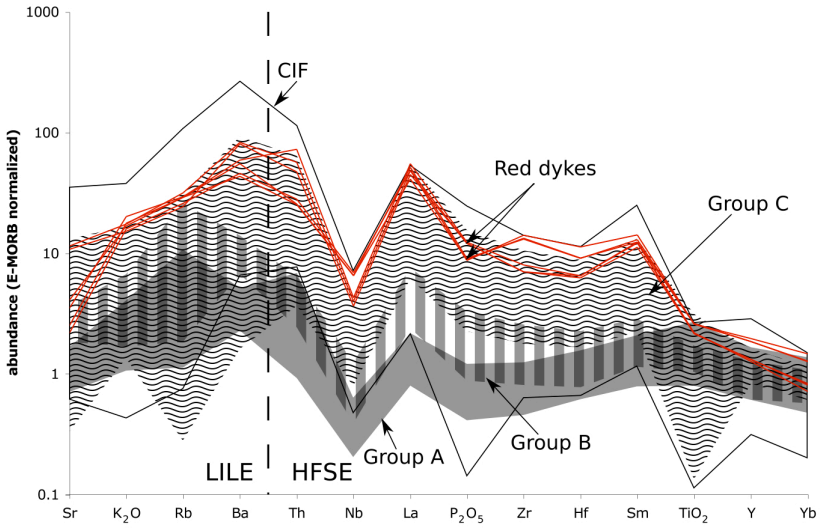

(b)

Figure 4.2: E-MORB normalized (Sun and McDonough, 1989) incompatible element profiles for Groups A, B, C and the CIF. (a) REE profiles and (b) spidergrams.

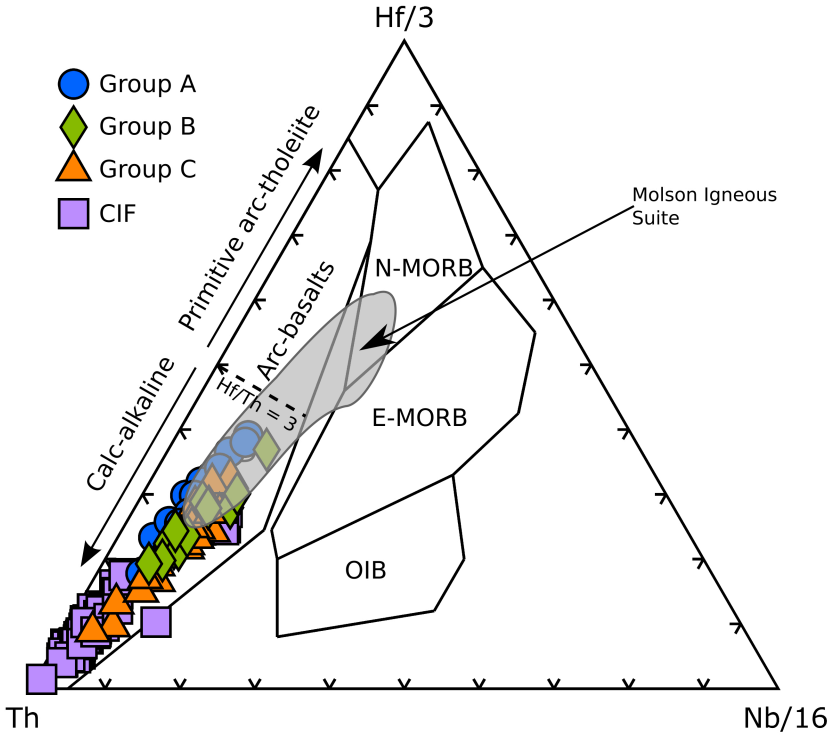

Figure 4.3: Th-Hf-Nb tectonic discrimination diagram, after Wood (1980), showing the samples of the present study plotting in the field of arc volcanics. This supports the interpretation of Cousens *et al.* (2001) that the CIF were sourced from a subduction-modified, metasomatized mantle. The similarity of the Group C samples with the CIF suggests that they share a similar source. Data for the CIF and Molson Igneous Suite from Cousens *et al.* (2001) and Heaman *et al.* (2009), respectively.

in the field area of the present study. This leaves open the possibility that the mantle was modified by subduction prior to the onset of the THO, as conceived by Cousens *et al.* (2001).

The CIF samples also plot in this field, supporting the interpretation of Cousens *et al.* (2001, 2004) that they are sourced from a subduction-modified mantle. Groups A, B and C also plot in this field making it likely that they too were sourced from a subduction-modified mantle. Despite overlap in the LILE abundances in Figure 4.2(b), it is observed that Groups A and B show

generally lower range of abundances than Group C and the CIF. This could indicate that the degree of metasomatism that affected the source of Groups A and B was less than for Group C and the CIF.

4.2.1 Metasomatism

However, metasomatism by an aqueous fluid alone cannot explain the very elevated HFSE abundances of Group C and the CIF observed in Figure 4.2, as these elements are relatively immobile in such fluids (e.g., Muecke *et al.*, 1979; Brewer and Atkins, 1989). Cousens *et al.* (2004) indicate that the high carbonate content of the CIF requires their mantle source to have been metasomatized by silicate, or H_2O–CO_2 rich fluids, or both. Such a fluid could produce the observed enrichments in the CIF as it might conceivably have a higher carrying capacity for the HFSE. Such a fluid could also have produced the incompatible element enrichment observed in Group C although, since no carbonate minerals are evident in the studied thin-sections of Group C, the metasomatizing fluid must have been relatively CO_2 poor.

As Nd is marginally more incompatible than Sm (e.g., Arth, 1976), thus preferentially enriched in a metasomatizing fluid, such a process would also decrease the ϵNd value of the source. The CIF show very negative values in Figure 4.4, supporting the argument of extensive metasomatism of their source. Group C show less negative ϵNd values than the majority of the CIF, which may indicate a slightly lower degree of metasomatic effect. Groups A and B have the least negative ϵNd values of the four suites. This supports the hypothesis that their source experienced a lowest degree of metasomatic enrichment compared to the Group C and CIF sources, as argued above on

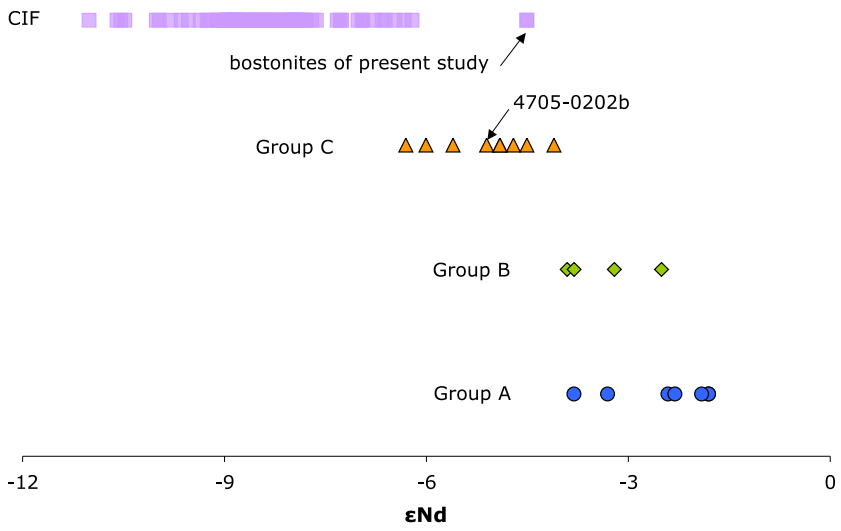

Figure 4.4: ϵNd of samples from Groups A, B, C and the CIF. All CIF data, except for the bostonites of this study (i.e., the red dykes), from Cousens *et al.* (2001). All Group C data, except 4705-0202b, from Morelli *et al.* (2009). The negative values of the CIF and Group C samples may be due to metasomatic alteration of their source. The less negative values for Groups A and B support the interpretation that these rocks are from a source that has experienced less metasomatism, as discussed in the text.

the basis of LILE enrichment.

This metasomatism may be further examined with a plot of ϵNd vs. initial $^{87}Sr/^{86}Sr$, as in Figure 4.5. It is observed that ϵNd varies considerably between the suites whereas initial $^{87}Sr/^{86}Sr$ is similar, within error. Metasomatism by an aqueous fluid alone would increase the initial $^{87}Sr/^{86}Sr$ by enriching it in ^{87}Rb, but would have minimal effect on ϵNd, since Rb is mobile whereas the REE are immobile in aqueous fluids (e.g., Muecke *et al.*, 1979; Brewer and Atkins, 1989). Thus, progressive metasomatism would produce a sub-horizontal trend, as indicated on Figure 4.5 and as observed between Groups A, B and C on that plot. It must be remembered, however, that the error of the initial $^{87}Sr/^{86}Sr$ is high. Therefore, this 'trend' may simply be a reflection

of the variability of the composition of these samples.

On the other hand, metasomatism by a fluid of carbonatitic composition would produce very negative ϵNd values, as carbonatites generally have low ϵNd (e.g., Nelson *et al.*, 1988). Crucially, the high $^{87}Sr/^{86}Sr$ ratio that such a fluid would impart to the source would not increase substantially with time due to the low Rb content in carbonatites (e.g., Nelson *et al.*, 1988). This would result in a sub-vertical trend on Figure 4.5 with increasing metasomatism, which is evident when the four suites are plotted on expanded axes, as in the inset in Figure 4.5. Such a fluid composition (i.e., high CO_2 and incompatible element concentration; e.g., Nelson *et al.*, 1988) is also favourable since the high carbonate content of the CIF rocks requires a mantle source rich in CO_2 (Cousens *et al.*, 2004).

The arguments presented above indicate that it is possible to attribute the isotopic variation of these rocks to varying degrees of source metasomatism by fluids of different composition. However, regardless of the nature of the metasomatic fluid (or fluids), that Groups A and B plot closer to the DM indicates that they are less metasomatized than Group C and the CIF, which plot farther away.

4.2.2 Water-content

An additional observation to be made from the Th-Nb-Hf diagram (Figure 4.3) is that Groups A, B, C and the CIF samples are spread out in the 'calc-alkaline' arc-basalt subfield. Despite extensive overlap, the samples closest to the dividing line of this field with the 'primitive arc-tholeiite' are from Groups A and B, whereas Group C plots closer to the Th apex. The CIF

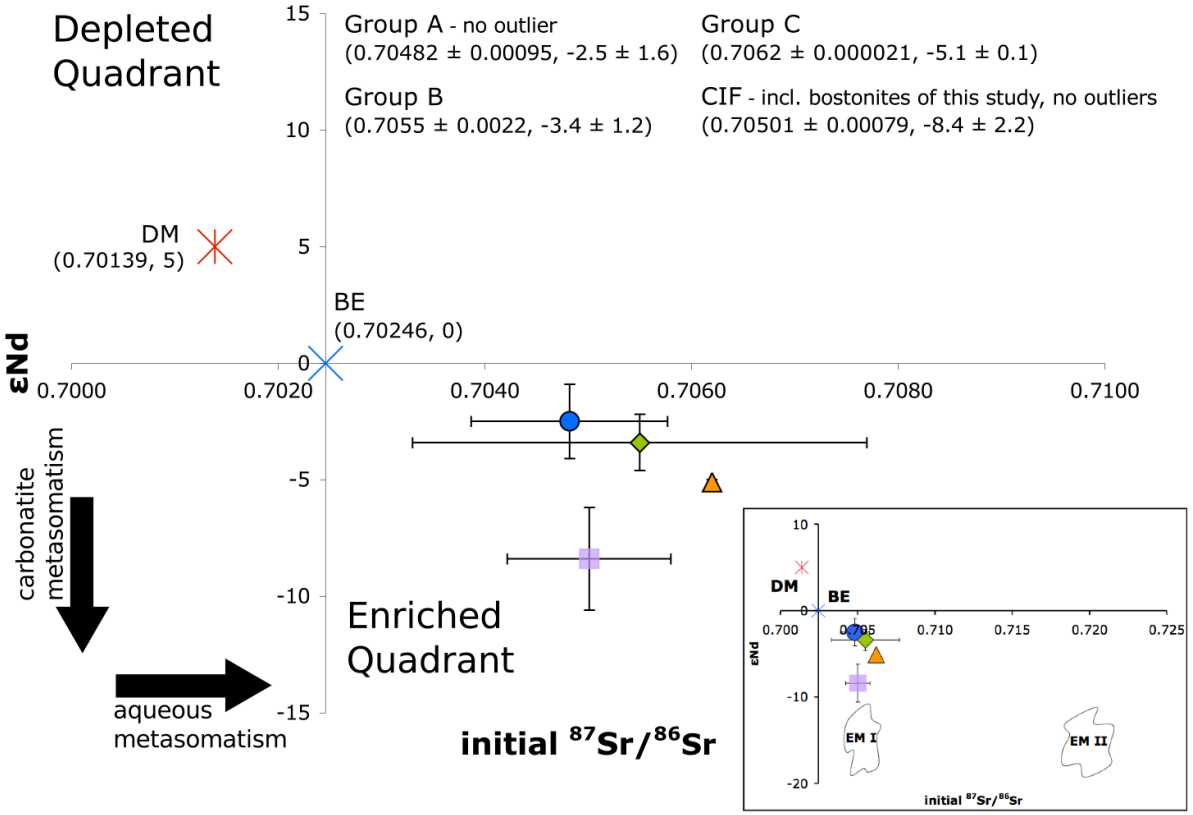

Figure 4.5: ϵNd vs. initial $^{87}Sr/^{86}Sr$ for Groups A, B and the CIF (t =1830 Ma) and Group C (t = 1818 Ma; Morelli *et al.*, 2009). Initial $^{87}Sr/^{86}Sr$ values are from the Sr-isochrons in Figure 3.17, except Group C, which was calculated from an individual analysis as described in the text. Error bars are 2σ. Arrows point in the direction of increasing metasomatic effect, as discussed in the text. This plot shows the strong separation of Groups A, B, C and the CIF from each other in ϵNd but not initial $^{87}Sr/^{86}Sr$. Depleted Mantle (DM) and Bulk Earth (BE) data from McCulloch and Wasserburg (1978) and Taylor and McLennan (1985); Enriched Mantle (EM I and EM II) from Zindler and Hart (1986); CIF data from Cousens *et al.* (2001).

plots farthest from the calc-alkaline/tholeiite dividing line and closest to the Th apex.

This calc-alkaline/tholeiite difference between the groups is most clearly shown on Figure 4.6(a), an AFM diagram after Irvine and Baragar (1971). The CIF suite clearly describes a calc-alkaline trend and Groups A and B are in the tholeiitic field. According to Sisson and Grove (1993), tholeiites crystallize under low-H_2O conditions, whereas high-H_2O content favours early magnetite crystallization, in turn producing the calc-alkaline trend.

This suggests that the source of the CIF had relatively higher H_2O-content compared to the Group A and B source, an assertion that is bolstered by the dominantly minette and lamproite lithology of the CIF (Cousens *et al.*, 2004). These are rock types that contain primary biotite (Le Maitre, 2002), whereas the Group A and B samples do not contain any such primary hydrous phases (Appendix B). This fits well with the above argument that the CIF source was metasomatized to a greater extent than the Group A and B source.

Group C samples plot close to the tholeiite/calc-alkaline division in Figure 4.6(a). Sisson and Grove (1993) demonstrated that the calc-alkaline differentiation trend shown by subduction-related volcanics is due to fractionation of minerals like spinel and magnetite from an H_2O-rich magma. As these phases can incorporate TiO_2, their early fractionation would reduce the amount of titanium available for phases that crystallize from the magma later, resulting in a rock with a lower TiO_2 content.

Thus, the relatively high TiO_2 content of the Group C samples seen in Figure 4.6(b), indicates that Ti-bearing phases did not fractionate out early. This implies that the source was not as H_2O-rich as the CIF, which show

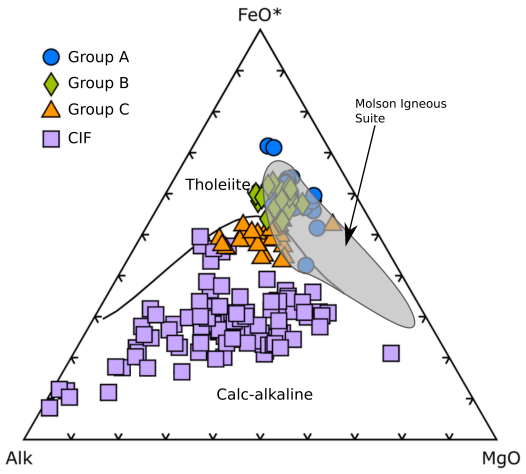

(a)

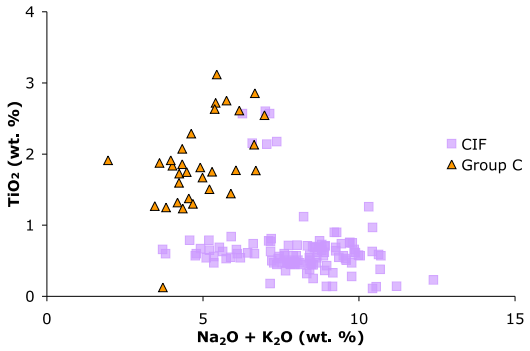

(b)

Figure 4.6: (a) An AFM diagram (Irvine and Baragar, 1971) showing the tholeiitic trend of Groups A and B, and the calc-alkaline trend of Group C and the CIF. The latter are interpreted in the present study to be due to higher water-content in the CIF source than in the Group C source, as per Sisson and Grove (1993); (b): TiO_2 vs. total alkaline content for the CIF and Group C rocks, indicating that the latter are more enriched in TiO_2 for a given alkaline content, which may be linked to the degree of spinel and/or magnetite fractionation in the source (Sisson and Grove, 1993). This is indicates that the water content of the source for the CIF was greater than that for the Group C source. Data for the CIF and Molson Igneous Suite from Cousens *et al.* (2001) and Heaman *et al.* (2009), respectively.

considerably less TiO_2 than Group C. The assertion of lower water content in the Group C magmas is supported by the observation that samples from Group C do not contain primary hydrous phases (Appendix B), whereas the CIF rocks do (Cousens *et al.*, 2004). This also fits with the argument above that Group C rocks are from a source that has been more metasomatized than the source of Groups A and B, but less so than the CIF source.

4.2.3 Depth of melting

The depth of the sources can be semi-quantitatively assessed by examining the REE profiles of the groups, as shown in Figure 4.2(a). As garnet is a phase that retains HREE preferentially (Irving and Frey, 1978), the steep HREE profile of Group C and the CIF can be interpreted as indicating that garnet remained in the source region upon melting. This implies that the source for the CIF and Group C rocks must be at or below ∼75 kilometres, where garnet is stable (McKenzie and O'Nions, 1991). Conversely, the shallow to flat HREE profiles of Groups A and B is evidence that garnet is not present in the source, placing its depth above 75 kilometres.

These conclusions are supported by Figure 4.7, a plot of the slopes of the REE profiles, as per Lassiter and DePaolo (1997). Here, the sub-horizontal trend of Group C and the CIF indicates melting in the presence of garnet, whereas the sub-vertical trend of Groups A and B indicates spinel in the source region. As spinel is a polymorph of garnet that is stable at lower pressures than garnet (McKenzie and O'Nions, 1991), this supports the above assertion that the source for Groups A and B was shallower than that for Group C and the CIF.

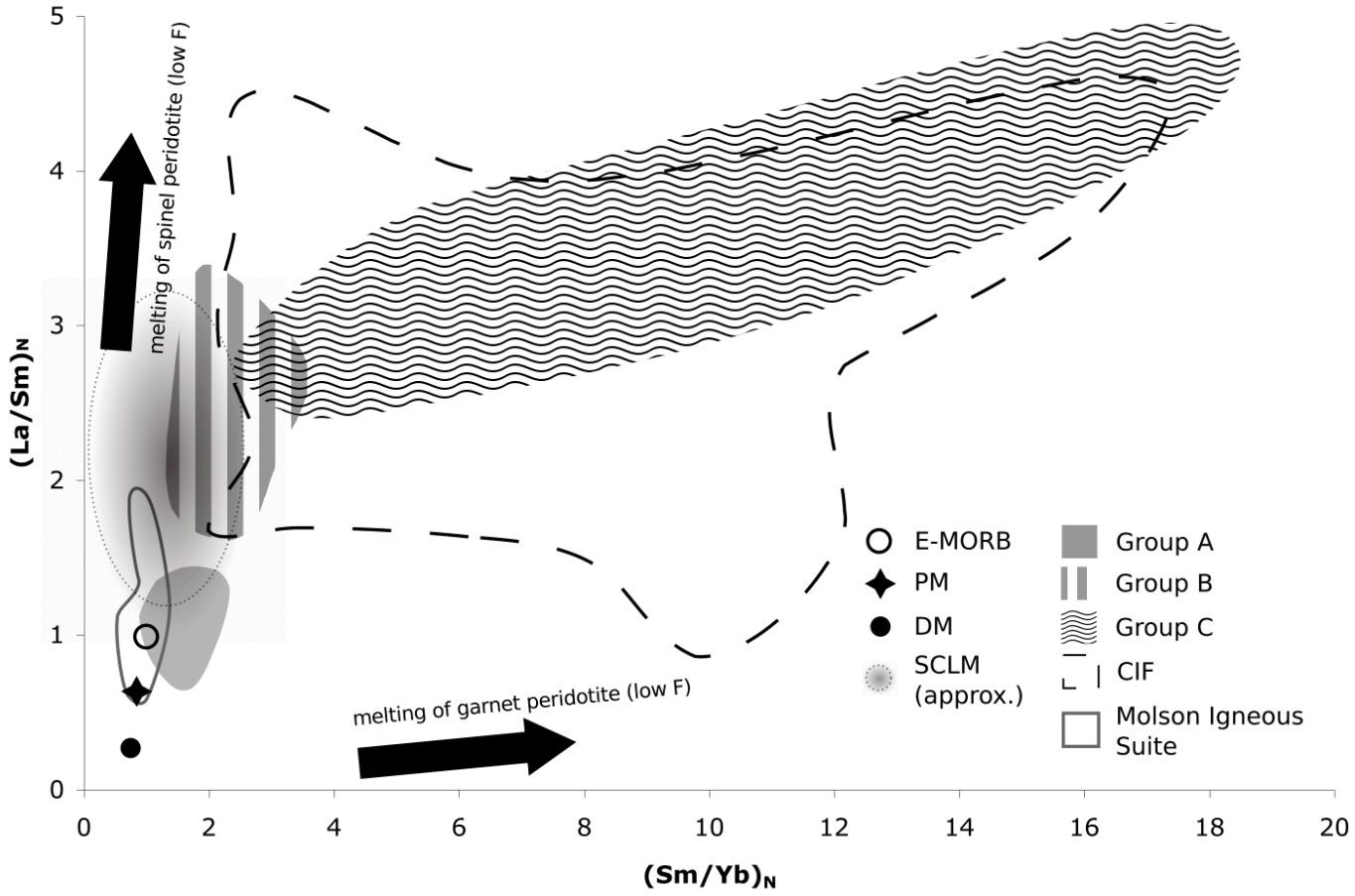

Figure 4.7: La/Sm vs. Sm/Yb plot (E-MORB normalized; Sun and McDonough, 1989). Arrows are in the direction of decreasing melt fraction, as per Lassiter and DePaolo (1997); Primitive Mantle (PM) and Depleted Mantle (DM) values after McKenzie and O'Nions (1991); approximate Sub-Continental Lithospheric Mantle (SCLM) position from McDonough (1990).

4.2.4 Possible geochemical reservoirs

Another use of Figure 4.7 is to determine potential sources for these rocks. The low $(Sm/Yb)_N$ and moderate to high $(La/Sm)_N$ region of the diagram is occupied by the heterogenous SCLM (McDonough, 1990). Group C and the CIF are observed to trend toward this area implying that enriched SCLM is a possible source of these rocks. The ultrapotassic rocks (such as the minettes and lamproites of the CIF) and the alkaline basalts (such as Group C; Figure 3.5) can both be derived from the SCLM (McDonough, 1990, and references therein). Groups A and B are also observed to occupy the portion of Figure 4.7 between the DM and the SCLM, making a less enriched SCLM the likely source for these rocks.

The variably metasomatized SCLM source postulated for these suites is supported by the Nd-Sr isotope diagram (Figure 4.5), where the samples plot in the lower right, 'enriched' quadrant. As observed in the inset of Figure 4.5 the Groups A, B, C and the CIF describe a sub-vertical trend towards EM II, the metasomatized mantle reservoir (Zindler and Hart, 1986). This is interpreted as support for the argument made here that the CIF are, relative to the other groups, the most metasomatized suite. Groups A and B are least metasomatized, whereas Group C shows moderate metasomatism. That they plot away from EM II (upper continental crust; Zindler and Hart, 1986) reinforces the earlier conclusion that these rocks have not been crustally contaminated.

4.3 Petrogenetic model

The arguments and observations made above may be integrated into a petrogenetic model that is capable of reconciling the different igneous lithologies emplaced at *ca.* 1830 Ma in the Churchill Province. Such a model is illustrated in Figure 4.8 and described below.

All suites show a high incompatible element abundances and large negative Nb anomaly, indicating that the source enrichment could be metasomatizing fluids from a dehydrating slab of subducted oceanic crust, as aruged by Cousens *et al.* (2001, 2004). That all four suites plot in the enriched quadrant of the ϵNd vs. initial $^{87}Sr/^{86}Sr$ plot (i.e., Figure 4.5) supports the argument that their sources have experienced metasomatism. The relative positions of the suites in that plot indicate that the degree of metasomatism is lowest for the source of Groups A and B, moderate for the Group C source and highest for the CIF source.

In agreement with Cousens *et al.* (2001, 2004), the present study argues that a metasomatized SCLM is the source for the ultrapotassic and incompatible element rich rocks of the CIF. This is supported by the very negative ϵNd values (-10.8 to -4.5) and high initial $^{87}Sr/^{86}Sr$ (0.7050). The residual garnet signature in the REE profiles of the CIF, as observed in Figure 4.2(a), suggests that the source region was below 75 kilometres (McDonough, 1990). The negative Eu anomaly observed in CIF samples, as seen in Figure 4.2(a), may indicate that, prior to emplacement, the melts may have accumulated at depths less than $\sim$30 kilometres where plagioclase could crystallize out (McKenzie and O'Nions, 1991).

In Figure 4.2, the Group C rocks show incompatible element abundances

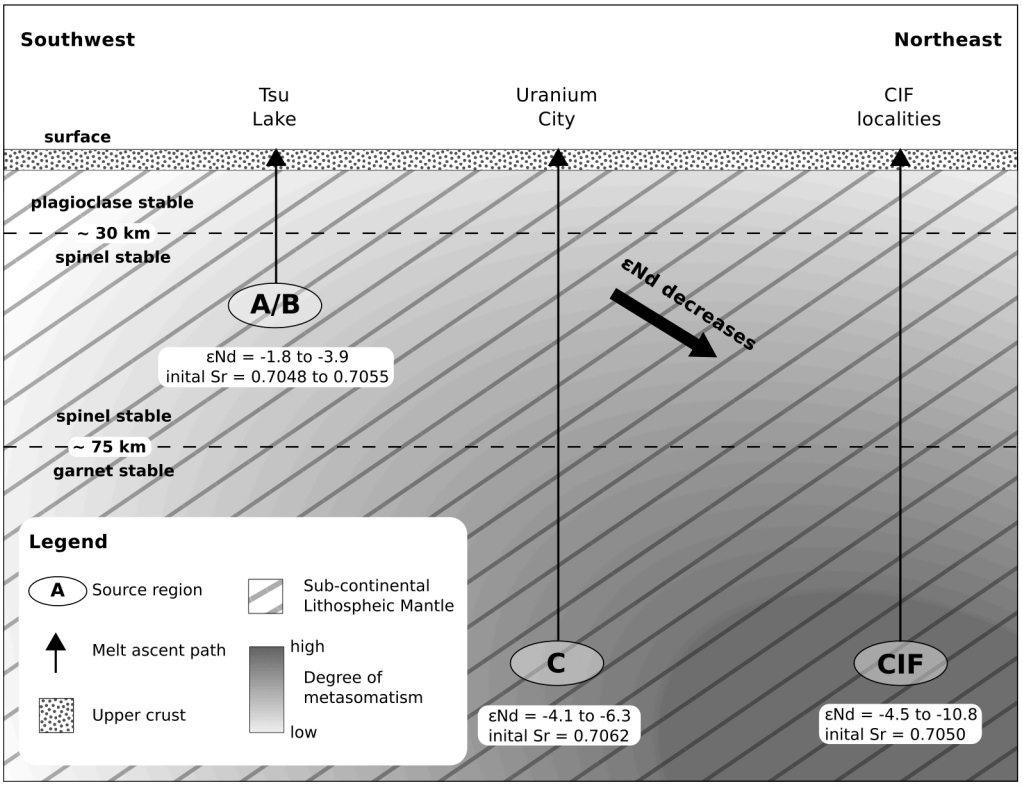

Figure 4.8: A petrogenetic model and conceptual cross section running NE-SW of the Churchill Province and the lithospheric mantle beneath it at *ca.* 1830 Ma. Group C and the CIF are sourced from depths at which garnet is stable, from an SCLM that displays metasomatic overprint that increases with depth to the NE. This metasomatism could be the result of ancient subduction, as argued by Cousens *et al.* (2001). Groups A and B, the farthest SW, are sourced from less metasomatized SCLM, with Group B being emplaced slightly earlier than Group A, see text for details.

similar to the CIF and the REE profiles suggest similar minimum source depth (i.e., >75 kilometres) and possible plagioclase fractionation prior to emplacement. The ϵNd values for Group C are less negative (-6.3 to -4.1) than the CIF, indicating less incompatible element enrichment from the metasomatism responsible for enriching the CIF source. This difference in the metasomatism of Group C is supported by the low TiO_2 content and the position on the calc-alkaline trend of the AFM diagram (Figure 4.6), indicating the metasomatic fluid affecting that source that was relatively poor in water compared to that for the CIF.

Compared with Group C and the CIF, the Group A and B rocks are less enriched in the incompatible elements and their flat HREE profiles indicate that garnet was not present in the source (Figure 4.2). The lack of a Eu anomaly in these groups, as observed in Figure 4.2(a), indicates that the source was not so shallow that plagioclase was stable, thus placing its depth between $\sim$30 and $\sim$75 kilometres (McKenzie and O'Nions, 1991). Additionally, their position between DM and SCLM in Figure 4.7 indicates that they are from an SCLM source that is not as enriched as for Group C and the CIF. Relative to Group C and the CIF, Group A and B also show less negative ϵNd (-3.9 to -1.8), supporting the argument. The tholeiitic nature of Groups A and B requires a source relatively poor in H_2O, which, with the preceding observations, indicates a lower degree of metasomatic enrichment of the source.

Group B is LREE enriched compared to Group A in Figure 4.2(a) and is also slightly older, as indicated by the cross-cutting relationship in the Granddaddy dyke (Figure 3.3). This implies that Group B magmas traversed the SCLM before Group A. Thus, if the two magmas utilized the same plumbing

system, incompatible elements (e.g., the LREE) residing in the lithospheric wall-rocks would be taken up by the earlier Group B magmas, leaving a more refractory lithosphere for Group A to travel through. This more refractory lithosphere would not contaminate Group A magmas to the same extent. This would produce the elevated LREE abundance observed in Figure 4.2(a), slightly more negative ϵNd and higher initial $^{87}Sr/^{86}Sr$ of Group B relative to Group A (Figure 4.5).

This model fits the observed geographic distribution (Figure 4.9), wherein the metasomatic enrichment of the rocks increases from Groups A and B in the SW to the CIF in the NE, with the moderately metasomatized Group C in between. This model implies that the source of metasomatism that most dramatically affected the SCLM was at depth in the NE. However, it does not exclude the possibility of smaller, localized metasomatic events whose evidence may be obscured by this larger, more influential one. Indeed, there is the hint of an aqueous metasomatic enrichment in the SW as indicated by the increase in initial $^{87}Sr/^{86}Sr$ between Groups A/B and Group C.

4.3.1 An alternate petrogenetic model

Peterson *et al.* (2002, 2010) propose a model for the enrichment of the CIF source involving the imbrication of the middle crust and mantle in the lithosphere by continent-continent collision, possibly associated with the assembly of the Paleoproterozoic (*ca.* 1.9–1.8 Ga) supercontinent Nuna. In that model, mixed melts of the crust and mantle would produce the highly enriched signature of the CIF. Groups A and B from the present study indicate derivation from the less enriched source, which can be reconciled in the Peterson *et al.*

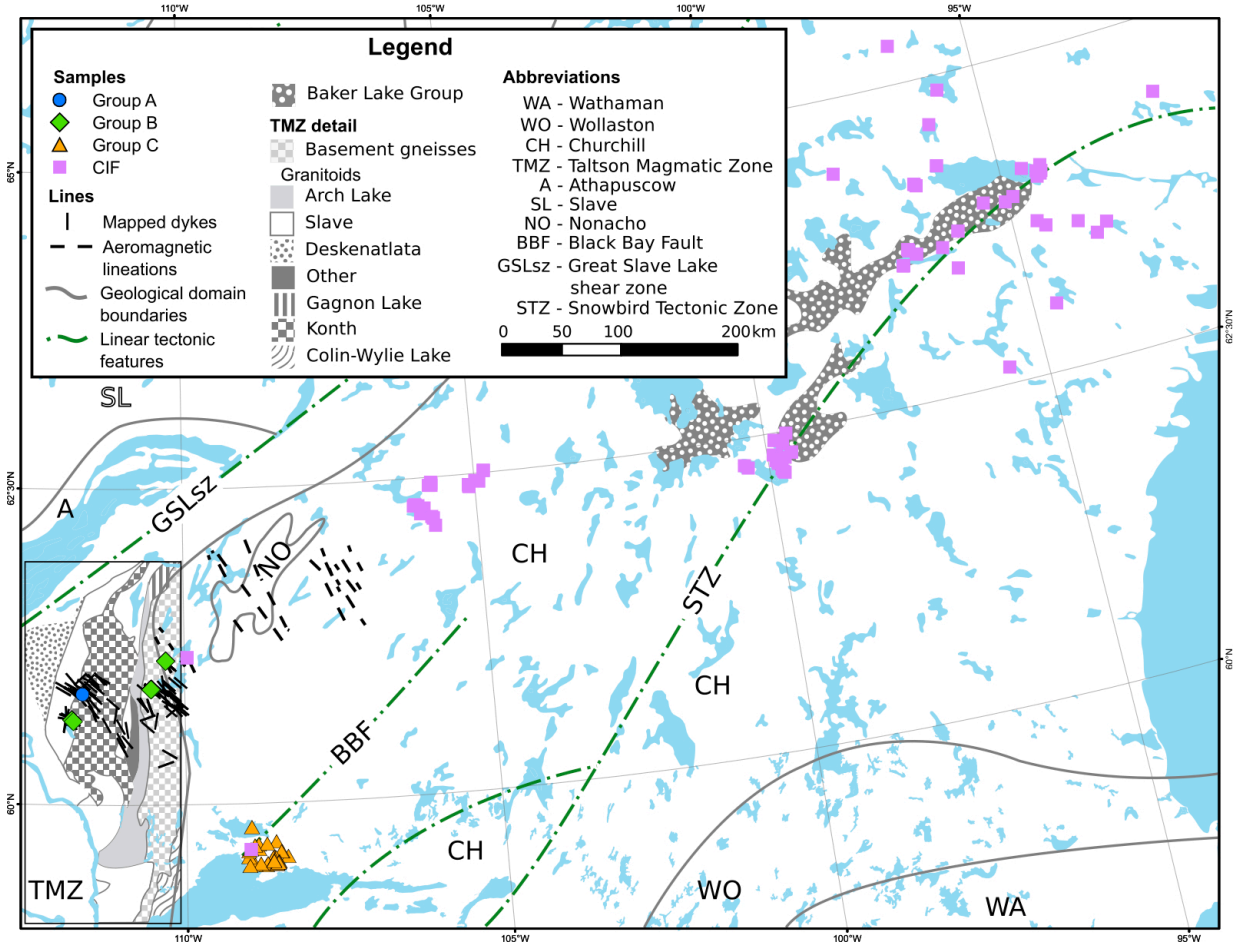

Figure 4.9: Geographic map of sample distribution, coded by group. Regional geology (including TMZ detail) are from Chacko *et al.* (2000) and references therein. Location of BBF from Morelli *et al.* (2009) and the extent of the Baker Lake Group is from Paul *et al.* (2002). Detailed geology of the Uranium City area is visible in Figure 3.4.

(2002, 2010) model as melts of a mantle wedge that did not mix with crustal melts.

Conceptually, however, the mixing of crustal and mantle melts in varying proportions to produce the CIF would produce the same geochemical signature as contamination of mantle melts with crustal material, as described previously. The present work and that of Cousens *et al.* (2001) demonstrates that the CIF (and the CIF-like Group C rocks) do not show the major- and trace-element characteristics of contamination with crustal material. The Peterson *et al.* (2002, 2010) model is possible, however, if the imbricated crust only dehydrated, instead of melting. The fluids released could enrich the mantle with incompatible elements, impart the observed isotopic signatures and show no sign of crustal contamination, as observed for the CIF and the rocks of the present study.

4.4 Tectonic model and trigger for source melting

The major tectonic events during the emplacement of these rocks, were the terminal stages of the Trans-Hudson Orogeny (THO), which juxtaposed the Superior Province against the east and southeast margins of the Churchill Province (Hoffman, 1988; Corrigan *et al.*, 2009). The stress-field required for this would have been oriented with the σ_1 (principal compressive stress) axis trending NW–SE. If the σ_3 (principal extensional stress; perpendicular to σ_1) axis was horizontal, the stress-field would tend to generate extensional fractures that open perpendicular to σ_1, but striking parallel to it (i.e., a vertical plane striking $\sim$130°).

If this extension is sufficient, it might result in decompression-melting of the

underlying mantle (Foucher *et al.*, 1982), aided by the presence of the metasomatic fluids that enriched the SCLM. These melts would then rise through the lithosphere and crust as dykes, exploiting the planes of weakness created by the extensional fractures. There is support for this model from Vaughan and Scarrow (2003) and Scarrow *et al.* (2011), who have postulated a genetic link between trans-tensional stress regimes (i.e., extension associated with oblique compression) and the melting of enriched mantle, producing ultrapotassic rocks such as those observed in the CIF. Such a trans-tensional stress regime has also been inferred for the internal belts of the THO by Hoffman (1988), resulting from sinistral shear in a N–S compressive stress regime.

The predicted orientation of the σ_3 stress axis fits well with the $\sim$130° orientation of mafic dykes in the study area of the present work. The orientations of dykes in the NT are $\sim$130° (Ewanchuk, 2006; this study) and aeromagnetic maps (NTGO, 2007) indicate a regionally extensive system of linear magnetic highs trending similarly, including one that corresponds to the bostonite dyke found at Thekulthili Lake. Additionally, historic maps from the Geological Survey of Canada (Alcock, 1936; Henderson, 1939a,b; Wilson, 1941; McGlynn, 1978; Bostock, 1982) indicate regionally extensive occurrences of mafic dykes with a similar trend. Morelli (2000) also demonstrated that the mafic dykes around Uranium City, SK, trend predominantly 130°, similar to the orientations of fractures in that area. The CIF also has a considerable number of dykes trending 100-130° (Peterson *et al.*, 2010), though other orientations are present as well.

A possible consequence of this tectonic model is the symmetric emplacement of mafic dykes on the other side of the THO (i.e., within the Superior

Province). As indicated by Ernst and Buchan (2004), the only mafic dykes observed immediately east of the THO are from the Mackenzie Dyke Swarm and the Molson Igneous Event, which are dated at 1.27 Ga (LeCheminant and Heaman, 1989) and 1.88 Ga (Heaman *et al.*, 1986, 2009), respectively. These ages clearly preclude those events from being related with the event responsible for the dykes of the present study.

Although it is possible that 1.83 Ga dykes have not yet been recognized on the Superior Province's side of the THO, it is more likely that asymmetry in the rheological conditions across the orogeny favoured the development of extensional fractures and mantle melting only on the Churchill-side of the THO. This is supported by the distribution of regional metamorphism related to the the THO. This zone is ∼900 kilometres wide in the Churchill Province and narrow in the Superior Province (Corrigan *et al.*, 2009), indicating that the lithosphere in the Churchill was likely hotter, thus more easily metamorphosed and more likely to experience melting as described above.

4.4.1 An alternate melting trigger

Conceptually, the head of a mantle plume impinging on the base of the lithosphere could cause the melting of the latter, without imparting a plume geochemical signature to the melts. Such melts could be emplaced along planes of weakness created by the tectonic environment, as described above. This would not show the expected radiating distribution of dykes (e.g., Ernst *et al.*, 1995) and the crustal uplift associated with plumes (Hill, 1991) could be masked by uplift associated with the ongoing THO. This could happen in conjunction with, or independent of, the melting process described above. The

present study is not able to conclusively indicate or invalidate this possibility.

4.5 Comparison with the Molson Igneous Event

The dominant tectonic regime over the period from 1.92 to 1.80 Ga was compressive, related to the Trans-Hudson Orogeny (Hoffman, 1988; Corrigan *et al.*, 2009). The dykes of the present study were emplaced in the western Churchill province at *ca.* 1830 Ma, during the terminal stages of collision. At *ca.* 1880 Ma, during the collision of the Snow Lake belt with the northwest Superior craton (i.e., a part of the Trans-Hudson Orogeny; Corrigan *et al.*, 2009, and references therein), the dykes of the Molson Igneous Event (MIE) were emplaced on the northwest margin of the Superior craton, in present-day Manitoba (Heaman *et al.*, 1986, 2009). The reason why the rocks of the MIE will be compared with those of the present study is because of the similarity in the ages and tectonic settings of these events.

The incompatible- and major-element geochemistry of the rocks of the MIE (presented in Figures 4.3, 4.6(a) and 4.7; data from Heaman *et al.*, 2009) is most similar to that of Groups A and B of the present study, implying that they are also from a similar non-enriched source. Unlike Groups A and B, however, the MIE suite has a consistently positive $\epsilon \mathrm{Nd}_{1880\ Ma}$ (up to +5; Chauvel *et al.*, 1987; Desharnais *et al.*, 2002), indicating that they are closer in composition to Depleted Mantle than enriched SCLM.

Chapter 5

Conclusions

The objective of the present study was to check the validity of the correlations of the Sparrow Dyke Swarm (McGlynn *et al.*, 1974) with the dykes at Tsu Lake, NT, (Ewanchuk, 2006) and the Martin Group Igneous Rocks (MGIR), near Uranium City, SK, (Morelli *et al.*, 2009). As no geochemical data has been available for the Sparrow Dyke Swarm to date, those authors made these correlations on the basis of similarity in trend ($\sim$130°) and time of emplacement (*ca.* 1830 Ma). A second objective of the present study was to use the geochemical data obtained herein and those of the Christopher Island Formation (CIF; data from Cousens *et al.*, 2001) to infer the nature of the mantle underlying the western Churchill Province. Finally, this study aimed to tie the lithologies and geochemistry of these rocks into a single petrogenetic and tectonic model.

5.1 Correlations

The present study has determined that the Jerome Lake dyke (from the Sparrow Dyke Swarm, as defined by McGlynn *et al.*, 1974) is geochemically

similar to some of the ∼130°-trending dykes at Tsu Lake (called 'Group B' in the present study). As discussed above, these groups are defined based on similarity of REE profiles of the samples. They also show similar incompatible element abundances on spidergrams and have radiogenic isotope compositions, making it likely that they shared the same source. The age of the Taltson River dyke (at Tsu Lake) is *ca.* 1830 Ma (Heaman, pers. comm.), confirming the correlation with the Sparrow Dyke Swarm (dated at 1827 ± 4 Ma; Bostock and van Breemen, 1992), as postulated by Ewanchuk (2006).

However, at Tsu Lake (and other locations), there is a slightly younger mafic lithology associated with Group B that is less enriched in LREE, less negative in ϵNd and lower in initial $^{87}Sr/^{86}Sr$. This lithology, referred to as 'Group A' in the present study, is evidently younger than Group B, as observed by its cross-cutting relationship at the 'Grand-daddy Dyke' at Tsu Lake. Furthermore, although no geochronology has been carried out quantify this, it is likely that the time between the emplacement of these two groups was very short given that Group A shows no chill-margin at its contact with Group B. Thus, it is argued that the Sparrow Dyke Swarm exhibits two geochemical signatures that are the result of differing contamination from the SCLM during ascent.

Morelli *et al.* (2009) dated the MGIR (Group C, in the present study) at 1818 ± 4 Ma and tentatively correlated them with the Sparrow Dyke Swarm on the basis of similarities in petrography and timing. However, this correlation is not tenable as the former are considerably more enriched in incompatible elements, have more negative ϵNd values and higher initial $^{87}Sr/^{86}Sr$ than Groups A and B. However, Group C is very similar to the Christopher Island

Formation (CIF; Peterson *et al.*, 1994; Cousens *et al.*, 2001, 2004), emplaced at *ca.* 1830 Ma (Rainbird *et al.*, 2006).

5.2 Sources

The evidence presented and discussed in the present study argues for a metasomatized Sub-Continental Lithospheric Mantle (SCLM) beneath the Churchill Province during the Paleoproterozoic. The degree of metasomatism appears to vary, laterally and vertically: the shallow source for the Sparrow Dyke Swarm (i.e., Groups A and B) to the SW is inferred to be less metasomatized than the deeper source of Group C and the CIF to the NE. The negative Nb anomalies associated with these four suites indicates that the metasomatizing fluids were possibly derived from a subducting slab. ϵNd values are not correlated with SiO_2 or other crustal contamination monitors, indicating that the geochemical differences between these groups are not the result of crustal contamination, but instead reflect varying degrees of metasomatic enrichment.

The ϵNd values and initial $^{87}Sr/^{86}Sr$ composition of the Sparrow dykes indicates a source that is more enriched than the Depleted Mantle at 1830 Ma (McCulloch and Wasserburg, 1978). As suggested by the REE data, the depth of melting of this source is between $\sim$30 and $\sim$75 kilometres, where spinel is stable (McKenzie and O'Nions, 1991). The tholeiitic nature of these rocks implies that the water content of the source was relatively minor. The LREE enrichment of Group B of the Sparrow dykes is likely due to contamination with the SCLM that those magmas traversed. Group A, rising through this SCLM after Group B would experience less of this contamination. This is supported by the lower incompatible element abundances and less radiogenic

Nd and Sr isotopes of Group A relative to Group B.

The ultrapotassic CIF and the alkaline Group C rocks are from an SCLM source that is more metasomatized than that of the Sparrow Dyke Swarm. The enriched incompatible element abundances of these groups is attributed to metasomatic enrichment by fluids associated with the subduction modification. Although both groups are on the calc-alkaline trend, the higher TiO_2 content of the Group C rocks indicates that their source had a lower water content than the CIF source. This is supported by the observation that the alkaline basalts of Group C do not contain any primary hydrous phases like biotite, whereas the CIF minettes and lamproites do (Le Maitre, 2002; Cousens *et al.*, 2001, 2004). The present study argues that this indicates that the Group C source was less metasomatized than the CIF source, which is also supported by the less negative ϵNd of those samples compared to the CIF. The REE data indicates that the source of these rocks must have melted below ∼75 kilometres, where garnet is stable (McKenzie and O'Nions, 1991). A negative Eu anomaly is present in both groups, possibly implying that the melts accumulated at depths less than ∼30 kilometres, allowing plagioclase to fractionate out (McKenzie and O'Nions, 1991).

5.3 Petrogenetic and tectonic model

The present study argues that these sources were melted as a result of decompression from the lithospheric extension associated with the terminal stages of the Trans-Hudson Orogeny. The present study is not able to rule out the possibility that this melting of the lithospheric mantle was enhanced by the heating from an underlying plume. These melts then travelled through

the lithosphere, exploiting expansion fractures associated with the compressive stress of the Trans-Hudson Orogeny. The general trend of the dykes of Groups A, B, C and the CIF corresponds with the predicted orientation of these fractures, supporting this idea.

5.4 Outstanding issues and questions

A number of issues have been raised in this work that have not been resolved:

1. Geochronology of Group A dykes should be carried out, if possible, to corroborate or refute the inferred age of emplacement of that magma. Currently the temporal relationship is inferred by Group A's cross-cutting of Group B rocks and the lack of a chill margin as observed at the 'Granddaddy Dyke'at Tsu Lake, NT.

2. At present, the across-trend extent of the Sparrow Dyke Swarm (of which Groups A and B are members) is unknown. Reconnaissance and exploration farther to the west and southwest will provide better indication of the size of the Sparrow Dyke Swarm and, by extension, its source.

3. Complex commingling of granitoid and mafic magmas, displayed magnificently at the Taltson River dyke, location near Tsu Lake, has not been addressed. Ages previously obtained from these lithologies are discordant and inconclusive (Heaman, pers. comm.). Sandeman *et al.* (2000) have reported evidence for *ca.* 1830 Ma commingling between mafic and granitoid lithologies around Rankin Inlet (NU), in the vicinity of the CIF. Geochemical comparison of the lithologies from these two areas

(i.e., the Taltson River and Rankin Inlet localities) will provide insights into this phenomenon.

4. A study of hand samples and thin-sections from the CIF would be most valuable for directly comparing lithologies with Group C samples.

5. Bostonite dykes at Thekulthili Lake (NT) and Uranium City (SK) are geochemically and petrographically similar to the bostonite samples of the Christopher Island Formation (Cousens, pers. comm.; Pehrsson, pers. comm.; Peterson, pers. comm.), thereby extending the range of the CIF approximately 100 kilometres farther west, and confirming its extent as far SW as Uranium City. Bostonites around Baker Lake and other core CIF areas are associated with economic hydrothermal mineralization, as are the bostonites near Uranium City (Pehrsson, pers. comm.; Ashton, pers. comm.). This provides an exciting avenue for future exploration and research into the iron, copper, gold, uranium and REE potential over a vast area of the Churchill Province.

Bibliography

Alcock, F. J.: 1936, Map 363A - Tazin Lake Sheet, Northern Saskatchewan, Geological Survey of Canada, "A" Series Map.

Ansdell, K. M.: 2005, Tectonic evolution of the Manitoba–Saskatchewan segment of the Paleoproterozoic Trans-Hudson Orogen, Canada, *Canadian Journal of Earth Sciences* **42**, 741–759.

Arth, J. G.: 1976, Behaviour of trace elements during magmatic processes – a summary of theoretical models and their applications, *Journal of Research of the U.S. Geological Survey* **4**(1), 41–47.

Ashton, K. E., Hartlaub, R. P., Heaman, L. M., Morelli, R. M., Card, C. D., Bethune, K. and Hunter, R. C.: 2009, Post-Taltson sedimentary and intrusive history of the southern Rae Province along the northern margin of the Athabasca Basin, Western Canadian Shield, *Precambrian Research* **175**, 16–34.

Baragar, W. R. A., Ernst, R. E., Hubert, L. and Peterson, T. D.: 1996, Logitudinal petrochemical variation in the mackenzie dyke swarm, northwestern canadaian shield, *Journal of Petrology* **37**(2), 317–359.

Böhm, C. O., Zwanzig, H. V. and Creaser, R. A.: 2007, Sm-Nd isotope technique as exploration tool: delineating the north extension of the Thompson Nickel Belt, Manitoba, Canada, *Economic Geology* **102**, 1217–1231.

Bostock, H. H.: 1982, Map 859 - Geology of the Fort Smith map area, District of Mackenzie, Northwest Territories, Geological Survey of Canada, Open File.

Bostock, H. H. and van Breemen, O.: 1992, The timing of emplacement, and distribution of the Sparrow diabase dyke swarm, District of Mackenzie, Northwest Territories, *Radiogenic Age and Isotopic Studies: Report 6* **92-2**, 49–55.

Bostock, H. H. and van Breemen, O.: 1994, Ages of detrital and metamorphic zircons and monazites from a pre- Taltson magmatic zone basin at the western margin of Rae Province, *Canadian Journal of Earth Sciences* **31**(8), 1353–1364.

Bougault, H., Joron, J. L. and Treuil, M.: 1980, The primordial chondritic nature and large-scale heterogeneities in the mantle: evidence from high and low partition coefficient elements in oceanic basalts, *Philosophical Transactions of The Royal Society Series A* **297**, 203–213.

Brewer, T. S. and Atkins, B. P.: 1989, Element mobilities produced by low grade metamorphic events. A case study from the Proterozoic of sourthern Norway., *Precambrian Research* **45**, 143–158.

Buchan, K. L. and Ernst, R. E.: 2004, Map 2022A - Diabase dyke swarms and

related units in Canada and adjacent regions, Geological Survey of Canada Map.

Buzon, M. R., Simonetti, A. and Creaser, R. A.: 2007, Migration in the Nile Valley during the New Kingdom Period: A Preliminary Strontium Isotope Study, *Journal of Archaeological Science* **34**, 1391–1401.

Campbell, I. H.: 2005, Large Igneous Provinces and the Mantle Plume Hypothesis, *Elements* **1**, 265–269.

Chacko, T., De, S. K., Creaser, R. A. and Muehlenbachs, K.: 2000, Tectonic setting of the Taltson magmatic zone at 1.9-2.0 Ga: a granitoid-based perspective, *Canadian Journal of Earth Sciences* **37**, 1597–1609.

Chauvel, C., Arndt, N. T., Kielinczuk, S. and Thom, A.: 1987, Formation of Canadian 1.9 Ga old continental crust. I: Nd isotopic data., *Canadian Journal of Earth Sciences* **24**(3), 396–406.

Coffin, M. F. and Eldholm, O.: 1993, Scratching the surface: estimating dimensions of large igneous provinces, *Geology* **21**(6), 515–518.

Coffin, M. F. and Eldholm, O. (eds): 1991, *Large Igneous Provinces: JOI/USSAC Workshop Report*, Vol. 114, Austin, TX, p. 79.

Condie, K. C.: 1997, Sources of Paleoproterozoic mafic dyke swarms: constraints from Th/Ta and La/Yb ratios, *Precambrian Research* **81**, 3–14.

Corrigan, D., Pehrsson, S., Wodicka, N. and De Kemp, E.: 2009, *Ancient Orogens and Modern Analogues*, Vol. 327 of *Special Publications*, Geological Society of London, London, U.K., chapter The Palaeoproterozoic Trans-Hudson Orogen: a prototype of modern accretionary processes, pp. 457–479.

Cousens, B. L., Aspler, L. B., Chiarenzelli, J. R., Donaldson, J. A., Sandeman, H., Peterson, T. D. and LeCheminant, A. N.: 2001, Enriched Archean lithospheric mantle beneath western Churchill Province tapped during Paleoproterozoic orogenesis, *Geology* **29**(9), 827–830.

Cousens, B. L., Chiarenzelli, J. R. and Aspler, L. B.: 2004, *The Precambrian Earth: Tempos and Events*, number 3.5 in *Developments in Precambrian Geology*, Elsevier Science, chapter An unusual Palaeoproterozoic magamatic event, the ultrapotassic Christopher Island Formation, Baker Lake group, Nunavut, Canada: Archaean Mantle Metasomatism and Palaeoproterozoic mantle reactivation, pp. 183–201.

Creaser, R. A., Grütter, H. S., Carlson, J. and Crawford, B.: 2004, Macrocrystal phlogopite Rb-Sr dates for the Ekati property kimberlites: Evidence for multiple intrusive episodes during Paleocene and Eocene time, *Lithos* **76**, 399–414.

De, S. K., Chacko, T., Creaser, R. A. and Muehlenbachs, K.: 2000, Geochemical and Nd-Pb-O isotope systematics of granites from the Taltson Magmatic Zone, NE Alberta: implications for early Proterozoic tectonics in western Laurentia, *Precambrian Research* **102**, 221–249.

DePaolo, D. J. and Wasserburg, G. J.: 1976, Nd Isotopic Variation and Petrogenetic Models, *Geophysical Research Letters* **3**(5), 249–252.

Desharnais, G., Halden, N. M., Scoates, J. S., Weis, D., Peck, D. and Scoates, R. F. J.: 2002, Hf and Nd isotopic geochemistry of the Fox River Belt, Superior Boundary Zone, Manitoba: Implications for source compositions,

crustal contamination and mineral exploration , Program with Abstracts, Geological Association of Canada, p. 27.

Elkins-Tanton, L. and Hager, B. H.: 2000, Melt intrusion as a trigger for lithospheric foundering and the eruption of the Siberian flood basalts, *Geophysical Research Letters* **27**(23), 3937–3940.

Ernst, R. E. and Buchan, K. L.: 2004, Igneous Rock Associations in Canada 3. Large Igneous Provinces (LIPs) in Canada and Adjacent Regions: 3 Ga to present, *Geoscience Canada* **31**, 103–126.

Ernst, R. E., Head, J. W., Parfitt, E., Grosfils, E. and Wilson, L.: 1995, Giant radiating dyke swarms on Earth and Venus, *Earth Science Reviews* **39**, 1–58.

Ewanchuk, S.: 2006, Distribution and nature of Basaltic Dykes, Tsu Lake, Northwest Territories. Undergraduate thesis.

Foucher, J. P., Le Pichon, X. and Sibuet, J. C.: 1982, The ocean-continent transition in the uniform lithospheric stretching model: role of partial melting in the mantle, *Philosophical Transactions of The Royal Society Series A* **305**(1489), 27–43.

Gill, J. B.: 1981, *Orogenic Andesites and Plate Tectonics*, Springer-Verlag, New York, USA.

Harlan, S., Heaman, L. M., LeCheminant, A. N. and Premo, W. R.: 2003, Gunbarrel mafic magmatic event: A key 780 Ma time marker for Rodinia plate reconstructions, *Geology* **31**, 1053–1056.

Hartlaub, R. P., Chacko, T., Heaman, L. M., Creaser, R. A., Ashton, K. E. and Simonetti, A.: 2005, Ancient (Meso- to Paleoarchean) crust in the Rae

Province, Canada: Evidence from Sm–Nd and U–Pb constraints, *Precambrian Research* **141**, 137–153.

Heaman, L. M., Machado, N., Krogh, T. E. and Weber, W.: 1986, Precise U-Pb zircon ages of the Molson dyke swarm and the Fox River sill: Constraints for Early Proterozoic crustal evolution in northeastern Manitoba, Canada, *Contributions to Mineralogy and Petrology* **94**, 82–89.

Heaman, L. M., Peck, D. and Toope, K.: 2009, Timing and geochemistry of 1.88 Ga Molson Igneous Events, Manitoba: Insights into the formation of a craton-scale magmatic and metallogenic province, *Precambrian Research* **172**, 143–162.

Henderson, J. F.: 1939a, Map 525A - Taltson Lake, District of Mackenzie, Northwest Territories, Geological Survey of Canada, "A" Series Map.

Henderson, J. F.: 1939b, Map 526A - Nonacho Lake, District of Mackenzie, Northwest Territories, Geological Survey of Canada, "A" Series Map.

Hill, I. R.: 1991, Starting plumes and continental break up, *Earth and Planetary Science Letters* **104**, 398–416.

Hoffman, P. F.: 1988, United Plate of America, the birth of a craton: Early Proterozoic Assembly and Growth of Laurentia, *Annual Reviews of Earth and Planetary Sciences* **16**, 543–603.

Holmden, C. E., Creaser, R. A. and Muehlenbachs, K.: 1997, Paleosalinities in brackish water environments: A method based on the isotopic paleohydrology of strontium, *Geochimica et Cosmochimica Acta* **61**, 2105–2118.

Irvine, T. N. and Baragar, W. R. A.: 1971, A Guide to the Chemical Classification of the Common Volcanic Rocks, *Canadian Journal of Earth Sciences* **8**, 523–548.

Irving, A. J. and Frey, F. A.: 1978, Distribution of trace elements between garnet megacrysts and host volcanic liquids of kimberlitic to rhyolitic composition, *Geochimica et Cosmochimica Acta* **42**, 771–787.

King, S. D. and Anderson, D. L.: 1998, Edge-driven convection, *Earth and Planetary Science Letters* **160**, 289–296.

Lassiter, J. C. and DePaolo, D. J.: 1997, *Large Igneous Provinces: Continental, Oceanic and Planetary*, Vol. 100 of *Geophysical Monograph*, American Geophysical Union, chapter Plume/Lithosphere Interaction in the Generation of Continental and Oceanic Flood Basalts: Chemical and Isotopic Constraints, pp. 335–355.

Le Maitre, R. W. (ed.): 2002, *Igneous Rocks: A Classification and Glossary of Terms, Recommendations of the International Union of Geological Sciences Subcommission on the Systematics of Igneous Rocks*, 2 edn, Cambridge Unversity Press, Cambridge, UK.

LeCheminant, A. N. and Heaman, L. M.: 1989, Mackenzie igneous events, Canada: Middle Proterozoic hotspot magmatism associated with ocean opening, *Earth and Planetary Science Letters* **96**, 38–48.

Ludwig, K. R.: 2003, *Isoplot 3.00, Special Publication No. 4, A Geochronological Toolkit for Microsoft Excel*, 3.00 edn, Berkeley Geochronology Center, 2455 Ridge Road, Berkeley CA 94709, USA.

Maxeiner, R. O. and Rayner, N.: 2011, Continental arc magmatism along the southeast Hearne Craton margin in Saskatchewan, Canada: Comparison of the 1.92–1.91 Ga Porter Bay Complex and the 1.86–1.85 Ga Wathaman Batholith, *Precambrian Research* **184**, 93–120.

McCulloch, M. T. and Gamble, J. A.: 1991, Geochemical and geodynamicai constraints on subduction zone magmatism, *Earth and Planetary Science Letters* **102**, 358–374.

McCulloch, M. T. and Wasserburg, G. J.: 1978, Sm-Nd and Rb-Sr Chronology of Continental Crust Formation, *Science* **200**(4345), 1003–1011.

McDonough, W. F.: 1990, Constraints of the composition of the continental lithospheric mantle, *Earth and Planetary Science Letters* **101**, 1–18.

McDonough, W. F. and Sun, S. s.: 1995, The composition of the Earth, *Chemical Geology* **120**, 223–253.

McGlynn, J. C.: 1978, Map 543 - Geology of Nonacho Basin, District of Mackenzie, Geological Survey of Canada, Open File.

McGlynn, J. C., Hanson, G. N., Irving, E. and Park, J. K.: 1974, Paleomagnetism and Age of Nonacho Group Sandstones and Associated Sparrow Dikes, District of Mackenzie, *Canadian Journal of Earth Sciences* **11**, 30–42.

McKenzie, D. and O'Nions, R. K.: 1991, Partial Melt Distributions from Inversion of Rare Earth Element Concentrations, *Journal of Petrology* **32**(5), 1021–1091.

Morelli, R. M.: 2000, Geology and Geochemistry of Igneous Rocks Associated

with the Martin Basin, Beaverlodge Domain, Northwestern Saskatchewan. Undergraduate thesis.

Morelli, R. M., Hartlaub, R. P., Ashton, K. E. and Ansdell, K. M.: 2009, Evidence for enrichment of subcontinental lithospheric mantle from Paleoproterozoic intracratonic magmas: Geochemistry and U–Pb geochronology of Martin Group igneous rocks, western Rae Craton, Canada, *Precambrian Research* **175**, 1–15.

Morgan, W. J.: 1971, Convection plumes in the lower mantle, *Nature* **230**, 42–43.

Muecke, G., Pride, C. and Sarkar, P.: 1979, Rare-earth element geochemistry of regional metamorphic rocks, *Physics and Chemistry of the Earth* **11**(449-464).

Nelson, D. R., Chivas, A. R., Chappell, B. W. and McCulloch, M. T.: 1988, Geochemical and isotopic systematics in carbonatites and implications for the evolution of ocean-island sources, *Geochimica et Cosmochimica Acta* **52**, 1–17.

NTGO: 2007, High resolution total field and gradient aeromagnetic survey of the Nonacho Basin and Environs, Northwest Territories, parts of NTS 75E, 75F and 75G, *Northwest Territories Geoscience Office, NWT Open File* **2007-04**, 8 1:100,000 scale maps, digital data and report.

Paul, D., Hanmer, S., Tella, S., Peterson, T. D. and LeCheminant, A. N.: 2002, Map 4236 - Compilation, Bedrock Geology of part of the Western Churchill Province, Geological Survey of Canada, Open File.

Pearce, J. A.: 1982, *Andesites: Orogenic andesites and related rocks*, 526-547 edn, Wiley, Chichester, chapter Trace element characteristics of lavas from destructive plate boundaries.

Pearce, J. A.: 1983, *Continental Basalts and Mantle Xenoliths*, Shiva, Nantwich, England, chapter The role of sub-continental lithosphere in magma genesis at destructive plate boundaries, pp. 230–249.

Peate, D. W. and Hawkesworth, C. J.: 1996, Lithospheric to asthenospheric transition in Low-Ti flood basalts from southern Paraná, Brazil, *Chemical Geology* **127**, 1–24.

Peterson, T. D., Esperança, S. and LeCheminant, A. N.: 1994, Geochemistry and origin of the Proterozoic ultrapotassic rocks of the Churchill Province, Canada, *Mineralogy and Petrology* **51**, 251–276.

Peterson, T. D., Pehrsson, S., Jefferson, C., Scott, J. and Rainbird, R.: 2010, The Dubawnt Supergroup, Canada: a LIP with a LISP. December 2010 LIP of the Month.
URL: *http://www.largeigneousprovinces.org/10dec*

Peterson, T. D., Scott, J. M. J. and Jefferson, C. W.: 2011, Uranium-rich bostonite-carbonatite dykes in Nunavut: recent observations, Vol. 2011-11 of *Current Research Paper*, Geological Survey of Canada, pp. 1–12.

Peterson, T. D., van Breemen, O., Sandeman, H. and Cousens, B. L.: 2002, Proterozoic (1.85–1.75 Ga) igneous suites of the Western Churchill Province: granitoid and ultrapotassic magmatism in a reworked Archean hinterland, *Precambrian Research* **119**, 73–100.

Rainbird, R. H., Smith, W. J., Stern, R. A., Peterson, T. D., Smith, S. R., Parrish, R. R. and Hadlari, T.: 2006, Ar-Ar and U-Pb Geochronology of a Late Paleoproterozoic Rift Basin: Support for a Genetic Link with Hudsonian Orogenesis, Western Churchill Province, Nunavut, Canada, *Journal of Geology* **114**, 1–17.

Rampino, M. R.: 1987, Impact cratering and flood-basalt volcanism, *Nature* **327**(6122), 468–468.

Ryerson, F. J. and Watson, E. B.: 1987, Rutile saturation in magmas: implications for Ti-Nb-Ta depletion in island-arc basalts, *Earth and Planetary Science Letters* **86**, 225–239.

Sandeman, H. A., Lepage, L. D., Ryan, J. J. and Tella, S.: 2000, Field evidence for commingling between ca. 1830 Ma lamprophyric, monzonitic, and monzogranitic magmas, MacQuoid-Gibson lakes area, Nunavut, Vol. 2000-C5 of *Current Research Paper*, Geological Survey of Canada, pp. 1–10.

Scarrow, J. H., Molina, J. F., Bea, F., Montero, P. and Vaughan, A. P. M.: 2011, Lamprophyre dikes as tectonic markers of late orogenic transtension timing and kinematics: A case study from the Central Iberian Zone, *Tectonics* **30**(TC4007), 1–22.

Schmidberger, S., Heaman, L. M., Simonetti, A., Creaser, R. A. and Whiteford, S.: 2007, Lu-Hf, in-situ Sr and Pb isotope and trace element systematics for mantle eclogites from the Diavik diamond mine: Evidence for Paleoproterozoic subduction beneath the Slave craton, Canada, *Earth and Planetary Science Letters* **254**, 55–68.

Sharpton, V. L., Grieve, R. A. F., Thomas, M. D. and Halpenny, J. F.: 1987, Horziontal gravity gradient: an aid to the definition of crustal structure in North America, *Geophysical Research Letters* **14**(808-11).

Sisson, T. W. and Grove, T. L.: 1993, Experimental investigations of the role of H_2O in calc-alkaline differentiation and subduction zone magmatism, *Contributions to Mineralogy and Petrology* **113**, 143–166.

Sun, S. s. and McDonough, W. F.: 1989, Chemical and isotopic systematics of oceanic basalts: implications for mantle composition and processes, *in* A. D. Saunders and M. J. Norry (eds), *Magmatism in the Ocean Basins*, Vol. 42 of *Special Publications*, Geological Society of London, pp. 313–345.

Taylor, S. R. and McLennan, S. M.: 1985, *The continental crust: its composition and evolution*, Blackwell, Oxford.

Thériault, R. J.: 1992, Nd isotopic evolution of the Taltson magmatic zone, Northwest Territories, Canada: insights into early Proterozoic accretion along the western margin of the Churchill Province, *Journal of Geology* **100**(4), 465–475.

Unterschutz, J. L. E., Creaser, R. A., Erdmer, P., Thompson, R. I. and Daughtry, K. L.: 2002, North American margin origin of Quesnel terrane strata in the southern Canadian Cordillera: Inferences from geochemical and Nd isotopic characteristics of Triassic metasedimentary rocks, *Geological Society of America Bulletin* **114**, 462–475.

Vaughan, A. P. M. and Scarrow, J. H.: 2003, K-rich mantle metasomatism

control of localization and initiation of lithospheric strike-slip faulting, *Terra Nova* **15**, 163–169.

Wanless, R. K.: 1979, Geochronology of Archean rocks of the Churchill Province, Program with Abstracts, Geological Association of Canada, p. 85.

White, R. and McKenzie, D.: 1989, Magmatism at rift zones - the generation of volcanic continental margins and flood basalts, *Journal of Geophysical Research* **94**(B6), 7685–7729.

Wilson, J. T.: 1941, Map 602A - Fort Smith, District of Mackenzie, Northwest Territories, Geological Survey of Canada, "A" Series Map.

Wood, D. A.: 1980, The application of a Th-Hf-Ta diagram to problems of tectonomagmatic classification and to establishimg the nature of crustal contamination of baslatic lavas of the British Tertiary Volcanic Province, *Earth and Planetary Science Letters* **50**, 11–30.

Zindler, A. and Hart, S.: 1986, Chemical Geodynamics, *Annual Reviews of Earth and Planetary Sciences* **14**, 493–571.

Appendix A

Sample locations

Table A.1: Locations of samples collected for this study and other details. All are mafic dykes, except the dyke at Thekulthili Lake, which is a 'bostonite' (Pehrsson, pers. comm.). Sample numbers are of the form RD10-ABC-xy, where ABC is the abbreviation as per Table 3.1 and xy is a unique identifier within the series.

Sample number	Easting[1]	Northing[1]	Width (m)	Orientation[2]	Texture[3]
Tsu Lake, 'Grand-daddy dyke' (Ewanchuk, 2006)					
RD10-129-01	454564	6726430	∼50	137/82	f.g., massive
RD10-129-01A	454564	6726430		-	f.g., chill margin
RD10-129-02	454564	6726430		-	f.g., massive
RD10-129-03	454564	6726430		-	c.g., amygdaloidal
RD10-129-04	454564	6726430		-	f.g., massive
RD10-129-05	454564	6726430		-	f.g., massive
RD10-129-06	454564	6726430		-	c.g., amygdaloidal
RD10-129-07	454553	6726 408		-	c.g., massive
RD10-129-08	454553	6726 408		-	c.g., massive
RD10-129-09	454553	6726 408		-	f.g., massive
RD10-129-10	454553	6726 408		-	f.g., massive
Tsu Lake, 'Taltson River dyke' (Ewanchuk, 2006)					
RD10-130-01	456091	6725242	∼30	-	c.g., massive
RD10-130-04	456091	6725242		-	f.g., sheared/faulted
Tsu Lake, dykes at location 751 (Ewanchuk, 2006)					
RD10-751-01	448790	6723166	∼1	-	f.g., granite veins
RD10-751-02	448736	6723189		-	f.g.

Continued on next page...

Table A.1 – continued

Sample number	Easting[1]	Northing[1]	Width (m)	Orientation[2]	Texture[3]
Nelson Lake dyke					
RD10-NEL-01	464262	6749122	unknown	126/90	f.g., chill margin
RD10-NEL-02	464262	6749122			c.g., massive
Jerome Lake dyke					
RD10-JER-01	537199	6778444	>40	-	c.g., massive
RD10-JER-02	537199	6778444		-	c.g., massive
RD10-JER-03	537210	6778444		-	c.g., massive
RD10-JER-04	537209	6778467		-	c.g., massive
RD10-JER-05A	537209	6778467		-	c.g., massive
Thekulthili Lake dyke; bostonite					
RD10-THK-01	556360	6781584	∼20	130/–	plagioclase-phyric, red colour
RD10-THK-02	556360	6781584			plagioclase-phyric, red colour
RD10-THK-03	556360	6781584			plagioclase-phyric, red colour
Lady Grey Lake dykes					
RD10-LGL-01	524485	6753315	∼1	136/80	f.g., with quartz veins
RD10-LGL-01A	524485	6753315		-	chill margin
RD10-LGL-02	524502	6753326	∼1	140/80	f.g.
RD10-LGL-03	524577	6753427	∼3	-	f.g.
RD10-LGL-04	524631	6753494	∼2	116/90	f.g.
RD10-LGL-05	524647	6753539	∼1	136/–	f.g.
RD10-LGL-05A	524647	6753539		-	chill margin
RD10-LGL-05B	524647	6753539	∼1	-	f.g.
RD10-LGL-06	524674	6753550	∼1	125/85	f.g.
RD10-LGL-06A	524674	6753550	∼2	-	f.g.

[1] UTM Zone 12, NAD '83.

[2] Right-hand rule.

[3] f.g. - fine-grained; c.g. - coarse-grained.

Appendix B

Petrographic thin-section descriptions

B.1 RD10-129-07

Minerals	Modal abundance (%)
plagioclase	60
clinopyroxene	20
quartz	10
opaques	<5
amphibole	<5

This section shows large, euhedral to subhedral, plagioclase laths >10 mm long, variably altered, but displaying lamellar and Carlsbad twinning. In places, plagioclase is seen co-mingling with quartz in irregular granophyric patches that are 0.3–1 mm across. Clinopyroxene is generally subhedral, ∼1 mm long, showing alteration in the cores, while clinopyroxene shows alteration in the rims. Opaque minerals are roughly equant, euhedral to subhedral, 0.3–0.9 mm across. These minerals are sometimes seen interfingering with other phases, but also poikilitic to the other phases. Amphibole is minor and, where visible, is seen to be an alteration of the clinopyroxene.

B.2 RD10-751-01

A mafic and felsic lithology are represented in this thin-section, accounting for 70% and 30% of the whole, respectively. The felsic lithology occurs as inclusions within the mafic component. These lithologies are treated separately.

B.2.1 Mafic portion

Minerals	Modal abundance (%)
plagioclase	50
quartz	20
amphibole	20
opaques	10

All crystals in this portion of the thin-section are very fine grained (<0.03 mm) and equant. There is a pervasive light brown to medium green staining visible, especially in the plagioclase. The green stained portions are pleochroic, from medium green to black. Crystals of quartz are very clean and randomly distributed in irregular patches. The numerous anhedral opaques occur in two size and shape classes: as equant crystals (<0.03 mm across) and as irregular ones (>0.03 mm across).

B.2.2 Felsic portion

Minerals	Modal abundance (%)
plagioclase	60
quartz	40

The anhedral, roughly equant crystals of quartz and plagioclase are seen in an interlocking texture. Quartz and plagioclase crystals are ∼0.15 mm and ∼0.3–0.45 mm across, respectively. Approximately two-thirds of the plagioclase is

altered to a very fine-grained (*i.e.* $\ll$0.03 mm), highly birefringent mineral.

Numerous, small lenses of the felsic lithology are distributed throughout the the mafic lithology, increasing in abundance with proximity to the major felsic portion. The boundaries of these lenses are fuzzy and very irregular. In places the mafic lithology is seen as inclusions within the felsic, but always near the margins of these lenses.

B.3 RD10-751-02

Minerals	**Modal abundance (%)**
plagioclase	35
clinopyroxene	25
amphibole	20
quartz	10
opaques	<5
orthopyroxene	<5

Quartz occurs as irregular, anhedral, roughly equant crystals, $\sim$0.15 mm across. All the plagioclase is present as altered, irregular, anhedral and roughly equant crystals, 0.15–0.4 mm across. Very faint, relict Carlsbad twinning is seen in the plagioclase. Clinopyroxene and, where seen, orthopyroxene, are unaltered, very pale green to medium green, with irregular borders. The pyroxenes are equant to lath-shaped crystals, 0.2–0.75 mm in the longest dimension. The amphibole is similar in size and shape to the pyroxenes, but display pleochroism from medium brown to dark brown. The opaques are very irregular, 0.03–0.9 mm across and appear to be space-filling.

B.4 RD10-NEL-01

Minerals	Modal abundance (%)
plagioclase	60
chlorite	25
opaques	10
amphibole	<5

Plagioclase and chlorite are both lath-shaped (randomly oriented) and semi-irregular to very irregular. Chlorite crystals are 0.15–0.9 mm long and plagioclase are generally 0.15 mm, though some crystals up to 0.9 mm long are also seen. Fresh crystals make up roughly 30% of the plagioclase population. The opaque minerals are 0.05–0.15 mm across, irregular and equant. Amphibole is similar in size and shape to the chlorite.

B.5 RD10-NEL-02

Minerals	Modal abundance (%)
plagioclase	60
orthopyroxene	15
amphibole	15
opaques	10
quartz	<2

Orthopyroxene is subhedral to anhedral, lath-shaped and large (>3mm long) or small (∼0.3 mm long). In places, orthopyroxene is observed to be gradationally altered to amphibole. Plagioclase sometimes occurs with quartz in granophyric texture, but, when alone, is euhedral to subhedral, 1–>3 mm long. Shards of a highly bi-refringent mineral are seen as inclusions in the plagioclase. These shards are euhedral and roughly 0.15 mm long. The opaque minerals occur as discrete, equant, subhedral to anhedral crystals, up to 0.9 mm across, but more generally 0.3mm across.

B.6 RD10-JER-04

Minerals	Modal abundance (%)
plagioclase	60
orthopyroxene	20
amphibole	15
opaques	5

Plagioclase is euhedral to subhedral, lath-shaped and generally 0.9 mm long. Plagioclase sometimes occurs with quartz in granophyric texture. Orthopyroxene is euhedral to subhedral, 0.3–0.6 mm long and may be partially to completely altered to amphibole.

B.7 RD10-JER-05

Minerals	Modal abundance (%)
quartz	50
plagioclase	40
amphibole	10
chlorite	*trace*

Quartz is seen as pristine, anhedral, equant crystals, 0.03–0.15 mm across, while plagioclase occurs as heavily altered, subhedral laths, generally 0.15 mm long. The plagioclase alteration ranges from mild to extreme, with very few pristine crystals (*i.e.* <10 in the entire thin-section) that show Carlsbad and lamellar twinning. Amphibole occurs as irregular, interstitial patches, 0.15–0.3 mm across, though there are larger aggregations, 0.6–>10 mm across. These large aggregations show chlorite in the cores.

B.8 RD10-JER-05A

This description relates only to the portion comprising roughly two-thirds of this thin-section, as the remaining third is virtually identical to RD10-JER-

05. The reader is directed to the description of that thin-section for details on it's lithology.

Minerals	**Modal abundance (%)**
plagioclase	40
quartz	35
amphibole	20
opaques	5
calcite	*trace*

Plagioclase crystals are subhedral laths, 1–>3 mm long. Some plagioclase crystals display pristine cores and finely altered rims, whereas other crystals are pervasively altered showing only relict Carlsbad and lamellar twinning. Quartz is dominantly seen with plagioclase, in granophyric patches, 1–3 mm across. In places, a single crystal constitutes the plagioclase component of a granophyric patch, with quartz occurring as lenses within. Amphibole occurs as irregular, anhedral patches, equant to elongate, 0.6–>1.5 mm across. The opaque minerals are euhedral to subhedral, 0.15–0.3 mm across. A single, large (∼3 mm) calcite crystal is observed in a poikilitic to semi-poikilitic relationship to all other minerals.

B.9 RD10-THK-03

Minerals	**Modal abundance (%)**
plagioclase	65
epidote	25
opaques	<5
quartz	5

Plagioclase occurs as euhedral laths, ∼0.6 mm long, with a few crystals >3.5 mm long. All plagioclase crystals are pervasively altered to a rusty brown colour, with Carlsbad and lamellar twinning clearly visible. Euhedral to sub-

hedral epidote (0.06–0.3 mm long) is seen evenly distributed among the other minerals and also as discrete amygdules. In the amygdules, epidote crystals up to 1mm long, in an interlocking relationship with euhedral quartz of similar size. Quartz occurs as discrete subhedral to anhedral crystals, sometimes in granophyric relationship to the plagioclase around the epidote amygdules. The opaque minerals occur as small (<0.15 mm), euhedral shards and large (0.3–0.45 mm) equant, subhedral crystals.

B.10 RD10-THK-04

Minerals	**Modal abundance (%)**
coarse-grained component	*20*
quartz	80
plagioclase	15
opaques	<5
calcite	*trace*
fine-grained component	*80*
unidentifiable mineral	100

The highly birefringent mineral of the fine-grained component of this rock is too fine to be reliably identified by optical methods, but makes up a supporting matrix to the coarser grains and accounts for 80% of the rock. Quartz and plagioclase both occur as lath-shaped, subhedral to anhedral crystals, generally 0.15–0.25 mm long, but up to 0.45 mm long in places. Quartz and plagioclase also appear to define an imbrication fabric in the thin-section, oriented such that the long dimension of these crystals is perpendicular to the long dimension of the petrographic slide. Calcite is not very common, but is euhedral to subhedral, roughly 1.2 mm across.

B.11 RD10-LGL-01

Minerals	Modal abundance (%)
plagioclase	50
chlorite	45
opaques	<5
calcite	*trace*

Plagioclase occurs as randomly oriented, lath-shaped crystals, 0.3–3 mm long, displaying moderate to extreme alteration, some with clean cores. Chlorite occurs as subhedral to anhedral crystals, similar in size to the plagioclase and in places is fracture-filling. Chlorite is also seen as very irregular patches, with one of these having a calcite core. The opaque minerals are equant, subhedral to anhedral, 0.045–0.15 mm across.

B.12 RD10-LGL-03

Minerals	Modal abundance (%)
plagioclase	50
chlorite	45
opaques	5

Plagioclase crystals are all extensively altered, commonly subhedral with very ragged edges, 0.12–0.45 mm long. Some plagioclase crystals are subhedral to anhedral, equant blocks, >5 mm across and extensively altered. Chlorite is subhedral to anhedral, equant to lath-shaped and found disseminated in the rock, though it is sometimes found as patches. Opaque minerals (equant, 0.03 mm across) are seen entirely enclosed in these crystals.

B.13 RD10-LGL-06

Minerals	Modal abundance (%)
plagioclase	50
chlorite	45
opaques	5

This thin-section is very similar to RD10-LGL-03, with the exception of the nature of chlorite. Chlorite, in this rock, occurs as radiating sheafs, from 1–>3 mm across.

B.14 RD10-LGL-06A

Minerals	Modal abundance (%)
plagioclase	50
chlorite	45
opaques	<5

Plagioclase and epidote occur as subhedral laths, of similar size, ∼0.2 mm long. Plagioclase is occasionally seen to be as long as 1.2 mm, while chlorite is also seen to infill a fracture. The plagioclase crystals are generally more pristine than in other LGL samples described, though there are patches where very altered plagioclase is seen. Though there are sharp contacts between patches of pristine and altered plagioclase, there are no other features to distinguish these zones. Opaque minerals are subhedral to anhedral, 0.3–0.3 mm across.

B.15 4701-0210a

Minerals	Modal abundance (%)
plagioclase	50
amphibole	40
quartz	10

Plagioclase crystals are very heavily altered to a fine-grained, pinkish-brown,

highly birefringent mineral. Some relict Carlsbad twins are visible and, though alteration is pervasive enough to obscure grain boundaries, plagioclase occurs in patches (0.03–3.0 mm across) that are linked, appearing as lace work. Amphibole crystals are generally euhedral to subhedral laths, though there are some that are anhedral. Crystals are 0.15–1.2 mm long, with some showing clear 60/120 cleavage and are dispersed throughout rock, with only little local clumping.

B.16 4701-9080

Minerals	Modal abundance (%)
plagioclase	45
amphibole	45
opaques	5
quartz	5

Amphibole crystals are euhedral to subhedral laths ∼1.2 mm long, with some very fine-grained aggregations (in places, pseudomorphing hexagons). Plagioclase occurs as euhedral to subhedral laths, generally 1.2–1.5 mm long, but as small as 0.15 mm long in places. Carlsbad and lamellar twinning are visible and all crystals have pristine cores, that are unaltered despite the presence of cracks. Some plagioclase crystals (∼10%) are heavily altered, but these are exclusively found in lineaments. Opaques are euhedral to anhedral, generally equant, 0.15–1 mm. Quartz crystals are anhedral, ∼1.2 mm long, with very irregular boundaries.

B.17 4703-0379b

Minerals	Modal abundance (%)
plagioclase	75
amphibole	15
quartz	5
opaques	<5
epidote	*trace*

Plagioclase is heavily altered to a rusty brown, occurring as euhedral to subhedral laths, ∼0.3 mm long. Quartz is seen as ovoid, vesicle-filling crystals, 0.06–0.3 mm across. One large quartz crystal completely encloses a plagioclase crystal showing a Carlsbad twin. Opaque minerals are equant crystals, from 0.03–0.3 mm across, with larger crystals being euhedral, while smaller ones are anhedral.

B.18 4703-406

Minerals	Modal abundance (%)
groundmass	*85*
plagioclase	65
amphibole	30
opaques	<5
quartz	*trace*
phenocrysts	*15*
plagioclase	60
epidote	25
orthopyroxene	15

Groundmass plagioclase is heavily altered to pink-brown, subhedral to anhedral laths, ∼0.15 mm long and display relict Carlsbad twinning. The opaque minerals are anhedral, 0.06–0.3 mm, interstitial to plagioclase in the groundmass and sometimes as inclusions within the phenocrysts. Groundmass amphibole occurs as ill-defined patches. Phenocrysts tend to occur in clumps

of discrete crystals. Phenocryst plagioclase occurs as euhedral laths, 1.5–4 mm long, with epidote occurring in moderately abundant fractures. The plagioclase, more generally, is moderately altered to a fine-grained, highly birefringent mineral. Epidote phenocrysts are subhedral to anhedral, 0.3–3.5 mm long and seen as an alteration of plagioclase. Orthopyroxene is euhedral to subhedral, with ragged boundaries.

B.19 4703-4048b

Minerals	**Modal abundance (%)**
plagioclase	60
opaques	40
amphibole	*trace*
orthopyroxene	*trace*

Subhedral to euhedral laths plagioclase occurs in two size groups, one 0.15–0.3 mm long and the other, >1 mm long, with minor amphibole found around the crystals. The larger crystals (accounting for a sixth of the plagioclase population) are generally fresher than the smaller crystals, which are moderately altered to pink-brown. The opaque minerals are euhedral, equant, ∼0.15 mm across and interstitial to the plagioclase crystals. The observed orthopyroxene is 0.6 mm long, subhedral and equant to lath-shaped. Some othropyroxene are moderately altered to a fine-grained mineral.

B.20 4703-5326a

Minerals	Modal abundance (%)
groundmass	*95%*
plagioclase	65
orthopyroxene/amphibole	30
opaques	<5
quartz	*trace*
phenocrysts	*5%*
plagioclase	60
quartz	35
opaques	<5

Groundmass plagioclase is altered to a light pink colour and no grain boundaries are visible. Anhedral, equant crystals (0.03–0.15 mm across) of groundmass orthopyroxene are lightly to heavily altered to amphibole. Needles of orthopyroxene/amphibole up to 0.3 mm long occur with anhedral, equant quartz crystals, 0.15 mm across. Phenocryst plagioclase, 0.6 mm long, anhedral to subhedral, equant to lath-shaped, are fresh to heavily altered. Quartz phenocrysts are ∼0.45mm ovoids and opaque phenocrysts are anhedral, irregular, angular to rounded, crystals, 0.15–0.9 mm across.

Appendix C

Sample crushing procedures

The samples were first sawed into slabs, 5–10 mm thick, with a diamond tile-saw. Weathered surfaces were also trimmed at this time. These slabs, wrapped in plastic to prevent contamination, were broken into small pieces with a sledgehammer against a steel plate. These pieces were visually inspected and those that were too large (*i.e.* larger than roughly $5 \times 5 \times 5$ mm) or showed visible country rock inclusions or fracture-infill material were removed.

These pieces were split into two aliquots. One aliquot was crushed in a tungsten carbide (WC) ring-and-puck mill and the other was crushed with a motorized agate mill. This two-method crushing procedure was used to minimize contamination by Nb, Ta and Co from the WC mill and SiO_2 from the agate mill. The aliquots from the WC mill were submitted for major element analyses and the agate milled aliquots were submitted for trace element analyses. Both aliquots were crushed to a flour-like consistency. This took approximately 3.5 minutes in the WC mill and 5–10 minutes in the agate mortar.

In between crushing samples, the components of the WC mill were washed in water, wiped down with ethanol and dried with compressed air. Following

this, approximately 2 tablespoons of pure quartz was crushed for 3.5 minutes to remove any residual traces of the previous sample. The resulting quartz powder was disposed of and the mill was washed, wiped and dried again to remove any traces of crushed quartz, before running the next sample. The cleaning procedure for the agate mill was similar, except that 4 tablespoons of quartz were crushed over 2 minutes.

Appendix D

Analytical results

Table D.1: Results of XRF whole-rock major element analyses

Analyte	RD10-129-01	RD10-129-01A	RD10-129-02	RD10-129-03	RD10-129-04	RD10-129-05	RD10-129-06	RD10-129-07	RD10-129-08	RD10-129-09
SiO_2 *	52.97	52.45	52.80	52.96	52.40	52.17	51.50	51.93	51.79	52.19
TiO_2 *	1.29	1.33	1.29	2.48	1.03	1.22	1.29	1.69	1.20	1.03
Al_2O_3 *	14.72	15.61	14.30	11.52	14.49	13.29	12.65	15.97	15.42	15.33
Fe_2O_3 ^{T} *	14.34	11.85	14.93	17.65	13.48	14.31	14.29	12.70	12.40	12.52
MnO *	0.19	0.15	0.20	0.21	0.19	0.20	0.20	0.16	0.16	0.18
MgO *	5.00	5.10	5.06	3.85	7.23	7.05	6.82	3.82	5.26	6.19
CaO *	9.38	9.05	9.38	8.70	9.14	8.86	8.64	9.30	9.70	9.94
Na_2O *	2.30	2.42	2.23	2.07	2.05	1.80	1.64	2.46	2.16	2.05
K_2O *	0.39	0.44	0.40	0.50	0.31	0.30	0.28	0.75	0.54	0.39
P_2O_5 *	0.072	0.076	0.072	0.130	0.082	0.102	0.121	0.220	0.162	0.086
LOI *	0.43	2.12	0.31	0.70	0.34	1.68	3.27	1.65	1.74	0.88
Total	101.08	100.60	100.97	100.77	100.74	100.99	100.70	100.65	100.54	100.79
Ba *	142.7	169.8	155.3	227.0	196.6	212.9	253.8	714.1	451.9	229.8
Cr *	95.4	104.8	96.7	38.1	230.6	217.6	193.2	47.3	82.2	143.7
Cu *	128	188	120	92	68	61	62	55	66	81
Ni *	68	71	64	39	71	78	62	26	40	55
Sc *	32	29	29	35	28	27	27	26	28	28
V *	195.4	204.5	201.6	354.8	151.4	169.2	168.0	181.4	155.5	156.2
Zn *	83	92	94	132	86	97	98	94	81	76
Ga *	19.7	20.5	19.6	22.1	17.0	17.5	16.6	20.20	18.50	18.40
Rb *	10.0	11.3	10.3	10.7	7.3	6.5	6.2	19.00	12.40	9.60
Sr *	163.8	171.3	158.1	200.0	234.8	223.7	222.0	510.00	432.20	255.70
Y *	20.6	20.8	21.4	30.4	14.9	17.5	18.7	21.50	17.30	14.50
Zr *	56.8	61.1	56.1	92.0	44.6	54.2	60.6	81.10	61.20	43.30
Li	13.1	24.2	10.2	12.1	7.2	12.8	18.6	14.3	18.3	10.4
Be	0.6	1.2	0.2	0.6	0.3	0.4	0.4	0.7	0.7	0.4
Co	65.5	43.7	59.0	41.6	48.1	47.8	52.4	36.3	39.1	45.4
Ge	2.04	1.65	2.13	2.24	1.97	2.15	2.16	1.86	1.83	1.76
Nb	3.3	2.8	2.7	3.8	2.0	2.4	2.7	4.5	3.3	2.5
Mo	1.74	1.09	0.81	0.83	0.99	0.62	0.62	0.58	0.56	1.21
Ru	0.27	0.14	0.13	0.08	0.15	0.16	0.08	0.08	0.09	0.30
Pd	2.11	2.36	1.86	3.11	1.70	1.84	2.09	2.50	2.13	1.39
Ag	0.58	0.53	0.27	0.23	0.17	0.19	0.20	0.22	0.18	0.38
Cd	0.43	0.46	0.45	0.29	0.25	0.58	0.48	0.38	0.41	0.31
Sn	4.43	3.00	3.22	3.00	2.38	2.59	2.76	2.92	2.56	3.09
Sb	1.19	0.55	0.48	0.49	0.17	0.13	0.15	0.19	0.13	0.31
Te	0.68	0.13	0.21	-	-	-	-	-	-	-
Cs	0.50	0.43	0.43	0.66	0.36	0.63	0.80	0.59	0.42	0.31

data continued on next page. . .

Table D.1 – continued

Analyte	RD10-129-01	RD10-129-01A	RD10-129-02	RD10-129-03	RD10-129-04	RD10-129-05	RD10-129-06	RD10-129-07	RD10-129-08	RD10-129-09
La	9.01	10.3	7.46	13.5	6.85	9.32	11.1	26.5	19.4	8.07
Ce	17.7	20.0	14.9	27.5	13.6	19.0	23.7	52.0	38.5	16.2
Pr	2.32	2.54	1.93	3.69	1.77	2.46	2.95	6.12	4.66	2.14
Nd	10.1	10.8	8.91	17.3	8.29	11.0	12.8	24.7	18.6	9.44
Sm	3.24	3.34	2.89	5.36	2.51	3.21	3.61	5.08	3.93	2.69
Eu	1.25	1.30	1.15	1.97	1.01	1.21	1.30	1.94	1.57	1.12
Gd	4.38	4.22	4.19	7.41	2.96	3.90	4.09	5.14	4.07	3.38
Tb	0.75	0.68	0.70	1.15	0.48	0.59	0.65	0.71	0.60	0.54
Dy	4.53	4.41	4.43	7.35	2.89	3.66	3.97	4.33	3.65	3.09
Ho	0.92	0.85	0.89	1.41	0.57	0.73	0.74	0.83	0.67	0.63
Er	2.44	2.40	2.41	3.73	1.55	1.89	2.03	2.16	1.83	1.61
Tm	0.365	0.347	0.339	0.524	0.199	0.274	0.272	0.293	0.242	0.237
Yb	2.06	2.23	2.09	3.20	1.28	1.62	1.70	1.83	1.53	1.35
Lu	0.33	0.32	0.31	0.43	0.18	0.24	0.23	0.25	0.22	0.22
Hf	2.02	2.37	1.73	2.99	1.33	1.62	1.82	2.13	1.77	1.42
Ta	1.58	0.84	0.84	0.67	0.46	0.45	0.44	0.50	0.39	0.96
W	18.8	12.5	12.4	23.7	-	7.21	0.56	2.30	-	0.23
Re	0.059	0.015	0.004	-	0.003	-	0.004	-	-	0.055
Os	1.07	0.38	0.29	0.25	0.24	0.19	0.21	0.17	0.20	1.10
Ir	-	-	-	-	-	-	-	-	-	-
Pt	0.07	0.06	0.03	0.05	0.03	0.04	0.03	0.03	0.03	0.06
Au	0.87	0.28	0.23	0.15	0.18	0.10	0.21	0.16	0.11	0.55
Tl	1.53	0.80	0.45	0.33	0.29	0.26	0.17	0.22	0.18	1.24
Pb	6.03	23.2	4.60	3.42	2.56	4.50	4.82	6.28	5.70	2.45
Th*	1.5	2.1	1.2	1.8	-	1.3	1.6	2.6	1.9	-
U	0.37	0.40	0.38	0.38	0.10	0.15	0.17	0.54	0.24	0.15

* Analyses performed using XRF, all others using ICP-MS.

Fe_2O_3 ^{T} = all iron reported as Fe_2O_3.

Oxides reported as wt. %, all others in ppm.

"-" below detection limits.

Table D.1: Results of XRF whole-rock major element analyses

Analyte	RD10-129-10	RD10-130-01	RD10-130-04	RD10-751-01	RD10-751-02	RD10-NEL-01	RD10-NEL-02	RD10-JER-01	RD10-JER-02	RD10-JER-03
SiO_2 *	52.55	52.95	52.18	57.78	59.57	52.72	52.39	58.76	53.30	53.62
TiO_2 *	1.42	1.37	1.28	1.32	1.41	1.42	1.21	2.11	1.28	1.47
Al_2O_3 *	13.97	17.35	14.62	14.97	14.54	15.98	14.59	11.39	16.95	14.99
Fe_2O_3 ^{T} *	14.70	11.43	14.46	8.16	6.46	9.64	14.16	14.54	11.48	13.47
MnO *	0.19	0.14	0.19	0.06	0.07	0.11	0.19	0.18	0.15	0.17
MgO *	5.12	3.62	5.04	6.55	7.27	7.84	5.72	2.00	3.30	4.13
CaO *	9.30	9.19	9.34	2.11	1.15	4.85	8.85	6.77	9.00	8.73
Na_2O *	2.01	2.53	2.25	1.46	0.05	3.03	2.28	2.31	2.51	2.30
K_2O *	0.34	0.98	0.34	4.61	4.22	0.87	0.78	1.28	1.11	0.80
P_2O_5 *	0.094	0.202	0.073	0.628	0.672	0.112	0.086	0.405	0.191	0.213
LOI *	0.98	0.87	0.75	2.34	4.42	4.06	0.36	0.70	0.89	0.53
Total	100.67	100.62	100.53	99.99	99.84	100.63	100.62	100.45	100.15	100.43
Ba *	-	649.4	130.7	1074.8	2202.3	215.9	208.5	1094.8	664.7	675.1
Cr *	-	45.2	96.7	365.5	348.4	175.1	164.5	2.3	52.4	68.5
Cu *	-	43	136	4	8	158	102	54	52	53
Ni *	-	24	68	19	17	89	82	7	30	38
Sc *	-	23	28	21	25	29	32	28	22	24
V *	-	140.2	195.2	172.4	178.8	196.4	187.5	149.5	160.0	189.5
Zn *	-	81	86	8	61	128	90	118	74	89
Ga *	18.90	21.10	19.30	23.50	19.30	20.50	19.20	20.40	19.80	19.20
Rb *	10.30	22.10	14.20	437.90	413.10	15.90	17.60	33.50	33.30	21.30
Sr *	176.90	566.10	166.10	142.80	42.30	170.10	219.80	369.90	470.40	396.60
Y *	22.50	19.50	20.10	19.10	27.30	20.50	19.30	40.50	20.50	22.80
Zr *	66.40	76.30	56.80	345.90	371.70	83.20	66.30	169.20	83.20	92.00
Li	11.4	16.2	24.3	68.2	143	143	13.4	16.1	13.5	9.6
Be	0.5	0.5	0.3	7.4	8.9	2.5	1.1	3.1	1.2	1.6
Co	47.0	33.1	47.0	20.1	24.3	43.6	44.8	39.8	31.3	34.7
Ge	1.79	1.60	2.13	2.31	2.24	2.24	2.02	2.26	1.69	2.05
Nb	2.8	4.1	2.2	30.9	24.7	5.3	3.6	11.2	5.1	5.2
Mo	0.94	0.73	0.54	1.26	1.08	0.96	0.89	2.61	0.76	0.76
Ru	0.14	0.10	0.05	0.05	-	0.07	0.12	0.28	0.10	0.06
Pd	2.16	2.25	2.29	14.5	14.6	2.74	2.12	6.50	2.15	2.45
Ag	0.24	0.26	0.17	0.94	0.79	0.39	0.23	1.31	0.22	0.23
Cd	0.47	0.48	0.43	0.31	0.54	0.40	0.34	0.56	0.38	0.62
Sn	3.28	2.69	2.49	8.06	7.86	3.12	2.74	5.14	2.95	2.85
Sb	0.22	0.13	0.06	0.78	0.50	0.27	0.21	0.87	0.39	0.32
Te	-	-	-	-	-	-	-	-	-	-
Cs	0.36	0.23	0.27	10.3	6.13	0.30	0.24	2.24	2.04	1.82

data continued on next page...

Table D.1 – continued

Analyte	RD10-129-10	RD10-130-01	RD10-130-04	RD10-751-01	RD10-751-02	RD10-NEL-01	RD10-NEL-02	RD10-JER-01	RD10-JER-02	RD10-JER-03
La	7.92	25.0	8.32	69.1	77.1	12.3	10.0	48.1	24.5	28.4
Ce	16.6	49.2	16.8	99.6	116	30.0	20.5	87.6	48.5	55.6
Pr	2.24	5.74	2.13	17.9	20.2	4.30	2.64	11.2	5.85	6.75
Nd	10.5	22.4	9.74	65.7	73.8	18.6	11.7	44.5	23.3	27.1
Sm	3.50	4.71	3.30	10.7	12.7	4.68	3.38	9.07	4.92	5.66
Eu	1.33	1.85	1.25	1.82	2.83	1.90	1.29	3.04	1.75	1.92
Gd	4.76	4.63	4.07	8.33	9.90	5.71	4.80	10.2	5.37	6.16
Tb	0.76	0.64	0.68	0.94	1.07	0.86	0.77	1.45	0.76	0.87
Dy	4.70	3.79	4.26	5.38	6.16	5.41	4.98	8.64	4.77	5.51
Ho	0.94	0.73	0.86	1.01	1.12	1.09	0.98	1.75	0.93	1.10
Er	2.57	1.90	2.34	2.76	2.89	2.89	2.72	4.58	2.57	2.90
Tm	0.329	0.256	0.316	0.39	0.39	0.40	0.38	0.68	0.35	0.40
Yb	2.05	1.55	1.95	2.34	2.45	2.47	2.31	4.00	2.13	2.50
Lu	0.30	0.22	0.27	0.35	0.34	0.35	0.33	0.55	0.31	0.35
Hf	1.99	2.00	2.16	14.04	14.10	2.93	2.15	4.63	2.12	2.32
Ta	0.78	0.64	0.43	3.28	2.17	0.72	0.47	1.83	0.53	0.53
W	1.29	1.53	3.65	8.11	8.59	4.72	8.57	45.7	1.12	4.14
Re	0.013	-	-	0.030	0.024	0.028	0.020	0.120	0.023	0.022
Os	0.44	0.18	0.20	0.34	0.26	0.25	0.22	2.02	0.19	0.23
Ir	-	-	-	0.13	0.10	-	-	0.26	-	-
Pt	0.05	0.03	0.04	0.23	0.25	0.12	0.09	0.32	0.10	0.09
Au	0.34	0.07	0.25	0.61	0.22	0.06	0.05	2.89	20.2	-
Tl	0.74	0.31	0.26	3.06	2.94	0.27	0.18	1.08	0.25	0.21
Pb	2.74	6.81	7.12	4.26	17.5	150	2.99	11.7	6.34	7.57
Th*	1.3	1.9	-	25.4	28.5	4.1	2.1	3.7	1.5	2.5
U	0.16	0.34	0.19	15.4	14.1	0.23	0.23	1.04	0.42	0.50

* Analyses performed using XRF, all others using ICP-MS.

Fe_2O_3 ^{T} = all iron reported as Fe_2O_3.

Oxides reported as wt. %, all others in ppm.

"-" below detection limits.

Table D.1: Results of XRF whole-rock major element analyses

Analyte	RD10-JER-04	RD10-JER-05A	RD10-THK-01	RD10-THK-02	RD10-THK-03	RD10-LGL-01	RD10-LGL-01A	RD10-LGL-02	RD10-LGL-03	RD10-LGL-04
SiO_2 *	52.33	56.16	56.78	55.96	55.96	50.38	50.66	50.00	50.65	50.67
TiO_2 *	1.03	2.05	2.57	2.60	2.57	1.14	1.27	1.22	1.52	1.64
Al_2O_3 *	15.31	12.04	13.58	14.09	14.21	15.06	16.06	14.74	14.54	14.08
Fe_2O_3 ^{T} *	13.07	15.59	8.89	10.17	9.69	14.30	13.68	15.01	13.61	14.16
MnO *	0.18	0.19	0.09	0.15	0.15	0.23	0.19	0.23	0.21	0.24
MgO *	6.19	2.76	2.89	2.32	2.56	5.75	5.22	5.56	5.36	5.52
CaO *	9.35	6.99	4.20	3.71	3.52	8.95	6.40	9.10	7.41	8.17
Na_2O *	2.10	1.84	2.29	2.78	2.69	2.22	1.68	2.32	2.39	2.24
K_2O *	0.43	1.08	3.99	4.23	4.46	0.85	0.95	0.59	1.64	1.29
P_2O_5 *	0.124	0.357	1.227	1.280	1.251	0.185	0.203	0.200	0.263	0.457
LOI *	0.85	1.16	3.17	2.12	2.65	1.50	3.96	1.50	2.42	1.77
Total	100.96	100.21	99.67	99.41	99.71	100.55	100.26	100.47	100.02	100.24
Ba *	382.5	928.3	2601.5	3125.6	2444.6	649.7	421.8	571.2	734.9	737.7
Cr *	168.5	26.6	-	-	-	146.1	138.8	125.1	99.3	147.5
Cu *	90	68	116	14	29	116	33	119	82	123
Ni *	84	21	-	-	-	85	83	86	68	84
Sc *	30	31	14	17	17	29	30	30	29	26
V *	161.0	202.7	111.8	114.5	114.9	184.2	241.9	200.0	183.4	195.7
Zn *	85	129	125	188	153	91	131	91	111	131
Ga *	17.70	19.90	24.20	24.80	24.90	17.90	25.40	18.60	18.70	19.70
Rb *	9.20	39.20	129.40	144.80	144.90	49.10	46.70	28.90	125.80	91.90
Sr *	339.80	371.80	334.30	628.60	386.10	411.20	519.50	422.00	363.60	336.80
Y *	15.70	33.00	42.80	40.40	40.40	20.70	13.40	21.80	21.80	23.50
Zr *	59.60	126.90	1020.60	947.20	964.50	80.10	91.20	90.90	141.00	184.70
Li	20.2	26.1	46.6	36.6	33.4	11.5	30.8	16.4	23.5	26.7
Be	1.1	1.8	5.8	6.0	6.4	1.1	1.2	1.1	2.1	2.8
Co	46.5	31.4	17.8	15.8	16.5	47.8	43.9	48.0	41.3	47.0
Ge	1.98	2.06	2.73	2.00	1.89	1.92	1.97	1.89	1.77	2.25
Nb	3.2	10.8	56.5	53.7	53.6	4.2	5.6	5.1	7.4	10.2
Mo	0.65	1.08	4.07	3.82	3.06	0.92	0.72	0.89	0.96	1.93
Ru	0.09	-	0.05	-	-	0.05	0.03	0.09	0.06	-
Pd	1.56	4.63	30.5	23.5	23.3	2.81	3.27	3.40	4.88	5.79
Ag	0.19	0.37	1.74	1.52	1.49	0.22	0.24	0.23	0.30	0.59
Cd	0.47	0.40	0.25	0.47	0.38	0.41	0.26	0.35	0.44	0.38
Sn	2.66	3.75	7.32	6.24	6.25	2.54	13.0	3.14	3.33	7.27
Sb	0.23	1.54	1.52	0.33	0.43	0.31	0.24	0.16	0.28	1.61
Te	-	-	-	-	-	-	-	-	-	-
Cs	1.29	2.77	1.36	1.09	0.83	1.18	0.40	0.38	0.82	1.90

data continued on next page. . .

Table D.1 – continued

Analyte	RD10-JER-04	RD10-JER-05A	RD10-THK-01	RD10-THK-02	RD10-THK-03	RD10-LGL-01	RD10-LGL-01A	RD10-LGL-02	RD10-LGL-03	RD10-LGL-04
La	15.2	60.0	304	322	258	30.5	23.5	34.1	39.7	48.4
Ce	30.2	115	581	592	572	58.7	45.9	64.8	76.1	97.6
Pr	3.68	14.1	62.1	61.9	59.3	6.92	5.05	7.58	8.86	11.3
Nd	15.1	55.8	227	226	214	26.4	18.1	28.8	33.7	42.3
Sm	3.33	11.6	36.5	33.4	31.8	5.06	3.00	5.36	6.31	7.34
Eu	1.26	3.35	7.19	6.90	6.35	1.67	1.03	1.76	1.93	1.91
Gd	3.84	12.4	23.3	20.9	20.1	5.03	2.75	5.36	5.97	7.34
Tb	0.57	1.76	2.18	1.92	1.89	0.71	0.41	0.75	0.84	0.94
Dy	3.69	11.1	11.7	10.7	10.5	4.56	2.69	4.81	5.19	5.26
Ho	0.74	2.19	1.94	1.74	1.72	0.91	0.56	0.97	1.00	1.01
Er	1.99	5.80	4.57	4.09	4.20	2.49	1.57	2.61	2.66	2.65
Tm	0.27	0.79	0.59	0.51	0.50	0.34	0.22	0.37	0.35	0.375
Yb	1.74	4.97	3.44	2.99	2.97	2.17	1.36	2.35	2.21	2.13
Lu	0.24	0.71	0.47	0.39	0.38	0.32	0.19	0.34	0.31	0.32
Hf	1.58	4.99	22.7	18.2	18.3	2.67	2.95	2.95	4.19	4.57
Ta	0.38	0.82	4.06	3.67	3.57	0.60	0.63	0.59	0.70	1.29
W	1.59	1.04	5.21	3.21	5.27	1.31	4.25	0.25	1.70	4.49
Re	0.020	0.013	0.066	0.034	0.015	0.016	0.010	0.012	0.010	0.046
Os	0.17	0.14	1.38	0.50	0.29	0.17	0.15	0.19	0.15	0.35
Ir	-	-	0.15	0.11	0.08	-	-	-	-	-
Pt	0.07	0.09	0.37	0.27	0.27	0.06	0.06	0.10	0.09	0.12
Au	-	-	1.05	0.39	0.21	-	-	-	-	0.81
Tl	0.11	0.31	1.86	1.51	1.26	0.35	0.36	0.29	0.84	1.05
Pb	3.80	15.6	19.0	55.7	34.1	9.28	5.45	10.5	11.4	15.6
Th*	1.7	3.4	13.3	13.5	13.2	2.5	2.2	3.8	-	2.9
U	0.25	0.95	3.05	2.52	2.89	0.40	1.12	0.49	0.55	0.94

* Analyses performed using XRF, all others using ICP-MS.

Fe_2O_3 ^{T} = all iron reported as Fe_2O_3.

Oxides reported as wt. %, all others in ppm.

"-" below detection limits.

Table D.1: Results of XRF whole-rock major element analyses

Analyte	RD10-LGL-05	RD10-LGL-05A	RD10-LGL-05B	RD10-LGL-06	RD10-LGL-06A	4700-4262	4701-0188b	4701-0210a	4701-0212a	4701-224
SiO_2 *	52.49	51.74	49.77	49.83	48.89	51.51	51.27	51.80	51.98	50.97
TiO_2 *	1.24	1.26	1.61	1.70	1.72	1.75	1.91	1.51	1.99	1.63
Al_2O_3 *	14.53	14.39	13.82	14.21	14.54	14.24	13.67	13.15	13.16	13.75
Fe_2O_3 ^{T} *	13.54	13.95	14.21	14.33	14.42	12.59	12.93	14.03	14.14	14.74
MnO *	0.19	0.19	0.20	0.26	0.22	0.18	0.16	0.23	0.20	0.24
MgO *	6.40	6.01	5.82	6.43	6.18	6.00	5.48	5.91	6.50	5.38
CaO *	4.93	3.23	6.90	7.23	6.82	6.79	6.68	7.40	5.82	7.35
Na_2O *	2.70	3.09	3.91	2.14	2.59	2.15	2.20	2.93	2.65	2.77
K_2O *	1.56	0.87	1.23	1.46	0.96	2.33	1.77	1.71	0.65	1.52
P_2O_5 *	0.171	0.174	0.370	0.413	0.418	0.525	0.668	0.139	0.230	0.154
LOI *	2.92	5.63	2.42	2.53	3.52	2.28	3.66	1.76	3.03	1.87
Total	100.67	100.54	100.26	100.54	100.28	100.34	100.41	100.56	100.36	100.37
Ba *	702.9	292.4	460.0	781.9	406.6	2100.2	1658.9	533.9	71.3	989.8
Cr *	139.3	143.3	166.2	168.0	176.0	166.7	153.1	31.5	13.9	29.8
Cu *	38	62	112	79	112	60	40	12	28	123
Ni *	65	66	97	95	99	77	60	29	23	26
Sc *	25	27	30	29	25	21	24	42	32	30
V *	184.3	173.7	195.4	199.3	206.8	179.4	181.2	322.2	334.2	339.2
Zn *	97	113	108	125	118	39	79	85	55	85
Ga *	17.50	20.90	18.60	19.40	22.30	18.80	18.50	16.90	20.20	18.60
Rb *	129.20	54.00	80.30	112.00	63.20	65.40	78.50	46.50	15.70	30.00
Sr *	290.00	109.90	422.80	310.80	296.70	554.50	660.60	183.20	209.40	203.00
Y *	19.20	19.50	22.00	22.40	23.00	23.90	25.40	26.30	33.20	29.10
Zr *	87.20	90.50	142.80	155.10	158.50	191.80	234.30	103.40	169.60	114.20
Li	39.3	68.9	21.6	40.1	43.2	48.0	43.7	18.4	21.5	10.7
Be	2.6	2.1	1.0	1.7	2.3	1.4	1.5	1.1	1.5	1.2
Co	45.8	48.5	46.8	48.0	49.6	39.8	19.0	40.0	39.0	39.7
Ge	1.51	0.67	1.64	1.50	1.21	1.72	1.83	1.81	2.16	2.03
Nb	4.6	3.9	7.2	7.5	8.0	8.5	11.7	7.1	16.8	8.0
Mo	0.87	0.82	0.57	0.86	0.90	1.16	1.24	0.68	3.34	1.39
Ru	-	-	-	-	-	-	-	-	-	-
Pd	2.97	2.96	4.75	4.89	4.98	7.04	8.84	3.68	4.60	3.28
Ag	0.25	0.16	0.28	0.26	0.27	0.35	0.39	0.26	0.77	0.32
Cd	0.29	0.17	0.23	0.18	0.16	0.27	0.30	0.28	0.43	0.38
Sn	3.13	2.84	3.99	4.64	2.91	2.88	3.19	2.64	4.43	3.30
Sb	0.82	0.44	0.52	0.36	0.29	0.18	0.19	0.29	1.07	0.33
Te	-	-	-	-	-	-	-	-	-	-
Cs	0.89	0.25	0.47	0.82	0.69	1.30	0.61	0.23	0.30	0.29

data continued on next page...

Table D.1 – continued

Analyte	RD10-LGL-05	RD10-LGL-05A	RD10-LGL-05B	RD10-LGL-06	RD10-LGL-06A	4700-4262	4701-0188b	4701-0210a	4701-0212a	4701-224
La	19.8	7.62	32.3	36.2	34.2	84.7	118	10.3	18.8	14.7
Ce	41.0	17.7	73.5	70.9	71.1	168	229	26.7	42.2	31.6
Pr	4.80	2.30	7.73	8.42	8.55	19.4	27.2	3.63	5.48	4.06
Nd	18.0	10.1	30.1	32.7	33.7	69.4	98.3	16.6	23.0	17.5
Sm	3.76	2.78	5.88	6.15	6.40	10.3	14.1	4.32	5.65	4.38
Eu	1.30	0.86	1.74	1.81	1.71	2.95	4.15	1.56	1.80	1.66
Gd	4.45	3.91	6.33	6.35	6.52	8.19	9.61	4.67	6.44	5.25
Tb	0.69	0.66	0.81	0.82	0.86	0.86	0.96	0.75	1.05	0.82
Dy	4.13	4.17	4.86	5.00	5.26	5.18	5.57	5.04	6.30	5.67
Ho	0.84	0.85	0.93	0.93	0.96	0.97	1.01	1.06	1.35	1.16
Er	2.28	2.25	2.41	2.51	2.62	2.58	2.58	3.17	3.81	3.37
Tm	0.315	0.293	0.315	0.324	0.328	0.331	0.309	0.443	0.609	0.493
Yb	1.98	1.94	1.97	2.03	2.10	2.11	1.91	2.90	3.32	3.16
Lu	0.29	0.27	0.27	0.27	0.29	0.29	0.26	0.43	0.60	0.47
Hf	2.69	2.84	4.00	3.99	4.21	4.77	5.51	2.74	3.84	2.84
Ta	0.75	0.69	0.79	0.74	0.73	0.63	0.73	0.69	2.20	1.14
W	3.63	2.57	7.38	1.58	3.15	1.13	1.47	0.55	4.08	1.16
Re	0.013	-	0.004	-	-	-	-	-	0.101	0.013
Os	0.23	0.13	-	0.07	0.15	0.09	-	-	1.22	0.34
Ir	-	-	-	-	-	-	-	-	-	-
Pt	0.04	0.05	0.06	0.06	0.05	0.07	0.08	0.03	0.11	0.05
Au	0.35	0.38	0.13	0.04	0.04	0.02	0.02	0.07	1.42	0.45
Tl	1.00	0.29	0.92	0.98	0.60	0.48	0.48	0.29	1.16	0.56
Pb	7.01	6.65	9.95	9.25	14.1	11.1	14.0	3.69	7.61	5.96
Th*	-	1.3	-	-	1.9	4.0	5.8	1.6	3.7	3.2
U	0.57	0.46	0.46	0.43	0.43	0.79	1.09	0.76	0.83	0.85

* Analyses performed using XRF, all others using ICP-MS.

Fe_2O_3 ^{T} = all iron reported as Fe_2O_3.

Oxides reported as wt. %, all others in ppm.

"-" below detection limits.

Table D.1: Results of XRF whole-rock major element analyses

Analyte	4701-9080	4703-0187b	4703-0379b	4703-0468d	4703-0492b	4703-0720a	4703-406	4703-5091	4703-5326a	4703-5326b
SiO_2 *	49.53	54.18	55.34	46.86	47.88	52.10	53.66	51.75	53.45	53.60
TiO_2 *	1.81	1.30	2.18	2.75	2.63	2.72	1.84	1.38	2.14	2.13
Al_2O_3 *	14.07	14.15	14.08	13.31	13.53	13.24	14.51	14.91	14.20	13.90
Fe_2O_3 ^{T} *	12.92	10.26	9.24	11.41	11.79	11.42	12.13	11.06	10.21	10.17
MnO *	0.12	0.14	0.08	0.27	0.14	0.14	0.07	0.12	0.12	0.13
MgO *	5.78	5.10	3.39	4.33	5.15	3.99	5.12	6.60	3.80	3.80
CaO *	6.58	6.79	3.52	6.94	6.27	6.12	4.61	4.02	5.13	4.98
Na_2O *	2.32	2.51	2.34	1.67	1.99	2.82	1.98	2.04	2.69	2.44
K_2O *	2.60	2.17	5.04	4.09	3.39	2.59	2.05	2.51	4.37	4.21
P_2O_5 *	1.123	0.495	1.738	2.032	2.16	1.40	0.570	0.360	1.701	1.71
LOI *	2.81	2.99	2.85	5.58	3.99	2.20	3.87	5.33	1.62	1.61
Total	99.67	100.09	99.79	99.25	98.93	98.75	100.41	100.08	99.42	98.69
Ba *	4519.6	1950.7	3338.5	4926.1	-	-	1752.3	1863.1	4677.3	-
Cr *	112.1	125.1	9.6	76.2	-	-	104.1	190.9	31.0	-
Cu *	60	73	8	243	25.47	26.53	43	44	33	32.33
Ni *	54	72	8	55	67.44	54.82	43	88	17	38.58
Sc *	17	18	-	14	18.00	18.00	20	22	-	14.00
V *	178.0	153.3	142.1	170.4	160.19	149.31	168.2	170.2	150.2	142.36
Zn *	48	56	48	161	155.08	164.97	46	51	38	75.12
Ga *	17.40	18.00	23.30	17.20	21.71	22.83	19.10	18.30	21.90	25.33
Rb *	62.00	67.40	146.80	140.70	73.27	78.42	32.00	76.60	158.10	157.87
Sr *	1499.80	703.30	537.80	1244.80	1840.00	1170.00	415.10	473.30	1761.00	2020.00
Y *	28.30	19.90	27.70	33.80	30.77	32.24	25.40	19.90	28.60	28.01
Zr *	255.90	179.20	577.30	464.60	270.00	468.00	223.60	131.10	507.20	482.00
Li	28.8	25.5	20.1	83.2	-	-	56.1	62.5	23.3	-
Be	1.8	1.9	2.5	2.0	-	-	1.5	1.5	5.5	-
Co	37.0	32.9	19.7	32.7	30.51	26.50	32.2	36.0	23.7	17.08
Ge	1.86	1.84	2.08	1.63	1.69	1.57	1.81	1.52	2.39	1.49
Nb	12.3	11.4	35.1	21.7	23.2	24.2	10.1	6.5	32.8	27.5
Mo	1.87	1.23	2.66	2.12	4.14	2.10	1.22	0.71	3.86	2.87
Ru	-	-	-	-	-	-	-	-	0.33	-
Pd	4.51	5.10	19.7	15.3	-	-	7.92	4.36	17.6	-
Ag	0.40	0.37	1.05	0.81	-	-	0.37	0.22	0.96	-
Cd	0.41	0.37	0.29	0.24	-	-	0.42	0.19	0.38	-
Sn	3.23	3.28	4.62	3.22	1.70	2.37	3.08	2.49	4.77	2.08
Sb	0.24	0.17	0.24	0.18	1.05	0.44	21.7	0.10	0.46	-
Te	-	-	-	-	-	-	-	-	4.27	-
Cs	0.90	0.66	0.32	2.70	1.04	0.68	0.35	0.24	1.98	1.77

data continued on next page...

Table D.1 – continued

Analyte	4701-9080	4703-0187b	4703-0379b	4703-0468d	4703-0492b	4703-0720a	4703-406	4703-5091	4703-5326a	4703-5326b
La	165	76.4	344	216	342.91	211.50	77.6	39.9	302	354.34
Ce	315	150	721	503	666.96	438.10	153	79.9	564	661.94
Pr	37.8	17.5	75.3	53.2	69.39	44.76	17.9	9.46	74.0	66.49
Nd	135	63.3	258	193	261.38	170.49	65.3	35.2	250	245.29
Sm	17.5	9.03	32.0	25.8	33.27	23.50	10.1	5.84	31.4	30.86
Eu	4.91	2.65	7.11	6.47	6.84	4.93	2.96	1.97	8.36	6.14
Gd	12.0	7.32	18.9	20.1	18.65	13.77	8.44	6.31	21.0	15.71
Tb	0.98	0.70	1.34	1.55	1.81	1.58	0.90	0.72	1.25	1.58
Dy	5.79	4.35	7.06	7.99	7.51	7.45	5.42	4.27	7.38	6.68
Ho	1.02	0.80	1.07	1.28	1.10	1.12	1.02	0.80	1.14	0.95
Er	2.68	2.17	2.69	3.32	3.13	3.12	2.64	2.19	2.74	2.63
Tm	0.334	0.281	0.281	0.374	0.31	0.36	0.360	0.280	0.325	0.24
Yb	2.03	1.80	1.69	2.32	2.06	2.26	2.15	1.77	1.95	1.65
Lu	0.27	0.25	0.18	0.28	0.28	0.31	0.29	0.25	0.23	0.21
Hf	3.55	4.06	13.1	10.3	8.86	10.82	5.28	3.77	13.1	11.63
Ta	0.97	1.02	2.64	1.73	1.21	1.27	0.83	0.68	2.95	1.68
W	3.17	0.96	1.84	1.02	2.12	0.74	0.40	0.54	5.33	1.64
Re	0.017	-	-	-	-	-	-	-	0.022	-
Os	0.19	0.13	0.14	-	-	-	0.10	-	0.92	-
Ir	-	-	-	-	-	-	-	-	0.08	-
Pt	0.07	0.08	0.19	0.18	-	-	0.06	0.06	0.17	-
Au	0.27	0.14	0.18	0.11	-	-	0.07	0.04	0.81	-
Tl	0.55	0.49	1.11	0.81	0.44	0.53	0.31	0.38	1.04	0.92
Pb	13.6	20.3	15.9	71.1	62.81	45.83	16.7	13.9	16.7	17.26
Th*	10.4	6.1	43.0	13.3	15.4	11.0	5.9	13.3	36.2	38.3
U	1.30	1.87	8.40	2.34	2.52	1.53	0.78	0.48	7.01	6.02

* Analyses performed using XRF, all others using ICP-MS.

Fe_2O_3 ^{T} = all iron reported as Fe_2O_3.

Oxides reported as wt. %, all others in ppm.

"-" below detection limits.

Table D.1: Results of XRF whole-rock major element analyses

Analyte	4703-5326e	4703-5529	4705-0202b
SiO_2 *	53.03	54.77	52.08
TiO_2 *	2.15	2.61	1.60
Al_2O_3 *	14.15	13.59	14.03
Fe_2O_3 ^{T} *	10.41	9.82	12.36
MnO *	0.12	0.11	0.15
MgO *	3.90	3.05	5.94
CaO *	4.86	4.64	6.51
Na_2O *	2.78	2.65	2.51
K_2O *	3.81	3.52	1.73
P_2O_5 *	1.704	1.38	0.450
LOI *	2.34	2.56	3.03
Total	99.26	98.71	100.38
Ba *	4564.8	-	1577.9
Cr *	26.1	-	177.8
Cu *	47	26.15	47
Ni *	23	55.32	83
Sc *	7	15.00	23
V *	153.1	119.04	164.1
Zn *	35	175.28	138
Ga *	21.70	23.77	18.60
Rb *	121.80	127.13	59.10
Sr *	1653.90	1030.00	473.70
Y *	28.80	31.20	23.30
Zr *	507.30	618.00	181.40
Li	25.6	-	24.4
Be	5.3	-	1.2
Co	39.8	19.14	37.5
Ge	2.28	1.51	1.96
Nb	30.0	29.6	9.6
Mo	5.08	2.29	0.82
Ru	0.30	-	0.33
Pd	17.3	-	6.37
Ag	0.81	-	0.35
Cd	0.22	-	0.25
Sn	4.05	3.45	2.82
Sb	0.42	1.22	0.35
Te	4.30	-	-
Cs	1.13	0.52	1.14

data continued on next page. . .

Table D.1 – continued

Analyte	4703-5326e	4703-5529	4705-0202b
La	280	267.38	61.9
Ce	487	533.67	125
Pr	67.5	52.99	14.7
Nd	224	194.23	52.6
Sm	28.9	25.76	8.43
Eu	7.72	5.03	2.79
Gd	19.3	13.87	7.18
Tb	1.25	1.61	0.75
Dy	7.18	7.34	4.62
Ho	1.12	1.09	0.86
Er	2.55	3.01	2.29
Tm	0.315	0.33	0.308
Yb	1.90	2.13	1.87
Lu	0.21	0.30	0.26
Hf	12.6	13.84	4.60
Ta	2.36	1.53	0.85
W	4.37	1.14	3.02
Re	0.017	-	0.006
Os	0.52	-	0.38
Ir	0.08	-	-
Pt	0.15	-	0.07
Au	0.55	-	0.28
Tl	0.72	1.02	0.34
Pb	15.5	83.40	13.0
Th*	36.9	20.6	3.3
U	7.26	3.04	0.63

* Analyses performed using XRF,
all others using ICP-MS.

Fe_2O_3 ^{T} = all iron reported as Fe_2O_3.

Oxides reported as wt. %, all others in ppm.

"-" below detection limits.

Table D.2: ICP-MS reproducibility using sample duplicates. Accuracy tested using Columbia River Basalt Certified Reference Material)

	Duplicated analyses							CRM analyses					
Analyte	RD10-129-08	RD10-130-04	RD10-JER-05A	RD10-LGL-03	4701-210a	4703-5091	4705-4109c	BCR-2 (2010-09-09)	BCR-2 (2010-10-08)	BCR-2 (2010-10-20)	BCR-2 (2010-10-22)	BCR-2 (2010-10-29)	BCR-2 certified value
Li	17.4	25.1	26.4	23.6	20.1	64.0	21.4	7.9	9.3	8.7	8.2	8.5	9
Be	0.4	0.4	1.7	1.9	1.2	1.4	2.4	3.4	2.0	2.4	2.2	2.4	-
Co	40.4	47.4	31.9	42.0	40.6	36.3	12.5	32.8	36.7	32.2	32.5	33.6	37
Ge	1.81	1.92	2.10	1.67	1.73	1.63	1.77	1.83	1.80	1.87	1.66	1.68	-
Nb	3.29	2.26	10.7	7.42	7.22	6.43	33.1	12.0	12.9	11.2	9.13	10.7	-
Mo	0.45	0.49	1.07	1.05	0.58	0.80	3.64	268	268	250	271	257	248
Ru	0.15	0.05	-	0.05	-	-	0.08	0.19	0.04	-	-	0.94	-
Pd	2.09	2.42	4.69	4.94	3.55	4.46	21.3	10.4	7.89	6.44	6.06	5.92	-
Ag	0.17	0.14	0.34	0.31	0.22	0.23	0.84	0.56	0.46	0.42	0.36	0.33	-
Cd	0.47	0.43	0.39	0.40	0.32	0.22	0.25	1.19	0.99	0.79	0.81	0.95	-
Sn	2.45	2.65	3.90	3.26	2.58	2.51	4.56	3.92	4.08	3.79	3.58	3.70	-
Sb	0.13	0.09	1.47	0.30	0.29	0.12	0.18	0.46	0.41	0.38	0.43	0.44	-
Te	-	-	-	-	-	-	-	-	-	-	-	-	-
Cs	0.39	0.28	2.90	0.76	0.22	0.24	1.23	1.18	1.20	1.14	1.20	1.25	1.1
Ba	508	172	1388	910	706	1556	1379	748	824	786	644	620	683
La	19.3	8.49	59.6	39.8	10.4	40.5	138	25.8	28.8	27.9	21.9	26.2	25
Ce	38.7	17.3	115	76.3	27.2	81.1	232	53.4	59.1	58.1	45.4	53.7	53
Pr	4.67	2.15	14.1	8.93	3.75	9.60	26.7	6.76	7.51	7.32	5.72	6.82	6.8
Nd	18.4	9.99	56.1	33.9	16.6	36.1	87.8	28.5	31.7	30.7	24.0	28.6	28
Sm	3.90	3.15	11.6	6.47	4.35	5.80	12.6	6.83	7.48	7.22	5.54	6.45	6.7
Eu	1.61	1.23	3.36	1.98	1.60	2.05	2.67	2.14	2.41	2.31	1.84	2.15	2
Gd	4.14	4.10	12.5	6.12	4.73	6.25	10.1	7.05	7.47	7.46	7.15	6.95	6.8
Tb	0.60	0.68	1.77	0.82	0.76	0.72	0.94	1.02	1.06	1.09	1.00	0.97	1.07
Dy	3.60	4.35	11.2	5.11	5.04	4.21	5.62	6.52	6.85	7.00	6.37	6.34	-
Ho	0.68	0.87	2.21	1.00	1.04	0.78	1.00	1.35	1.42	1.42	1.32	1.31	1.33
Er	1.83	2.32	5.83	2.68	3.07	2.11	2.68	3.85	3.92	4.06	3.83	3.72	-
Tm	0.244	0.318	0.78	0.35	0.434	0.285	0.350	0.54	0.557	0.58	0.528	0.537	0.540
Yb	1.52	2.00	4.98	2.19	2.85	1.78	2.21	3.53	3.56	3.73	3.45	3.36	3.5
Lu	0.22	0.28	0.70	0.31	0.43	0.24	0.29	0.54	0.54	0.55	0.49	0.50	0.51
Hf	1.82	2.10	4.99	4.31	2.78	3.69	15.4	7.22	5.68	5.35	4.92	4.95	4.8
Ta	0.38	0.41	0.87	0.68	0.66	0.61	2.31	1.16	1.23	1.08	1.01	1.05	-
W	-	3.19	0.79	1.55	0.60	0.34	3.28	3.87	-	0.39	0.20	49.81	-
Re	0.004	-	0.010	0.005	-	-	-	0.040	0.015	0.019	0.013	0.019	-
Os	0.21	0.18	0.14	0.15	-	-	0.22	0.50	0.24	0.12	-	0.22	-
Ir	-	-	-	-	-	-	0.07	0.10	-	-	-	-	-
Pt	0.03	0.03	0.10	0.08	0.05	0.07	0.13	0.25	0.10	0.10	0.08	0.07	-
Au	0.18	0.09	-	-	0.01	0.03	0.12	0.75	0.15	-	0.02	0.08	-
Tl	0.16	0.19	0.27	0.79	0.29	0.39	0.48	0.33	0.36	0.28	0.28	0.11	-
Pb	5.78	7.39	15.2	11.4	3.52	12.5	11.3	12.1	11.1	9.68	11.6	10.8	11
Th	1.62	1.76	5.75	3.63	2.40	3.59	36.2	6.15	6.37	6.64	6.18	6.08	6.2
U	0.26	0.19	0.95	0.56	0.78	0.45	5.59	1.95	1.90	1.85	1.85	1.83	1.69

Table D.3: Comparison of analytical results from Ewanchuk (2006) and this study, using samples from location 751.

Analyte	Units	RD10-751-02[a]	751A[b]	Analyte	Units	RD10-751-02[a]	751A[b]
SiO_2	wt. %	59.57	59.69	Nb	ppm	24.7	22.7
TiO_2	wt. %	1.408	1.392	Sn	ppm	7.86	3
Al_2O_3	wt. %	14.54	14.31	Sb	ppm	0.50	1.4
Fe_2O_3 ^{T}	wt. %	6.464	6.090	Cs	ppm	6.13	6.7
MnO	wt. %	0.071	0.085	Ba	ppm	2492	3432
MgO	wt. %	7.270	6.490	La	ppm	77.1	78.4
CaO	wt. %	1.150	2.130	Ce	ppm	116	183
Na_2O	wt. %	0.054	0.050	Pr	ppm	20.2	22.6
K_2O	wt. %	4.220	4.830	Nd	ppm	73.8	81
P_2O_5	wt. %	0.672	0.620	Sm	ppm	12.7	12.4
Ni	ppm	17	30	Eu	ppm	2.83	2.62
Sc	ppm	25	26	Gd	ppm	9.90	8.73
V	ppm	178.8	172	Tb	ppm	1.07	0.94
Zn	ppm	61	60	Dy	ppm	6.16	4.4
Th	ppm	28.50	33.3	Ho	ppm	1.12	0.76
U	ppm	14.10	11.2	Er	ppm	2.89	2.1
Zr	ppm	371.7	376	Tm	ppm	0.39	0.284
Be	ppm	8.9	7	Yb	ppm	2.45	1.79
Cr	ppm	352	220	Lu	ppm	0.34	0.252
Co	ppm	24.3	43	Hf	ppm	14.10	10.5
Ga	ppm	23.4	20	Ta	ppm	2.17	2.01
Ge	ppm	2.24	1.9	W	ppm	8.59	338
Rb	ppm	476	443	Tl	ppm	2.94	1.6
Sr	ppm	68.1	94	Th	ppm	21.6	33.3
Y	ppm	29.3	24.4	U	ppm	14.1	11.2

[a] Data from analyses performed in this study

[b] Data from Ewanchuk (2006).